UNIVERSITY OF ROCHESTER
LABORATORY FOR LASER ENERGETICS

Volume 92
July–September 2002
DOE/SF/19460-465

# LLE Review

## Quarterly Report

## About the Cover:

LLE has recently completed the development of a new carbon-activation diagnostic designed for tertiary neutron yield measurements on OMEGA (see p. 161). Tertiary neutrons with energies over 20 MeV are used to determine the areal mass density of inertial confinement fusion targets. Experiments that use this diagnostic and take advantage of the purification facility and handling procedures that ensure a low level of sample contamination have shown very good reproducibility. This diagnostic, with proper choice of shielding, is also suitable for use on the National Ignition Facility.

The cover photo (also shown at left) shows Dr. Vladimir Glebov preparing a carbon disk (1) for counting in the carbon activation system. The carbon disk was irradiated on OMEGA in a sealed vacuum bag. Once it is removed from the bag, it is inserted into the two NaI scintillation detectors, which are encased in lead shielding (2). The carbon activation system electronics (3) provide data that are analyzed by the PC-based data acquisition system (4).

This report was prepared as an account of work conducted by the Laboratory for Laser Energetics and sponsored by New York State Energy Research and Development Authority, the University of Rochester, the U.S. Department of Energy, and other agencies. Neither the above named sponsors, nor any of their employees, makes any warranty, expressed or implied, or assumes any legal liability or responsibility for the accuracy, completeness, or usefulness of any information, apparatus, product, or process disclosed, or represents that its use would not infringe privately owned rights. Reference herein to any specific commercial product, process, or service by trade name, mark, manufacturer, or otherwise, does not necessarily constitute or imply its endorsement, recommendation, or favoring by the United States Government or any agency thereof or any other sponsor. Results reported in the LLE Review should not be taken as necessarily final results as they represent active research. The views and opinions of authors expressed herein do not necessarily state or reflect those of any of the above sponsoring entities.

The work described in this volume includes current research at the Laboratory for Laser Energetics, which is supported by New York State Energy Research and Development Authority, the University of Rochester, the U.S. Department of Energy Office of Inertial Confinement Fusion under Cooperative Agreement No. DE-FC03-92SF19460, and other agencies.

Printed in the United States of America
Available from
National Technical Information Services
U.S. Department of Commerce
5285 Port Royal Road
Springfield, VA 22161

Price codes: Printed Copy A04
Microfiche A01

For questions or comments, contact Timothy J. B. Collins, *Editor*, Laboratory for Laser Energetics, 250 East River Road, Rochester, NY 14623-1299, (585) 275-8245.

Worldwide-Web Home Page: http://www.lle.rochester.edu/

UNIVERSITY OF ROCHESTER
LABORATORY FOR LASER ENERGETICS

Volume 92
July–September 2002
DOE/SF/19460-465

# LLE Review

## Quarterly Report

UR LLE

## Contents

In Brief ..... iii

Radial Structure of Shell Modulations Near Peak Compression of Spherical Implosions ..... 151

A TIM-Based Neutron Temporal Diagnostic for Cryogenic Experiments on OMEGA ..... 156

Carbon Activation Diagnostic for Tertiary Neutron Measurements ..... 161

The Properties of Polyimide Targets ..... 167

Anomalous Stimulated Raman Scattering and Electron Acoustic Waves in Laser-Produced Plasmas: A Linear Model .... 181

Time Delay of the Resistive-State Formation in Superconducting Stripes Excited by Single Optical Photons ..... 186

LLE's Summer High School Research Program ..... 190

FY02 Laser Facility Report ..... 192

National Laser Users' Facility and External Users' Programs ..... 194

Publications and Conference Presentations

# In Brief

This volume of the LLE Review, covering July–September 2002, features an investigation of the radial structure of shell modulations near peak compression of spherical implosions, by V. A. Smalyuk, S. B. Dumanis, F. J. Marshall, J. A. Delettrez, D. D. Meyerhofer, T. C. Sangster, and B. Yaakobi (p. 151). They describe the measurement of the structure of shell modulations at peak compression of implosions using absorption of titanium-doped layers placed at various distances from the inner surface of 20-$\mu$m-thick plastic shells filled with $D^3He$ gas. Their results show that the peak-compression, time-integrated areal-density modulations are higher at the inner shell surface, which is unstable during the acceleration phase of an implosion, than in the central part of the shell. The outer surface of the shell, which is unstable during the acceleration phase of an implosion, has a modulation level comparable to that of the inner shell surface.

Additional highlights of research presented in this issue include the following:

- Measurements of the neutron emission from inertial confinement fusion (ICF) implosions provide important information about target performance that can be compared directly with numerical models. For room-temperature target experiments on OMEGA at the Laboratory for Laser Energetics (LLE) the neutron temporal diagnostic (NTD), originally developed at Lawrence Livermore National Laboratory (LLNL), is used to measure the neutron burn history with high resolution and good timing accuracy. Since the NTD is mechanically incompatible with cryogenic target experiments because of the standoff required to remain clear of the Cryogenic Target Handling System, a new cryogenic-compatible neutron temporal diagnostic (cryoNTD) has been designed for LLE's standard ten-inch-manipulator (TIM) diagnostic inserters. This instrument provides high-resolution neutron emission measurements for cryogenic implosions. C. Stoeckl, V. Yu. Glebov, S. Roberts, and T. C. Sangster of LLE along with R. A. Lerche, R. L. Griffith, and C. Sorce of LLNL (p. 156) present the first experimental results of the performance of cryoNTD and compare them to NTD measurements of room-temperature direct-drive implosions.

- V. Yu. Glebov, C. Stoeckl, T. C. Sangster, D. D. Meyerhofer, and P. B. Radha of LLE along with S. Padalino, L. Baumgart, R. Colburn, and J. Fuschino of SUNY Geneseo (p. 161) report on the use of carbon activation as a diagnostic for tertiary neutron measurements. The yield of tertiary neutrons with energies greater than 20 MeV has been proposed as a method to determine the areal mass density of ICF targets. Carbon activation is a suitable measurement technique because of its high reaction threshold and the availability of high-purity samples. The isotope $^{11}C$ decays with a half-life of 20.3 min and emits a positron, resulting in the production of two back-to-back, 511-keV gamma rays upon annihilation. The present copper activation gamma-detection system can be used to detect tertiary-produced carbon activation because the positron decay of $^{11}C$ is nearly identical to the copper decay used in the activation measurements of 14.1-MeV primary deuterium–tritium (DT) yields. Because the tertiary neutron yield is more than six orders of magnitude lower than primary neutron yield, the carbon activation diagnostic requires ultrapure carbon samples, free from any positron-emitting contamination. Carbon purification, packaging, and handling procedures developed in recent years that reduce the contamination signal to a level low enough for OMEGA are presented. Potential implementation of a carbon activation system for the National Ignition Facility (NIF) are also discussed.

- D. Harding, F. Y. Tsai, and R. Q. Gram (p. 167) describe the development of polyimide shells suitable for ICF cryogenic experiments on OMEGA. They have also determined the associated mechanical properties needed to define the processing conditions for operating the OMEGA Cryogenic Target Handling System (CTHS). Overall, polyimide targets offer a viable alternative to plasma polymer capsules currently in use. The principal advantages of the polyimide material are its high radiation resistance for tritium application and its excellent mechanical properties, which lessen the demanding specifications for the equipment needed to provide cryogenic targets. The single biggest limitation to using polyimide, based on PMDA-ODA chemistry, is the low permeability of the material at room temperature. Methods to increase the permeability are described.

- R. W. Short (p. 181) presents a linear model of anomalous stimulated Raman scattering from electron-acoustic waves in laser-produced plasmas. Stimulated Raman scattering (SRS) from heavily Landau-damped plasma waves and from electron-acoustic (EA) waves has recently been attributed to nonlinear Bernstein–Green–Kruskal (BGK) wave modes. These phenomena find a simpler, more comprehensive explanation in terms of linear waves in a locally flattened distribution function. The flattening arises from Landau damping of SRS plasma waves (in the case of anomalous SRS) or from perturbations at the EA phase velocity that are then maintained by SRS. Local flattening allows undamped linear EA waves to propagate, as in the original description of these waves by Stix.

- J. Zhang, W. Slysz, A. Verevkin, and Roman Sobolewski of LLE and the University of Rochester along with O. Okunev and G. N. Gol'tsman of Moscow State Pedagogical University (p. 186) have measured the time delay of the resistive-state formation in superconducting NbN stripes illuminated by single optical photons. They observed a 65(±5)-ps time delay in the onset of a resistive-state formation in 10-nm-thick, 200-nm-wide NbN superconducting stripes exposed to single photons. This delay in the photoresponse decreased down to zero when the stripe was irradiated by multiphoton (classical) optical pulses. The NbN structures were kept at 4.2 K, well below the material's critical temperature, and were illuminated by 100-fs-wide optical pulses. The time-delay phenomenon is explained within the framework of a model based on photon-induced generation of a hotspot in the superconducting stripe and subsequent, supercurrent-assisted resistive-state formation across the entire stripe cross section. The measured time delays in both the single-photon and two-photon detection regimes agree well with the Tinkham model's theoretical predictions of the resistive-state dynamics in narrow, ultrathin superconducting stripes.

- This volume concludes with a summary of LLE's Summer High School Research Program (p. 190), the FY02 Laser Facility Report (p. 192), and the National Laser Users' Facility and External Users' Programs (p. 194).

Timothy J. B. Collins
*Editor*

# Radial Structure of Shell Modulations Near Peak Compression of Spherical Implosions

## Introduction

In inertial confinement fusion (ICF), a spherical target is imploded by either direct illumination of laser beams (direct drive)[1] or x rays produced in a high-$Z$ enclosure (hohlraum).[2] The growth of shell perturbations is the greatest factor limiting target performance in these implosions. Initial nonuniformities in the shell include target imperfections and modulations from laser nonuniformities in the case of direct-drive ICF.[3–8] These modulations initially grow at the shell's outer surface during the laser-driven part of implosions due to the acceleration-phase Rayleigh–Taylor (RT) instability[9–12] and convergent Bell–Plesset (BP) effects.[13] These outer-surface perturbations feed through the shell during their acceleration-phase growth, seeding the deceleration-phase RT instability[14–18] on the inner surface. As the shell starts to decelerate, the outer-shell modulations become stable. The inner surface of the shell, however, is subject to the RT instability during the deceleration phase since the higher-density shell is slowed down by the lower-density gas of the target core.[14–18] As a result, the shell modulations penetrate deep into the gas fuel region causing shell–fuel mixing.[19–21] This mixing inhibits the achievement of high compression and reduces the fuel temperature that is necessary to sustain efficient fuel burn.

The first measurements[18,22] of shell modulations around peak compression were based on differential imaging[22] of core emission with shells having diagnostic titanium-doped layers. At peak compression, when the maximum density and temperature occur, the hot, compressed core and inner surface of the shell produce strong x-ray emission. This emission is used as a backlighter to probe the outer, colder shell.[22] To measure shell integrity, both time-integrated[22] and time-resolved[18] measurements used imaging at photon energies above and below the titanium $K$ edge. Core images at photon energies below the $K$ edge (not absorbed by the shell) provide the spatial shape of the backlighter, while core images at photon energies above the $K$ edge (highly absorbed by the shell's titanium) contain information about the structure of shell-areal-density modulations in the titanium-doped layer.

Earlier experiments[18,22] were limited to measurements of perturbations at the shell's inner surface, where modulations and compression were expected to be the highest. Measurements with titanium-doped layers placed in the central and outer parts of the shell were not sensitive enough to detect perturbations. Differential imaging in the current experiments is extended to the much more sensitive absorption in the titanium 1$s$–2$p$ spectral region instead of the absorption above the $K$ edge. Near peak compression, the shell is heated by energy transported from the hot core through thermal conduction and radiation. At temperatures around 0.1 to 1 keV, the shell titanium is partially ionized and is able to absorb core radiation not only at photon energies above the $K$ edge ($\geq$ 4.966 keV) but also in the 1$s$–2$p$ absorption line region at photon energies around 4.5 to 4.75 keV. The mass absorption rate of any absorption line from the titanium 1$s$–2$p$ spectral region is about one order of magnitude higher than at photon energies above the $K$ edge. As a result, differential imaging can be extended to the central and outer parts of the shell, where the compression and modulations are smaller. In this article the first measurements of the compressed-shell modulation structure away from the inner surface are presented. A similar technique has also been employed for modulation measurements in indirectly driven implosions.[23]

## Experimental Conditions

Figure 92.1 shows a schematic of spherical targets and the positions of the titanium-doped layers in the shell used in these experiments and their predicted location at peak compression. Targets with ~450-$\mu$m initial radii and 20-$\mu$m-thick shells, filled with 18 atm of $D^3He$ gas, were imploded by 351-nm laser light using the 60-beam OMEGA laser system[24] with a 1-ns square pulse and a total energy of ~23 kJ. All shots were taken with laser beams smoothed by distributed phase plates (DPP's),[25] 1-THz, two-dimensional smoothing by spectral dispersion (2-D SSD),[26] and polarization smoothing (PS)[27] using birefringent wedges. The average beam-to-beam energy imbalance was ~3% in all implosions. The diagnostic, 1-$\mu$m-thick, titanium-doped (~2% by atom) CH layers were offset

from the inner surface by ~1, 5, 7, and 9 $\mu$m of pure CH. These layers were expected to determine shell-areal-density modulations at the inner, central, and outer parts of the shell at peak compression. Figure 92.1(b) shows the temperature and density profiles at peak compression of one of the targets calculated by the 1-D code *LILAC*.[28] At peak compression, the diagnostic titanium layer offset by 1 $\mu$m is located on the slope of the density profile at the inner shell, where the unstable surface is located. Titanium layers offset by 5 $\mu$m and 7 $\mu$m are in the central part of the shell, and the layer offset by 9 $\mu$m lies in the outer part of the shell at peak compression [see Fig. 92.1(b)].

Core images were measured with a gated monochromatic x-ray imager (GMXI),[29] which was set up for time-integrated (~200-ps) measurements during these experiments. One channel of the GMXI recorded monochromatic (with FWHM of ~30 eV) images at ~4.60 keV in the spectral region of titanium 1*s*–2*p* absorption, while the other channel was set up at ~4.87 keV outside titanium absorption regions or emission lines. Figure 92.2 shows Wiener-filtered images[30] for shots with titanium layers offset by 1, 5, 7, and 9 $\mu$m and for one shot without titanium, which was used to estimate the noise level. The Wiener filter used a noise level constructed from the difference of two images $I_{1s-2p}(\mathbf{r})$ and $I_{<K}(\mathbf{r})$ in shot

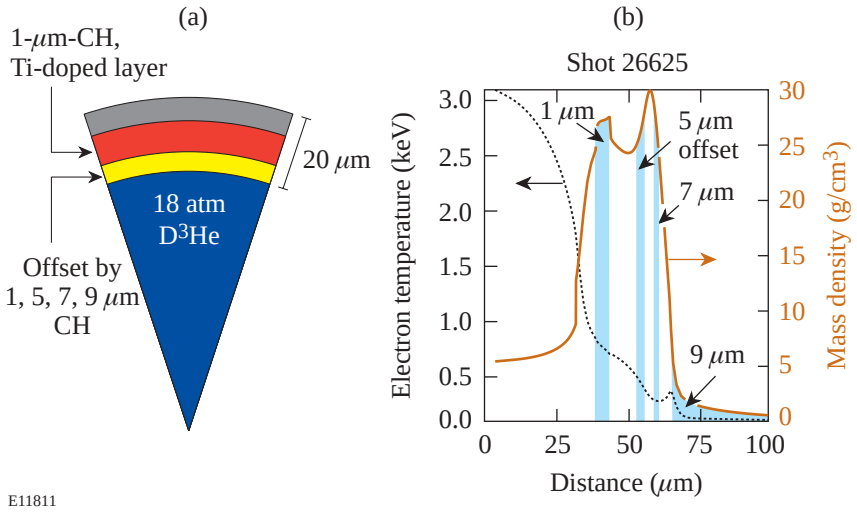


Figure 92.1
(a) Schematic of spherical targets with diagnostic titanium-doped (2% by atom) layers offset by 1, 5, 7, and 9 $\mu$m of pure CH from the inner surface. (b) *LILAC*-simulated profiles of target density and temperature at peak compression of the implosion. The locations of titanium-doped layers are shown by the light blue areas.

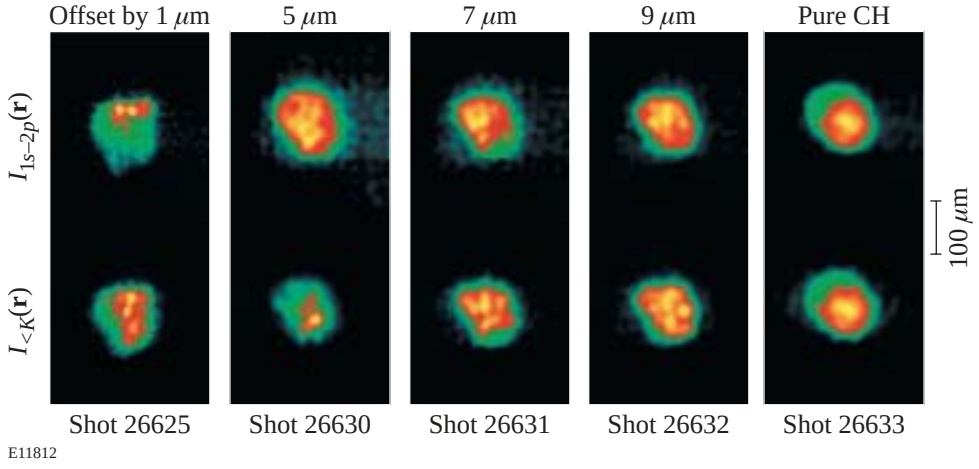


Figure 92.2
Wiener-filtered core images around peak compression at energies inside (~4.60 keV, upper row of images) and outside (~4.87 keV, lower row of images) the titanium 1*s*–2*p* absorption spectral region for shots with 1-$\mu$m- (shot 26625), 5-$\mu$m- (shot 26630), 7-$\mu$m- (shot 26631), and 9-$\mu$m-offset (shot 26632) titanium-doped layers, and for the shot without titanium (26633).

26633 without titanium and the measured GMXI modulation transfer function (MTF).[31] All the details of the image processing are described in Refs. 18, 22, and 30. The shell optical-depth (OD) modulations were calculated using the natural logarithm of the ratio of intensities of the two images at photon energies in the 1*s*–2*p* spectral region (highly absorbed by the shell), $I_{1s-2p}(\mathbf{r})$, and outside the 1*s*-2*p* region, below the *K* edge (weakly absorbed by the shell), $I_{<K}(\mathbf{r})$:

$$\delta[\mathrm{OD}(\mathbf{r})] = \delta\left\{\ln\left[I_{1s-2p}(\mathbf{r})/I_{<K}(\mathbf{r})\right]\right\}.$$

The spectra of the core emissions were captured on an x-ray streak camera.[32] They were subsequently time integrated and used to infer a spatial average of the OD of the titanium layer in the 1*s*–2*p* spectral region. The red line (shot 26625) in Fig. 92.3(a) shows an example of a measured time-integrated spectrum $S_{\mathrm{meas}}(E)$ as a function of photon energy $E$. The spectral responses of the GMXI at two channels in $[R_{1s-2p}(E)]$ and out $[R_{<K}(E)]$ of the 1*s*–2*p* absorption spectral region are represented by the dashed and dotted lines, respectively. The thick green line represents the estimated continuum level $S_{\mathrm{con}}(E)$ of core x rays, used to calculate average titanium optical depth $\mathrm{OD} = \ln\left[S_{\mathrm{con}}(E)/S_{\mathrm{meas}}(E)\right]$ at a photon energy of $E = 4.6$ keV. The average titanium OD is used to determine the relative OD modulations (which are equal to the relative areal-density modulations), $\delta[\mathrm{OD}(\mathbf{r})]/\mathrm{OD} = \delta[\rho R(\mathbf{r})]/\rho R$, to compare levels of modulations in the different parts of the shell.

In addition, the measured spectra are used to calculate the spatial variations in images due to small variations in the spectral response across the vertical axis of the images. For example, the central part of the image $I_{1s-2p}(\mathbf{r})$ is set up for measurements at a photon energy of $E = 4.60$ keV. The x rays originating at this point of the image are reflected at an angle of 5.88±0.01° from the GMXI multilayer mirror. The x rays originating from the horizontal line at 100 $\mu$m off the image center are reflected from the mirror at a slightly different angle of 5.91±0.01°, corresponding to a photon energy of 4.58 keV. Similarly, the x rays originating at the horizontal line at –100 $\mu$m off the center line in the image plane are reflected from the mirror at an angle of 5.85±0.01°, corresponding to a photon energy of 4.63 keV. The resulting image correction functions were calculated for each shot using corresponding spectra. For example, for the images at the 1*s*–2*p* absorption channel, the resulting correction function is proportional to the convolution of the measured spectrum $S_{\mathrm{meas}}(E)$ with the spectral response function $R_{1s-2p}(E)$. Figure 92.3(b) shows correction functions for shot 26625 inside (dashed line) and outside (dotted line) the 1*s*–2*p* absorption channel. For each Wiener-filtered image, the x-ray intensity at the vertical axis was divided by the corresponding correction function to compensate for these spatial variations.

## Experimental Results

Figure 92.4 presents the images of optical-depth modulations in the titanium-doped layers offset by 1, 5, 7, and 9 $\mu$m from the shell's inner surface. As shown in Fig. 92.1(b), these layers represent different parts of the shell ranging from the inner to the outer surfaces at peak compression. Power-per-mode spectra of these modulations as functions of spatial frequency are presented in Fig. 92.5(a). The amplitudes of modulations are highest at a spatial frequency of ~20 mm$^{-1}$ corresponding to a wavelength of ~50 $\mu$m (with a mode number of $\ell \sim 6$). This result is in agreement with previous inner-surface measurements using *K*-edge imaging. The absolute values of optical-depth modulation $\sigma_{\mathrm{rms}}$ decreased monotonically from 0.30±06 at the inner surface to 0.13±06 at the outer surface as shown by the solid line in Fig. 92.5(b). The relative areal-

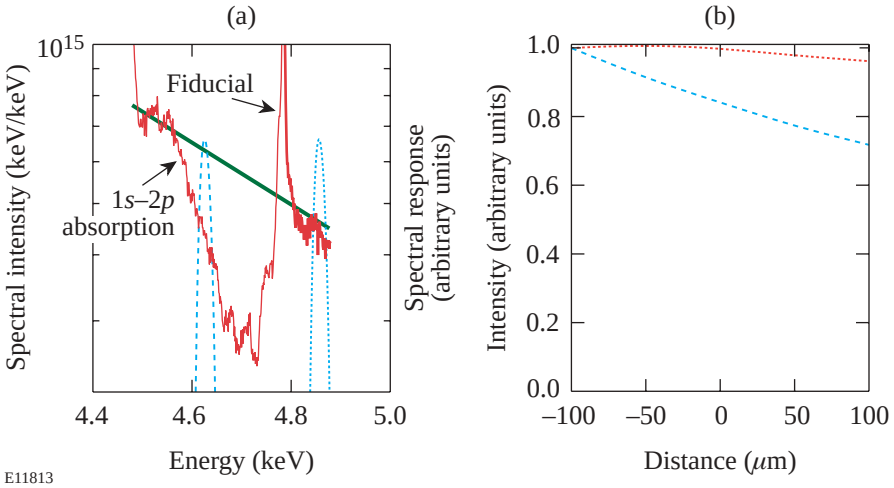


Figure 92.3
(a) Measured time-integrated spectrum $S_{\mathrm{meas}}(E)$ as a function of photon energy for shot 26625 (red line). Estimated continuum level $S_{\mathrm{con}}(E)$ as a function of photon energy (thick green line). The instrumental spectral responses as functions of photon energy of GMXI channels inside $[R_{1s-2p}(E)$, dashed line] and outside $[R_{<K}(E)$, dotted line] the titanium 1*s*–2*p* absorption region. (b) The spatial correction functions as a function of distance in the vertical axis for images inside (dashed line) and outside (dotted line) the titanium 1*s*–2*p* absorption region.

density modulation $\sigma_{rms}$ is 59±14%, 18±5%, 26±10%, and 52±20% in the layers offset by 1, 5, 7, and 9 $\mu$m, respectively, as shown by the dashed line in Fig. 92.5(b). The modulations are highest at the inner surface (in the 1-$\mu$m-offset layer), which is unstable during the deceleration phase of implosion near peak compression. As expected, the modulations decrease in the bulk of the shell (in the 5- and 7-$\mu$m-offset layers) but then increase at the outer surface (in the 9-$\mu$m-offset layer), which was unstable during the acceleration, laser-driven phase of the implosion. The areal-density modulations in the whole shell are dominated by nonuniformities in the inner and central parts of the shell. The contribution of outer shell modulations is small because of the small compression at the outer surface. As shown in Fig. 92.1(b), the 9-$\mu$m-offset layer is expected to be outside the compressed shell, and therefore its high modulation level is not very important to the integrity of the whole shell. The measured level of modulation at the inner surface, 59±14%, is in agreement with previous results[22] measured at peak compression. For comparison, at peak neutron production, ~100 ps earlier than the peak compression, previous time-resolved measurements have shown lower modulation levels, about 20% at the inner surface.[18] In the future, experiments will extend the time-integrated measurements of modulations in the central and outer parts of the shell to time-resolved measurements using the same titanium 1*s*–2*p* absorption technique.

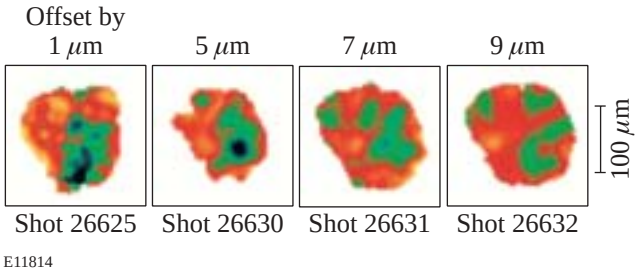


Figure 92.4
Optical-depth-modulation images at peak compression for shots with 1-$\mu$m- (shot 26625), 5-$\mu$m- (shot 26630), 7-$\mu$m- (shot 26631), and 9-$\mu$m-offset (shot 26632) titanium-doped layers integrated over ~200 ps of x-ray emission.

## Conclusions

This article has presented the first time-integrated measurements of the compressed-shell modulation structure away from the inner surface. The differential imaging technique has replaced previous titanium *K*-edge imaging with much more sensitive imaging using the titanium 1*s*–2*p* absorption spectral region. As a result, measurements of modulations at central and outer parts of the shell have become accessible. In implosions with the 20-$\mu$m-thick shells, the relative areal-density modulation $\sigma_{rms}$ is 59±14%, 18±5%, 26±10%, and 52±20%, in layers offset by 1, 5, 7, and 9 $\mu$m, respectively. The spatial spectra of modulations peaked at a spatial frequency of ~20 mm$^{-1}$ corresponding to a wavelength of ~50 $\mu$m (with a mode number of $\ell \sim 6$). The areal-density modulations in the whole shell are dominated by modulations in the inner and central parts of the shell, while the contribution of outer shell modulations is small because of the smaller compression at the outer surface.

## ACKNOWLEDGMENT

This work was supported by the U.S. Department of Energy Office of Inertial Confinement Fusion under Cooperative Agreement No. DE-FC03-92SF19460, the University of Rochester, and the New York State Energy Research and Development Authority. The support of DOE does not constitute an endorsement by DOE of the views expressed in this article.

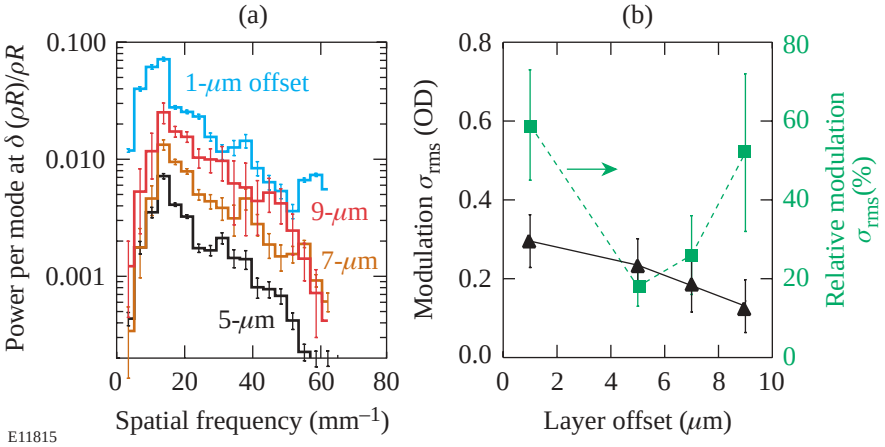


Figure 92.5
(a) Power per mode as a function of spatial frequency of relative areal-density modulations at peak compression for shots with 1-, 5-, 7-, and 9-$\mu$m-offset titanium-doped layers. (b) Peak compression optical-depth modulation $\sigma_{rms}$ (solid line) and relative areal-density modulation $\sigma_{rms}$ (dashed line) as functions of the layer offset.

## REFERENCES


1. J. Nuckolls *et al.*, Nature **239**, 139 (1972).
2. J. D. Lindl, *Inertial Confinement Fusion: The Quest for Ignition and Energy Gain Using Indirect Drive* (Springer-Verlag, New York, 1998), Chap. 6, pp. 61–82.
3. C. J. Pawley *et al.*, Phys. Plasmas **6**, 565 (1999).
4. H. Azechi *et al.*, Phys. Plasmas **4**, 4079 (1997).
5. R. J. Taylor *et al.*, Phys. Rev. Lett. **76**, 1643 (1996).
6. D. H. Kalantar, M. H. Key, L. B. Da Silva, S. G. Glendinning, B. A. Remington, J. E. Rothenberg, F. Weber, S. V. Weber, E. Wolfrum, N. S. Kim, D. Neely, J. Zhang, J. S. Wark, A. Demir, J. Lin, R. Smith, G. J. Tallents, C. L. S. Lewis, A. MacPhee, J. Warwick, and J. P. Knauer, Phys. Plasmas **4**, 1985 (1997).
7. V. A. Smalyuk, T. R. Boehly, D. K. Bradley, V. N. Goncharov, J. A. Delettrez, J. P. Knauer, D. D. Meyerhofer, D. Oron, and D. Shvarts, Phys. Rev. Lett. **81**, 5342 (1998).
8. T. R. Boehly, V. N. Goncharov, O. Gotchev, J. P. Knauer, D. D. Meyerhofer, D. Oron, S. P. Regan, Y. Srebro, W. Seka, D. Shvarts, S. Skupsky, and V. A. Smalyuk, Phys. Plasmas **8**, 2331 (2001).
9. S. G. Glendinning, S. N. Dixit, B. A. Hammel, D. H. Kalantar, M. H. Key, J. D. Kilkenny, J. P. Knauer, D. M. Pennington, B. A. Remington, R. J. Wallace, and S. V. Weber, Phys. Rev. Lett. **78**, 3318 (1997).
10. K. S. Budil *et al.*, Phys. Rev. Lett. **76**, 4536 (1996).
11. K. S. Budil *et al.*, Phys. Plasmas **8**, 2344 (2001).
12. J. P. Knauer, R. Betti, D. K. Bradley, T. R. Boehly, T. J. B. Collins, V. N. Goncharov, P. W. McKenty, D. D. Meyerhofer, V. A. Smalyuk, C. P. Verdon, S. G. Glendinning, D. H. Kalantar, and R. G. Watt, Phys. Plasmas **7**, 338 (2000).
13. M. S. Plesset and T. P. Mitchell, Q. Appl. Math. **13**, 41 (1956).
14. H. Sakagami and K. Nishihara, Phys. Rev. Lett. **65**, 432 (1990).
15. R. P. J. Town and A. R. Bell, Phys. Rev. Lett. **67**, 1863 (1991).
16. M. C. Herrmann, M. Tabak, and J. D. Lindl, Phys. Plasmas **8**, 2296 (2001).
17. R. Betti, K. Anderson, V. N. Goncharov, R. L. McCrory, D. D. Meyerhofer, S. Skupsky, and R. P. J. Town, Phys. Plasmas **9**, 2277 (2002).
18. V. A. Smalyuk, J. A. Delettrez, V. N. Goncharov, F. J. Marshall, D. D. Meyerhofer, S. P. Regan, T. C. Sangster, R. P. J. Town, and B. Yaakobi, Phys. Plasmas **9**, 2738 (2002).
19. S. P. Regan, J. A. Delettrez, F. J. Marshall, J. M. Soures, V. A. Smalyuk, B. Yaakobi, V. Yu. Glebov, P. A. Jaanimagi, D. D. Meyerhofer, P. B. Radha, W. Seka, S. Skupsky, C. Stoeckl, R. P. J. Town, D. A. Haynes, Jr., I. E. Golovkin, C. F. Hooper, Jr., J. A. Frenje, C. K. Li, R. D. Petrasso, and F. H. Séguin, Phys. Rev. Lett. **89**, 085003 (2002).
20. D. D. Meyerhofer, J. A. Delettrez, R. Epstein, V. Yu. Glebov, V. N. Goncharov, R. L. Keck, R. L. McCrory, P. W. McKenty, F. J. Marshall, P. B. Radha, S. P. Regan, S. Roberts, W. Seka, S. Skupsky, V. A. Smalyuk, C. Sorce, C. Stoeckl, J. M. Soures, R. P. J. Town, B. Yaakobi, J. D. Zuegel, J. Frenje, C. K. Li, R. D. Petrasso, D. G. Hicks, F. H. Séguin, K. Fletcher, S. Padalino, M. R. Freeman, N. Izumi, R. Lerche, T. W. Phillips, and T. C. Sangster, Phys. Plasmas **8**, 2251 (2001).
21. P. B. Radha, J. Delettrez, R. Epstein, V. Yu. Glebov, R. Keck, R. L. McCrory, P. McKenty, D. D. Meyerhofer, F. Marshall, S. P. Regan, S. Roberts, T. C. Sangster, W. Seka, S. Skupsky, V. Smalyuk, C. Sorce, C. Stoeckl, J. Soures, R. P. J. Town, B. Yaakobi, J. Frenje, C. K. Li, R. Petrasso, F. Séguin, K. Fletcher, S. Padalino, C. Freeman, N. Izumi, R. Lerche, and T. W. Phillips, Phys. Plasmas **9**, 2208 (2002).
22. B. Yaakobi, V. A. Smalyuk, J. A. Delettrez, F. J. Marshall, D. D. Meyerhofer, and W. Seka, Phys. Plasmas **7**, 3727 (2000).
23. J. Koch, Lawrence Livermore National Laboratory, private communication (2002).
24. T. R. Boehly, D. L. Brown, R. S. Craxton, R. L. Keck, J. P. Knauer, J. H. Kelly, T. J. Kessler, S. A. Kumpan, S. J. Loucks, S. A. Letzring, F. J. Marshall, R. L. McCrory, S. F. B. Morse, W. Seka, J. M. Soures, and C. P. Verdon, Opt. Commun. **133**, 495 (1997).
25. Y. Lin, T. J. Kessler, and G. N. Lawrence, Opt. Lett. **20**, 764 (1995).
26. S. P. Regan, J. A. Marozas, J. H. Kelly, T. R. Boehly, W. R. Donaldson, P. A. Jaanimagi, R. L. Keck, T. J. Kessler, D. D. Meyerhofer, W. Seka, S. Skupsky, and V. A. Smalyuk, J. Opt. Soc. Am. B **17**, 1483 (2000).
27. T. R. Boehly, V. A. Smalyuk, D. D. Meyerhofer, J. P. Knauer, D. K. Bradley, R. S. Craxton, M. J. Guardalben, S. Skupsky, and T. J. Kessler, J. Appl. Phys. **85**, 3444 (1999).
28. J. Delettrez, R. Epstein, M. C. Richardson, P. A. Jaanimagi, and B. L. Henke, Phys. Rev. A **36**, 3926 (1987).
29. F. J. Marshall and J. A. Oertel, Rev. Sci. Instrum. **6**, 735 (1997).
30. V. A. Smalyuk, T. R. Boehly, L. S. Iwan, T. J. Kessler, J. P. Knauer, F. J. Marshall, D. D. Meyerhofer, C. Stoeckl, B. Yaakobi, and D. K. Bradley, Rev. Sci. Instrum. **72**, 635 (2001).
31. F. J. Marshall, M. M. Allen, J. P. Knauer, J. A. Oertel, and T. Archuleta, Phys. Plasmas **5**, 1118 (1998).
32. D. H. Kalantar *et al.*, Rev. Sci. Instrum. **72**, 751 (2001).

# A TIM-Based Neutron Temporal Diagnostic for Cryogenic Experiments on OMEGA

## Introduction

In inertial confinement fusion[1] experiments, shells filled with deuterium ($D_2$) or a deuterium–tritium (DT) mixture are heated by either direct laser illumination or soft x-ray radiation in a laser-heated hohlraum. The target is compressed to conditions under which thermonuclear fusion occurs. The most-promising target designs consist of a layered cryogenic $D_2$ or DT shell enclosed by a very thin shell of plastic, which is ablated very early and does not contribute significantly to the dynamics of the implosion.[2,3] During the plasma confinement time, which is of the order of 100 ps, fuel atoms undergoing fusion release energetic charged particles, photons, and neutrons. The fusion reactions of interest are

$$\begin{aligned} &D + D \rightarrow n\ (2.45\ \text{MeV}) + {}^3\text{He}\ (0.82\ \text{MeV}), \\ &D + D \rightarrow p\ (2.5\ \text{MeV}) + T\ (1.01\ \text{MeV}), \\ &T + D \rightarrow \alpha\ (3.5\ \text{MeV}) + n\ (14.1\ \text{MeV}). \end{aligned} \tag{1}$$

The particle energies are shown in parentheses. While most of the charged particles are slowed down in the plasma and stopped, or "ranged out," before they leave the target, most neutrons escape the fuel without collision. As a result, the time history of neutrons arriving at an external diagnostic represents the burn history of the target fuel. Measurements of the neutron burn history provide important information about target performance that can be compared directly with numerical models. The time of peak neutron emission—the "neutron bang time"—is very sensitive to the details of the energy absorption and the equation of state used to describe the plasma. The neutron burn history contains valuable information about the plasma evolution close to the peak of compression. Target and laser illumination nonuniformities can feed through to the inner surface of the shell by the deceleration phase. Amplified by the Rayleigh–Taylor growth, these nonuniformities can severely disrupt the hot, neutron-producing region of the target, leading to a strongly distorted neutron burn history. Several detectors measuring the neutron bang time[4–8] are described in the literature, but only the streak-camera–based neutron temporal diagnostic[9] (NTD) is capable of resolving the details of the neutron burn history with a resolution of ~50 ps for DD neutrons and ~25 ps for DT neutrons. The NTD is currently installed on LLE's OMEGA laser. NTD is a highly successful instrument,[10] but the size of the cryogenic target shroud system prevents placing the scintillator of the NTD system at its optimum location close to the target. This makes it too insensitive to record the burn history of the current $D_2$ cryogenic target experiments. Furthermore, Doppler broadening of the neutron spectrum severely compromises the time resolution of NTD at larger distances.[9] These mechanical constraints motivated the development of new cryogenic-compatible neutron temporal diagnostic (cryoNTD), which fits into LLE's standard ten-inch manipulator (TIM) diagnostic inserters, to provide high-resolution neutron emission measurements for cryogenic implosions. This article describes the setup of cryoNTD and first experimental results compared to NTD on room-temperature direct-drive implosions and on cryogenic implosions.

## Setup of the Detector System

The cryoNTD system, shown schematically in Fig. 92.6, is based on a fast plastic scintillator (Bicron BC422[11]), which converts the kinetic energy of the neutrons into light. A light collection and transfer system (Fig. 92.7) transports the light from the scintillator to the input plane of a fast (<15-ps) optical streak camera.[12] The front end of the optical system is mounted in the TIM and inserted close to the target. An optical fiducial is used to time the neutron signals relative to the incident laser pulse. The size of the scintillator is that required to record high-quality burn histories at a yield comparable to $10^{10}$, which is the performance of the early cryogenic $D_2$ target implosions on OMEGA.[3] A simple scaling from the sensitivity of NTD with a 6-mm-diam scintillator at 2 cm from the target to the required standoff distance of 9 cm shows that a 30-mm-diam scintillator is sufficient. Due to the limited size of the photocathode of the streak camera, a demagnifying optical system

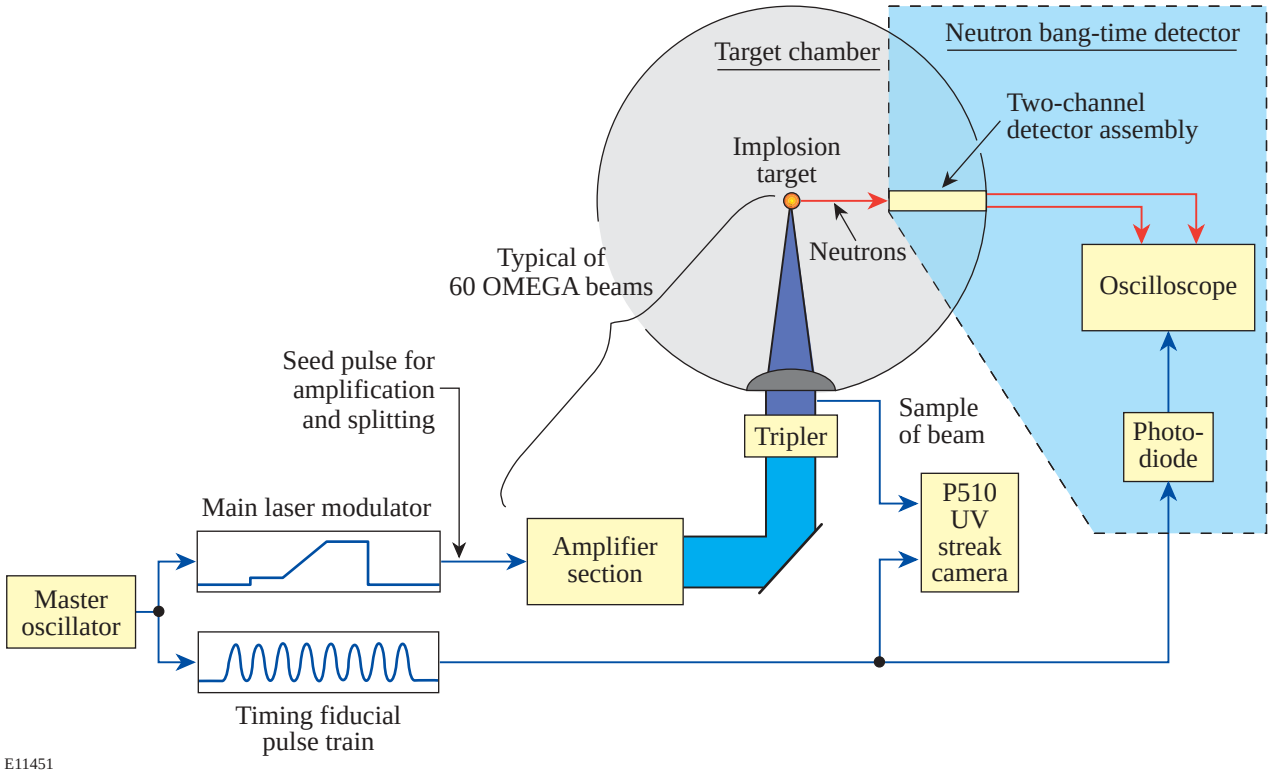


Figure 92.6
A block diagram of the cryoNTD detector system integrated into the OMEGA facility. The fiducial system provides cross timing between the neutron signals and the incident laser pulse, which is recorded on the P510 UV streak camera.

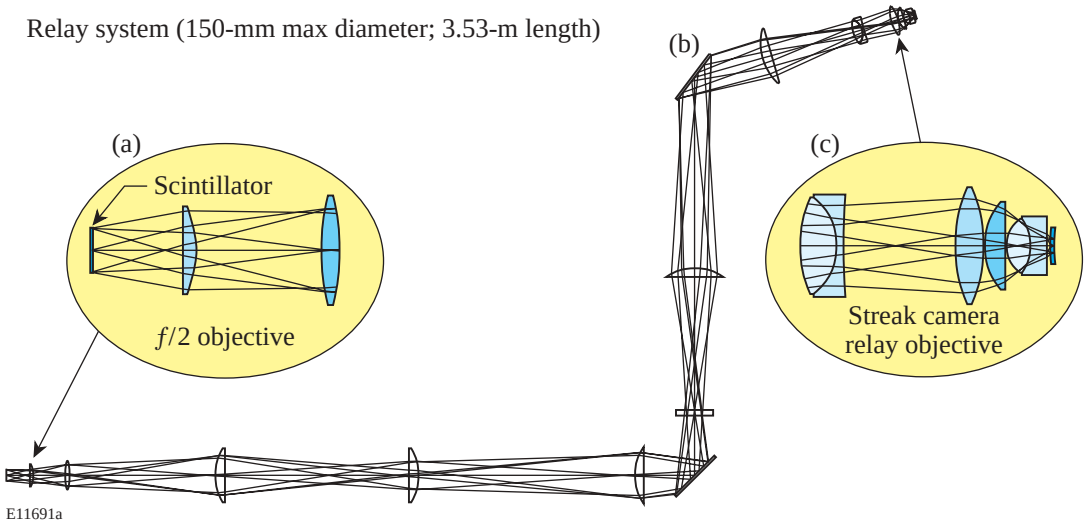


Figure 92.7
A fast scintillator converts the neutron kinetic energy into light, which is collected by a fast *f*/2 optic (a). An optical system (b) transports the light to the input plane of a fast optical streak camera with 3:1 demagnification though an *f*/0.67 final lens system (c).

with a 3:1 ratio is used. A fast *f*/2 lens collects the light from the scintillator with high efficiency [Fig. 92.7(a)]. An optical system consisting of 11 lenses and 2 mirrors relays the image of the scintillator though the TIM and the vacuum window along a 3.5-m optical path to the streak camera [Fig. 92.7(b)]. The 3:1 demagnification in combination with the fast *f*/2 lens leads to a very demanding *f*/0.67 final lens system, which maximizes the transmission of the optical system [Fig. 92.7(c)]. The 527-nm light from the OMEGA fiducial system is delivered via an optical fiber collimated and imaged onto the streak camera through the final lens assembly. The OMEGA fiducial consists of a series of eight pulses spaced 548 ps apart and is synchronized to the shaped OMEGA laser pulse with a jitter of less than 20 ps. The optical fiducial is amplified separately from the main laser pulse, split, and distributed to various diagnostic instruments for precision timing. The fiducial pulse train is also recorded on the P510 ultraviolet streak camera,[13] which measures the laser pulse shape. The common optical fiducial serves as a reference for both the neutron signal and the laser pulse, thus enabling very accurate timing of the cryoNTD signals.

The low light levels from the scintillator, the fast collection and transport optic, and the TIM design make it necessary to install a sophisticated system of shields and light baffles to avoid any scattered laser light from entering the optical system. Figure 92.8(a) shows a sample image from a cryogenic $D_2$ implosion with a yield of $3.17 \times 10^{10}$ recorded on the CCD camera attached to the optical streak camera. The fiducial is seen on top of the image and the scintillator output in the center. The "wings" seen on either side of the scintillator signal are most probably produced by the spatially nonuniform transmission of the optical system. Figure 92.8(b) shows image exposure versus time averaged across the central portion of the scintillator signal. The streak camera flat-field and geometric distortions are included in the signal processing. The time history of the scintillator signal is the convolution of the neutron temporal distribution with the scintillator response. The scintillator has a very fast rise time of <20 ps and a decay time of ~1.2 ns. Consequently the burn history information is encoded in the leading edge of the pulse due to the much longer decay of the scintillator compared to the burnwidth.

### Data Analysis and Calibration

The actual neutron burn history is obtained by deconvolving the effect of the long scintillator decay from the recorded signal. A "physical modeling" approach is used for the deconvolution, where the neutron signal $n_i$ at the pixel location $i$ is given as the recorded signal $s_i$ minus the sum of all earlier neutron signals, which are decaying exponentially at the scintillator fall time $\tau$:

$$n_i = s_i - \sum_{j=0}^{i-1} n_j \exp\left[\frac{(i-j)\times \Delta t_p}{\tau}\right]. \tag{2}$$

In this equation, $\Delta t_p$ is the time separation of two pixels. This method is fast and deterministic and is very stable against noise on the streak camera signal. The neutron signal is broadened by several different mechanisms. The thermal broadening of the neutron energy spectrum leads to an arrival time spread in the scintillator of[9]

$$\Delta t_T^{\mathrm{DD}} = 778 \frac{\mathrm{ps}}{m\ \mathrm{keV}^{1/2}} \sqrt{T} \times d \tag{3}$$

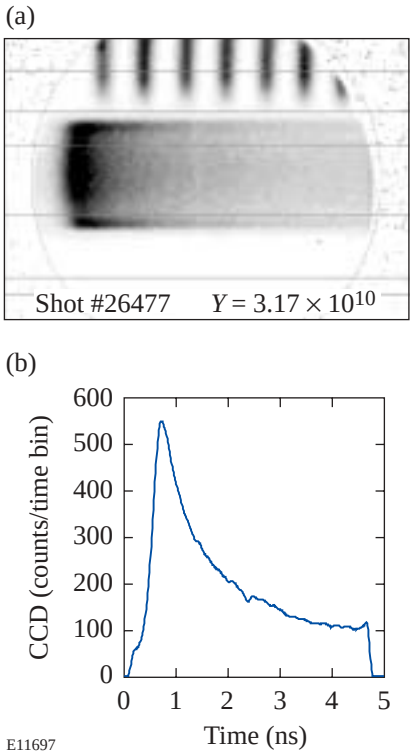


Figure 92.8
A streak camera image (a) of the neutron signal from a $D_2$ cryogenic implosion with a yield of $3.17 \times 10^{10}$. The fiducial seen on the top of the image is used for timing the neutron signal to the incident laser pulse. The image exposure versus time (b) is averaged across the central portion of the scintillator signal.

for DD neutrons, where $\Delta t_T$ is the FWHM in ps, $d$ is the target-to-detector distance in meters, and $T$ is the neutron-averaged ion temperature in keV. For the 9-cm standoff distance of cryoNTD, this effect limits the time resolution to ~70 ps at 1 keV. The finite neutron transit time through the scintillator $\Delta t_s = \Delta x / v_n$ broadens the signal by $\Delta t_s^{DD} = 44$ ps with a 1-mm-thick scintillator using a neutron speed of $v_n$ = 2.16 cm/ns. Adding both effects in quadrature gives an estimate of ~80 ps for the time resolution of cryoNTD. Figure 92.9 shows a comparison of the neutron burn histories obtained by NTD and cryoNTD on a room-temperature direct-drive OMEGA plastic target filled with 15 atm of $D_2$. The signals are aligned in time for best correlation to allow a better comparison. Although the effects of the limited time resolution of cryoNTD compared to NTD, which has a time resolution of ~50 ps for DD neutrons, can be seen, the burn histories compare very favorably.

Absolute timing is established using the OMEGA fiducial system. The recorded fiducial pulse is fitted by a pulse train of eight Gaussian pulses spaced apart at the well-characterized period of $d_t$ = 548 ps:

$$\text{fidu}(t) = \sum_{i=0}^{7} a_i \exp\left\{-\left[t-\left(t_0 + i \times dt\right)\right]^2 \Big/ 2\sigma^2\right\} \qquad (4)$$

to the recorded signal. Here $a_i$ is the amplitude of each fiducial peak, $t_0$ is the time of the first fiducial pulse, and $\sigma$ is the standard deviation of an individual fiducial pulse. This reduces the influence of noise on the determination of the timing reference. CryoNTD has been calibrated against NTD using a series of room-temperature plastic targets filled with $D_2$. The bang times measured by cryoNTD are very close to the bang times from NTD (Fig. 92.10), showing only 40-ps rms spread. Figure 92.11 shows a comparison of neutron burn histories from a direct-drive cryogenic target with a low-nonuniformity ice layer[3] and a cryogenic target with a very poor layer quality, both irradiated by a 1-ns, square, 23-kJ laser

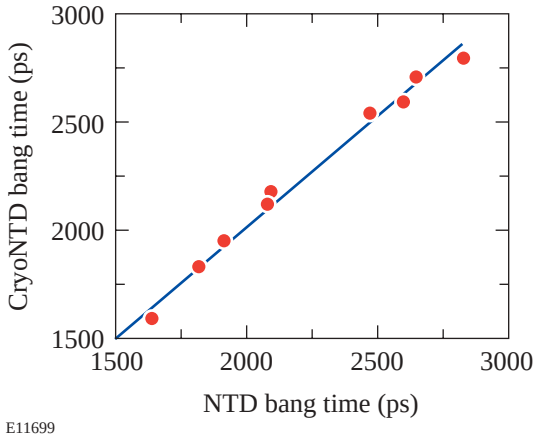


Figure 92.10
The bang times measured by the NTD compared to those of the cryoNTD for a series of room-temperature plastic targets.

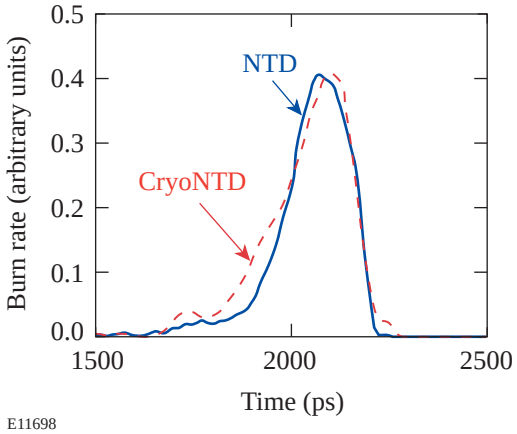


Figure 92.9
A comparison of the neutron burn histories recorded by the cryoNTD and the NTD from a room-temperature plastic target filled with 15 atm $D_2$ at a yield of $2 \times 10^{10}$.

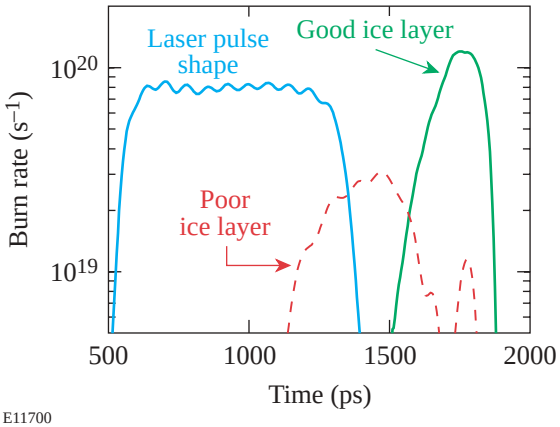


Figure 92.11
A comparison of neutron burn histories from direct-drive cryogenic targets with a good ice layer (solid line) and a poor ice layer (dashed line). Both targets are driven by a 1-ns square laser pulse.

pulse. The temporal shape of the laser pulse is shown for comparison. Even though the neutron yield of both implosions is relatively close—$1.5 \times 10^{10}$ for the poor capsule and $3.1 \times 10^{10}$ for the good capsule—the neutron burn history shows dramatic differences.

**Summary and Outlook**

A cryogenic-compatible neutron temporal diagnostic (cryoNTD) has been developed for OMEGA to allow the high-resolution measurement of the neutron burn history on early direct-drive $D_2$ cryogenic targets. The scintillator and the front end of the optical system are mounted in a TIM and inserted close to the target. The back end of the optical system containing the optical streak camera to record the light emitted from the scintillator is mounted outside the vacuum of the target chamber. The OMEGA fiducial system is used to cross-time the neutron signals to the incident laser pulse. This instrument is able to measure the neutron burn history at yields $>10^9$ DD neutrons with a resolution of ~80 ps. An absolute timing accuracy of 40 ps has been demonstrated using cross-calibration to the NTD. The time resolution of the cryoNTD is sufficient to resolve the important features of the reaction rate history of cryogenic implosions with high absolute timing accuracy. Future optimized cryogenic targets will generally show higher neutron yields,[3] allowing the use of a thinner scintillator (<0.5 mm), which will improve the time resolution of the instrument. Neutral density filters can be inserted in the light path to accommodate even the highest predicted yields, which will be comparable to $10^{12}$.

## ACKNOWLEDGMENT

This work was supported by the U.S. Department of Energy Office of Inertial Confinement Fusion under Cooperative Agreement No. DE-FC03-92SF19460, the University of Rochester, and the New York State Energy Research and Development Authority. The support of DOE does not constitute an endorsement by DOE of the views expressed in this article.

## REFERENCES

1. J. H. Nuckolls, Phys. Today **35**, 24 (1982).

2. S. Skupsky, R. Betti, T. J. B. Collins, V. N. Goncharov, D. R. Harding, R. L. McCrory, P. W. McKenty, D. D. Meyerhofer, and R. P. J. Town, in *Inertial Fusion Sciences and Applications 2001*, edited by K. Tanaka, D. D. Meyerhofer, and J. Meyer-ter-Vehn (Elsevier, Paris, 2002), pp. 240–245.

3. C. Stoeckl, C. Chiritescu, J. A. Delettrez, R. Epstein, V. Yu. Glebov, D. R. Harding, R. L. Keck, S. J. Loucks, L. D. Lund, R. L. McCrory, P. W. McKenty, F. J. Marshall, D. D. Meyerhofer, S. F. B. Morse, S. P. Regan, P. B. Radha, S. Roberts, T. C. Sangster, W. Seka, S. Skupsky, V. A. Smalyuk, C. Sorce, J. M. Soures, R. P. J. Town, J. A. Frenje, C. K. Li, R. D. Petrasso, F. H. Séguin, K. Fletcher, S. Padalino, C. Freeman, N. Izumi, R. Lerche, and T. W. Phillips, Phys. Plasmas **9**, 2195 (2002).

4. R. A. Lerche *et al.*, Rev. Sci. Instrum. **59**, 1697 (1988).

5. N. Miyanaga *et al.*, Rev. Sci. Instrum. **6**, 3592 (1990).

6. R. A. Lerche, M. D. Cable, and D. W. Phillion, Rev. Sci. Instrum. **61**, 3187 (1990).

7. T. J. Murphy and R. A. Lerche, *ICF Quarterly Report* **3**, 35, Lawrence Livermore National Laboratory, Livermore, CA, UCRL-LR-105821-93-1 (1992).

8. R. A. Lerche, D. W. Phillion, and G. L. Tietbohl, in *Ultrahigh- and High-Speed Photography, Videography, and Photonics '93*, edited by P. W. Roehrenbeck (SPIE, Bellingham, WA, 1993), Vol. 2002, pp. 153–161.

9. R. A. Lerche, D. W. Phillion, and G. L. Tietbohl, Rev. Sci. Instrum. **66**, 933 (1995).

10. D. D. Meyerhofer, J. A. Delettrez, R. Epstein, V. Yu. Glebov, V. N. Goncharov, R. L. Keck, R. L. McCrory, P. W. McKenty, F. J. Marshall, P. B. Radha, S. P. Regan, S. Roberts, W. Seka, S. Skupsky, V. A. Smalyuk, C. Sorce, C. Stoeckl, J. M. Soures, R. P. J. Town, B. Yaakobi, J. D. Zuegel, J. Frenje, C. K. Li, R. D. Petrasso, D. G. Hicks, F. H. Séguin, K. Fletcher, S. Padalino, M. R. Freeman, N. Izumi, R. Lerche, T. W. Phillips, and T. C. Sangster, Phys. Plasmas **8**, 2251 (2001).

11. Bicron Newbury, Newbury, OH 44065-9577.

12. R. A. Lerche, in *Ultrahigh- and High-Speed Photography, Videography, Photonics, and Velocimetry '90*, edited by P. A. Jaanimagi, B. T. Neyer, and L. L. Shaw (SPIE, Bellingham, WA, 1991), Vol. 1346, pp. 376–383.

13. W. R. Donaldson, R. Boni, R. L. Keck, and P. A. Jaanimagi, Rev. Sci. Instrum. **73**, 2606 (2002).

# Carbon Activation Diagnostic for Tertiary Neutron Measurements

## Introduction

In inertial confinement fusion (ICF)[1] implosions, nuclear reactions in the fusion fuel produce energetic neutrons and a variety of charged particles. The primary reaction for DT fuel is

$$\mathrm{D} + \mathrm{T} \rightarrow \alpha + \mathrm{n}\ (14.1\ \mathrm{MeV}). \tag{1}$$

In a secondary reaction, a small percentage of 14.1-MeV neutrons will scatter elastically from D or T ions in the fuel (prime notation indicates a scattered particle):

$$\mathrm{n} + \mathrm{D} \rightarrow \mathrm{n}' + \mathrm{D}'\ (0 - 12.5\ \mathrm{MeV}), \tag{2}$$

$$\mathrm{n} + \mathrm{T} \rightarrow \mathrm{n}' + \mathrm{T}'\ (0 - 10.6\ \mathrm{MeV}). \tag{3}$$

As these scattered ions pass through the fuel, some will undergo tertiary, in-flight fusion reactions:

$$\mathrm{D}'\ (0 - 12.5\ \mathrm{MeV}) + \mathrm{T} \rightarrow \alpha + \mathrm{n}''\ (12.0 - 30.1\ \mathrm{MeV}), \tag{4}$$

$$\mathrm{T}'\ (0 - 10.6\ \mathrm{MeV}) + \mathrm{D} \rightarrow \alpha + \mathrm{n}''\ (9.2 - 28.2\ \mathrm{MeV}). \tag{5}$$

The yield of these high-energy tertiary neutrons is proportional to $(\rho R)^2$ for small values of $\rho R$, where $\rho R$ is the areal density of the DT fuel, and to $\rho R$ for large values of $\rho R$ (Ref. 2) and is about $10^{-6}$ of the primary 14.1-MeV neutron yield.

The fuel areal density $\rho R$ is a fundamental parameter that characterizes the performance of an ICF implosion. For high areal densities ($\rho R > 0.3$ g/cm$^2$), which will be realized in implosion experiments at the National Ignition Facility (NIF) and Laser Megajoule Facility (LMJ), the target areal density exceeds the stopping range of charged particles, and $\rho R$ measurements with charged-particle spectroscopy will be difficult. In this region, an areal-density measurement using tertiary neutrons is one of the alternative methods. The use of tertiary neutrons for measurements of high areal densities in ICF implosions has been proposed by several authors[2–4] in the past. This article describes the experimental development of a tertiary neutron diagnostic using carbon activation and the 30-kJ, 60-beam OMEGA laser system.[5]

## Carbon as an Activation Material

The use of carbon as a threshold activation material was proposed many years ago.[3] There are three main reasons why carbon is a good activation material for tertiary neutron measurement. First, the $^{12}$C(n,2n)$^{11}$C reaction has a $Q$ value of 18.7 MeV, well above the 14.1-MeV primary DT neutron energy. Thus, the reaction $^{12}$C(n,2n)$^{11}$C will occur only from interactions with the high-energy tertiary neutrons. The experimental cross section of the $^{12}$C(n,2n)$^{11}$C reaction shown in Fig. 92.12 was measured in several experiments and can be used to calculate a tertiary neutron signal in a carbon sample.

The second attractive feature of carbon is the properties of its decay. The isotope $^{11}$C decays to $^{11}$B with a half-life of 20.39 min and emits a positron, resulting in the production of two back-to-back, 511-keV gamma rays upon annihilation. The $^{11}$C half-life is advantageous since it is compatible with the experimental conditions on OMEGA. The OMEGA laser fires at approximately one-hour intervals, and it takes a few minutes to remove the disk from the target chamber and carry it to the gamma-detection system after the laser has been fired. Thus, if the half-life were much shorter, a significant amount of information would be lost during transfer. If it were considerably longer, there would not be enough time to record all of the decays between shots. The positron decay of $^{11}$C is nearly identical to the $^{62}$Cu decay used in the copper activation measurements of 14.1-MeV primary DT yields; therefore, the well-developed copper activation gamma-counting system[6,7] can be used.

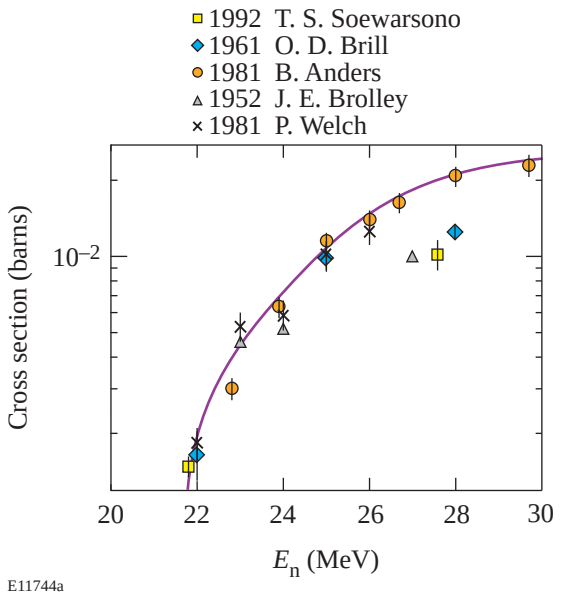


Figure 92.12
Experimentally measured cross section $\sigma$ for the reaction $^{12}C(n,2n)^{11}C$. The solid line is the fit used for calculations in the **Carbon Activation for OMEGA and the NIF** section.

The third reason carbon was chosen is the availability of high-purity samples. The purity of the activation sample is very important for tertiary activation diagnostic, as will be discussed in the **Contamination Signal in Carbon Activation** section below. Carbon is also a nontoxic, nonflammable, inexpensive, and safe material. These properties give carbon a big advantage over sodium, which has also been proposed.[3]

## OMEGA Carbon Activation System

The activation samples with a 7.6-cm diameter and a different thickness can be inserted with a pneumatic retractor into a reentrant tube installed on the OMEGA target chamber. Before a shot, the activation samples are manually installed in the retractor holder and inserted into the target chamber at 42 cm from the target. Immediately after a laser shot, the activated sample is automatically extracted from the chamber and dropped through a plastic tube to the pickup basket in a room under the OMEGA Target Bay. The operator delivers the activated sample to the gamma-detection system in the counting room. Generally, this process takes 1.5 to 3 min. Since the space in the OMEGA target chamber is very limited, the same pneumatic retractor is used for both copper and carbon activation diagnostics.

The OMEGA gamma-detection system consists of two 7.6-cm-diam, 7.6-cm-thick NaI(Tl) scintillation detectors separated by 0.89 cm or 1.78 cm and associated electronics. Each detector has an ORTEC 460 delay linear amplifier and an ORTEC 551 single-channel analyzer (SCA), which perform pulse-height discrimination. The time coincidence between two detectors is established by an ORTEC 418A universal coincidence module followed by an ORTEC 974 quad counter/timer module that counts time, single counts from each detector and two detectors coincidence. The 974 counter is read by a PC-based data acquisition program every 5 s and recorded for future analysis. The window of each SCA is set between 426 keV and 596 keV in order to detect 511-keV gammas from positron annihilation. The energy scale of each SCA is calibrated with a $^{22}Na$ radioactive source before each set of measurements. The NaI detectors are shielded from all sides with 7.6 cm of lead to reduce cosmic ray background. As a result of the shielding, the background coincidence count rate is about 18 counts/hour. To isolate the NaI detectors from direct activation by 14.1-MeV neutrons produced during high-yield OMEGA shots, the gamma-detection system is placed at a distance of 120 m from the target. Dedicated experiments have shown that the gamma-detection system records no coincidence for yields up to $7 \times 10^{13}$.

## Contamination Signal in Carbon Activation

Any material that produces a positron emitter by interaction with 14.1-MeV neutrons will add a contamination signal in the carbon activation diagnostic. The most-dangerous contaminants for carbon activation are copper and nitrogen, which produce positron emitters in reactions $^{63}Cu(n,2n)^{62}Cu$, $^{65}Cu(n,2n)^{64}Cu$, and $^{14}N(n,2n)^{13}N$. Each of these reactions has a threshold below 14 MeV. The nitrogen cross section for a 14.1-MeV neutron is 6.5 mb and is comparable to the carbon cross section for tertiary neutrons. The $^{63}Cu$ cross section for 14.1-MeV neutrons is about 100 times larger than the carbon cross section for tertiary neutrons. Since the primary 14.1-MeV neutron yield is about $10^6$ times larger than the tertiary yield, the contamination in the carbon sample must be less than one part per million (ppm) for nitrogen and 0.01 ppm for copper.

In the development of the carbon activation diagnostic, graphite disks from Bay Carbon[8] were used. Bay Carbon carefully selects their graphite for its physical and chemical compositions and performs chemical vapor purification (CVP) of the graphite. Bay Carbon purity is defined as follows: No more than three elements may be present (other than carbon), no single element may exceed one part per million

(ppm), and the total impurity level may not exceed two ppm in the graphite.

In addition to the purity of the sample material itself, proper packaging and handling procedures are very important. To keep the graphite disks clean before a shot, the disks are shrink-wrapped in plastic before being placed into the retractor and delivered to the gamma-detection system. The plastic is removed and discarded before counting. This procedure prevents surface contamination of the graphite disks. This is especially important on OMEGA because the same retractor is used for both copper and carbon activation. The graphite disks without shrink wrap showed a contamination signal of about 1000 coincidences per hour of counting. The shrink-wrapping procedure protects the graphite disks from surface contamination but leads to other forms of contamination.

The shrink-wrap plastic contains hydrogen. When bombarded by 14.1-MeV neutrons, the hydrogen atoms can produce elastically scattered protons with energies up to 14 MeV. These protons interact with carbon in the graphite disks and produce positron-emitting nitrogen via reaction $^{12}C(p,\gamma)^{13}N$. This source of contamination was eliminated through the use of graphite foils (thinner pieces of graphite) placed on both sides of the disk between the disk and the shrink wrap. The graphite foils act as protective barriers for the protons from the plastic. This combination of the disk and two foils is called a "sandwich." The foils are made from the same graphite as the disks in order to keep the disks clean. The foils are 2.5 mm thick, enough to completely stop the protons originating in the plastic and prevent their penetrating the graphite disk. All contamination from such protons is restricted to the graphite foils, which are removed and discarded before counting.

Because the graphite porosity is about 20%, the graphite disks can absorb and store $^{14}N$ nitrogen from the air. The 14.1-MeV neutrons can produce positron-emitting nitrogen $^{13}N$ via the reaction $^{14}N(n,2n)^{13}N$. To remove air from the graphite disks, a special purification facility was developed at the SUNY Geneseo.

The first step in the purification process is to remove the nitrogen and other contaminant gases from within the graphite disks and replace them with an inert gas such as argon that cannot be activated by 14.1-MeV neutrons. To do this, a large three-zone tube furnace is employed. This furnace is composed of a 7-ft-long, 7-in.-diam quartz tube. The graphite disks are inserted into the oven using a 5-ft-long rod. The oven is then brought to vacuum, heated to 1000°C, and maintained at that temperature for several hours. After cooling to room temperature, the quartz tube is flooded with high-purity (0.99995) argon. The disks stay in this environment for several hours. They are extracted from the quartz tube by placing a large glove bag over one end of the tube, filling it to positive pressure with argon gas, and then using a rod to remove the disks from the quartz tube into the glove bag. Graphite foils are fit to both sides of the disk, and the disks are then placed into small vacuum bags, which are immediately vacuum sealed. The disks can remain in the vacuum-sealed bag for at least six months without contamination.

In earlier experiments, the disks were taken out of the vacuum bags immediately before the shot and quickly sealed in shrink wrap, which was left on during the shot. In later experiments, the disks were shot in the vacuum bags, never being exposed to air contaminants.

**Experimental Results**

The main goal of the diagnostic development was to minimize the contamination signal in carbon samples. Several iterations of the purification, packaging, and gamma-detection system were made until the system described above was developed. In this section, results obtained in 2001–2002, after major improvements to the system, are presented.

Tests of the carbon activation system were carried out on the 30-kJ, 60-beam OMEGA laser system[5] in direct-drive implosions. A 1-ns square laser pulse shape with 28-kJ to 31-kJ energy was used to implode glass microballoons with shell thicknesses from 2.5 to 4 $\mu$m filled with 20 atm of DT. These targets have a very low $\rho R$ and should produce no measurable tertiary neutrons. Thus, any signal in these experiments was a contamination signal. The primary DT neutron yield was measured by an absolutely calibrated time-of-flight scintillating counter located 20 m from the target. The neutron yields in these experiments ranged from $4 \times 10^{13}$ to $9.6 \times 10^{13}$.

In the experiments on OMEGA, the cosmic ray background for the empty gamma-detection system was measured, fitted to a linear function, and subtracted from the coincident counts for each carbon disk. The results from the graphite disks were then normalized to a yield of $7.4 \times 10^{13}$, which was the average neutron yield for this series of measurements. The carbon disks without shrink wrap produced a contamination signal of about 1000 counts; disks in shrink wrap produce about 80 to 100 counts; and disks packaged as a sandwich in shrink wrap produce a contamination signal of only about 30 to 50 counts. The results for the carbon disks irradiated in sealed vacuum bags

are shown in Fig. 92.13. The two shots with carbon disks in vacuum bags without foils show a higher contamination signal than from a sandwich, demonstrating the importance of shielding from the protons originating in the plastic. The six sandwich results include four shots from June 2001 and two "consistency check" shots from June 2002. All of them show a similar contamination signal of 30 to 50 coincidence counts for $7.4 \times 10^{13}$ primary neutron yield.

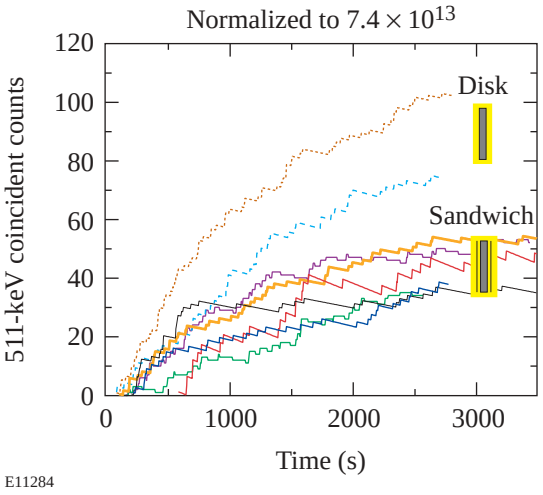


Figure 92.13
Coincidence counts in the gamma-detection system as a function of time after a shot for 0.89-cm-thick disks and "sandwiches."

The 0.89-cm carbon disk thickness originates from a copper disk thickness optimized for 511-keV gamma absorption in copper. Since the absorption length of 511-keV gammas in carbon is about five times larger than in copper, the carbon disk thickness can be increased. In June 2002 we tested on OMEGA carbon disks with a thickness of 1.78 cm. The results of these tests normalized to the same $7.4 \times 10^{13}$ primary neutron yield are shown in Fig. 92.14. The contamination signals from the thicker disks are similar to the thinner disks, suggesting that contamination is mostly a surface-related effect. In the thicker disks the tertiary signal will increase by a factor of 2, and the efficiency of the gamma-detection system decreases for the thicker disk by approximately 20%; the thicker disk has a 1.8 gain in sensitivity. Monte Carlo calculations for the optimal carbon disk thickness are in progress.

Consistent, repeatable results in two sets of measurements one year apart, which include the manufacture of new carbon disks, show stability and reproducibility of the carbon activation diagnostic chain—from manufacturing the disk to the purification and handling system.

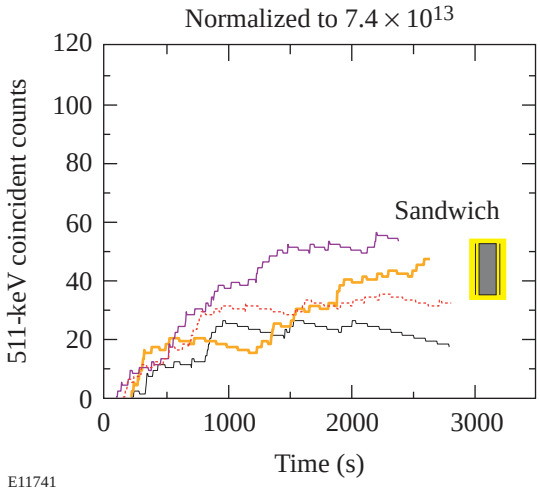


Figure 92.14
Coincidence counts in the gamma-detection system as a function of time after a shot for 1.78-cm-thick sandwiches.

## Carbon Activation for OMEGA and the NIF

Direct-drive spherical DD cryogenic target implosions[9] are routinely carried out on the 60-beam OMEGA laser system, and implosions with cryogenic DT fuel are planned for the near future. The OMEGA cryogenic DT design and expected laser pulse shape with an intensity picket are shown in Fig. 92.15. The intensity picket shapes the adiabat of the main fuel and ablator, reducing both the seeds and the growth rate of Rayleigh–Taylor instability.[10] A one-dimensional *LILAC*[11] simulation calculates a neutron yield of $Y_n = 6.0 \times 10^{14}$ and a neutron-averaged fuel areal density $\langle \rho R \rangle = 245$ mg/cm$^2$ for the design shown in Fig. 92.15. The *IRIS*[12] postprocessor to *LILAC* was used to calculate the spectrum of all neutrons emerging from an OMEGA cryogenic DT target. Figure 92.16 shows the calculated tertiary/primary neutron spectrum and the same spectrum multiplied by the cross section of the $^{12}C(n,2n)^{11}C$ reaction approximated by the solid line in Fig. 92.12.

The target design from Fig. 92.15 and tertiary spectrum from Fig. 92.16 were used to estimate the expected signal from a carbon activation sample in OMEGA cryogenic DT experiments. A 7.6-cm-diam, 0.89-cm-thick carbon disk at 40 cm from the target subtends solid angle $2.25 \times 10^{-3}$. The integral of the tertiary/primary neutron spectrum multiplied by the carbon cross section in Fig. 92.16 is about $3 \times 10^{-5}$ mb/primary neutron. The 80-g carbon disk will receive $1.2 \times 10^{-7}$ activations for each incident primary neutron or $2.7 \times 10^{-10}$ activations for each primary neutron produced in the

target. The gamma-detection system has an efficiency of 20%, thus the measured coincidence counts per produced primary neutron will be $5.4 \times 10^{-11}$. At a primary DT yield $Y_n = 6.0 \times 10^{14}$, we expect $3.2 \times 10^4$ coincidence counts from tertiary neutrons in the gamma-detection system. A similar calculation for the implosion quenched at a $\langle \rho R \rangle$ = 150 mg/cm$^2$ and neutron yield $Y_n = 9.2 \times 10^{13}$ gives about 400 coincidence counts in the gamma-detection system. With the achieved level of contamination signal, the present carbon activation system can be used for areal-density measurements of OMEGA cryogenic DT targets.

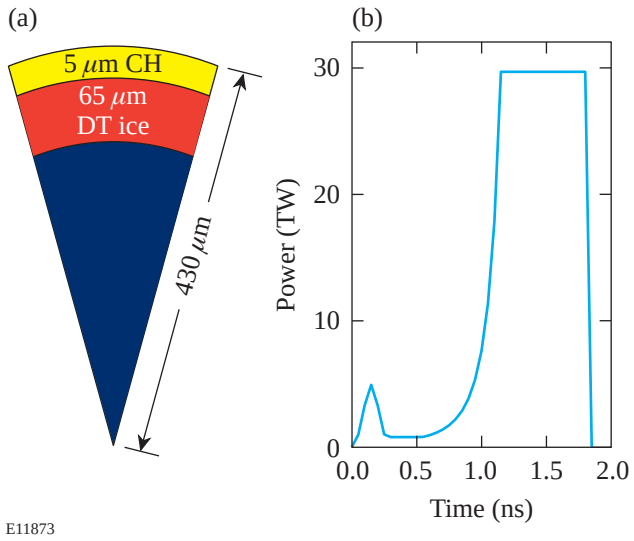


Figure 92.15
The OMEGA cryogenic capsule design (a) and pulse shape with an intensity picket (b).

Tertiary neutron measurements by carbon activation are an inexpensive, well-developed diagnostic that can be easily deployed on the NIF for areal-density measurements. All major diagnostic development problems have already been solved on OMEGA. Purified carbon packages are good for at least six months; consequently, they can be prepared in the already-existing purification facility at SUNY Geneseo and shipped to the NIF as needed. The carbon activation diagnostic will require a rapid transport system similar or identical to the yield activation system on the NIF because of the relatively short half-life of carbon.

The only problem that must be solved on the NIF for carbon activation is background in the gamma-detection system itself generated by the neutrons from a NIF implosion. Such a background-induced problem was observed on OMEGA when the gamma-detection system was located 40 m from the target. In Fig. 92.17 the background coincidence counts of an empty gamma-detection system are shown as a function of time. After a shot with a neutron yield of $7.35 \times 10^{13}$, a jump of 42 coincidence counts was recorded. Additionally the background stays high for about 1 h after the shot and then returns to the normal cosmic ray level. On OMEGA this background prob-

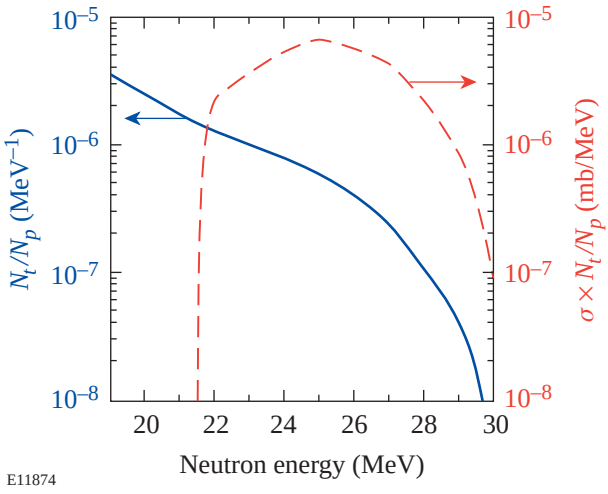


Figure 92.16
Ratio of tertiary $N_t$ to the primary $N_p$ neutrons per energy interval (MeV) as a function of tertiary neutron energy and the same ratio multiplied by the carbon cross section $\sigma$ in mb.

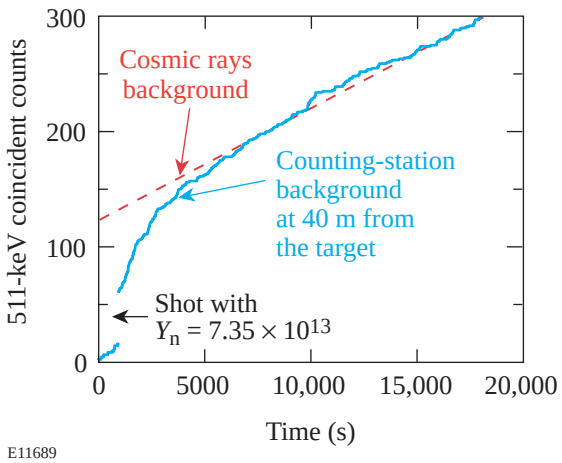


Figure 92.17
Background coincidence counts of an empty gamma-detection system at 40 m from the target during an OMEGA shot with a neutron yield of $7.35 \times 10^{13}$.

lem was solved by moving the gamma-detection system much farther from the target. Since neutron yield on the NIF will be about $10^5$ times higher than on OMEGA, a judicious choice of neutron shielding and location of the gamma-detection system will be required. Background measurements during the shot will also be needed. Two identical gamma-detection systems could be implemented—one for signal and another for the background measurement.

## Conclusions

This article has described the experimental development of the carbon activation diagnostic for tertiary neutron measurements performed on the 60-beam OMEGA laser system. We have created a purification facility and have developed packaging and handling procedures that significantly reduce the contamination signal in the carbon samples. Experiments on OMEGA in 2001–2002 have shown very good reproducibility of the contamination signal from the carbon samples.

The present carbon activation system is ready for areal-density measurements of DT cryogenic targets on OMEGA. The same carbon activation diagnostic can be implemented on the NIF, although the neutron-induced background issues in the gamma-detection system need to be solved for the NIF.

## ACKNOWLEDGMENT

This work was supported by the U.S. Department of Energy Office of Inertial Confinement Fusion under Cooperative Agreement No. DE-FC03-92SF19460, the University of Rochester, and the New York State Energy Research and Development Authority. The support of DOE does not constitute an endorsement by DOE of the views expressed in this article.

## REFERENCES

1. J. D. Lindl, *Inertial Confinement Fusion: The Quest for Ignition and Energy Gain Using Indirect Drive* (Springer-Verlag, New York, 1998).
2. Laboratory for Laser Energetics LLE Review **69**, 46, NTIS document No. DOE/SF/19460-152 (1996). Copies may be obtained from the National Technical Information Service, Springfield, VA 22161.
3. D. R. Welch, H. Kislev, and G. H. Miley, Rev. Sci. Instrum. **59**, 610 (1988).
4. H. Azechi, M. D. Cable, and R. O. Stapf, Laser Part. Beams **9**, 119 (1991).
5. T. R. Boehly, D. L. Brown, R. S. Craxton, R. L. Keck, J. P. Knauer, J. H. Kelly, T. J. Kessler, S. A. Kumpan, S. J. Loucks, S. A. Letzring, F. J. Marshall, R. L. McCrory, S. F. B. Morse, W. Seka, J. M. Soures, and C. P. Verdon, Opt. Commun. **133**, 495 (1997).
6. F. C. Young, J. Golden, and C. A. Kapetanakos, Rev. Sci. Instrum. **48**, 432 (1977).
7. R. J. Leeper *et al.*, Nucl. Instrum. Methods Phys. Res. B **B24**, 695 (1987).
8. Bay Carbon Inc., Bay City, MI 48706.
9. C. Stoeckl, C. Chiritescu, J. A. Delettrez, R. Epstein, V. Yu. Glebov, D. R. Harding, R. L. Keck, S. J. Loucks, L. D. Lund, R. L. McCrory, P. W. McKenty, F. J. Marshall, D. D. Meyerhofer, S. F. B. Morse, S. P. Regan, P. B. Radha, S. Roberts, T. C. Sangster, W. Seka, S. Skupsky, V. A. Smalyuk, C. Sorce, J. M. Soures, R. P. J. Town, J. A. Frenje, C. K. Li, R. D. Petrasso, F. H. Séguin, K. Fletcher, S. Padalino, C. Freeman, N. Izumi, R. Lerche, and T. W. Phillips, Phys. Plasmas **9**, 2195 (2002).
10. V. N. Goncharov, "Improved-Performance of Direct-Drive ICF Target Designs with Adiabat Shaping Using and Intensity Picket," presented at the 44th Annual Meeting of the APS Division of Plasma Physics, Orlando, FL, 11–15 November 2002; to be published in Physics of Plasmas.
11. M. C. Richardson, P. W. McKenty, F. J. Marshall, C. P. Verdon, J. M. Soures, R. L. McCrory, O. Barnouin, R. S. Craxton, J. Delettrez, R. L. Hutchison, P. A. Jaanimagi, R. Keck, T. Kessler, H. Kim, S. A. Letzring, D. M. Roback, W. Seka, S. Skupsky, B. Yaakobi, S. M. Lane, and S. Prussin, in *Laser Interaction and Related Plasma Phenomena*, edited by H. Hora and G. H. Miley (Plenum Publishing, New York, 1986), Vol. 7, pp. 421–448.
12. Laboratory for Laser Energetics LLE Review **86**, 68, NTIS document No. DOE/SF/19460-393 (2001). Copies may be obtained from the National Technical Information Service, Springfield, VA 22161.

# The Properties of Polyimide Targets

In 1996 LLE began a research effort to make spherical capsules from polyimide material for use in direct-drive inertial confinement fusion (ICF) experiments. Previously, ICF capsules were made exclusively from glass, polystyrene, or an amorphous carbon–hydrogen solid solution referred to as "plasma polymer" or "glow-discharge polymer."[1] Polyimide was first proposed as a potential material for a target wall in 1995 because of its appreciable strength;[2] however, no viable method for making these capsules was identified. Following a five-year development project, a process for making polyimide capsules was developed and demonstrated, and the technology transferred to General Atomics—the ICF target fabricator—for production. As part of the project, polyimide shells with various properties relevant to ICF were developed. Those properties will be presented and compared in this article.

The fabrication method and associated properties of the different direct-drive polyimide targets have been reported previously.[3–5] This article summarizes and compares those properties that are important for producing cryogenic targets. Furthermore, issues that are unique to providing cryogenic targets, which impose stringent demands on performance from the shell material, are explained.

The properties of polyimide of importance to direct-drive ICF experiments are those that will increase the survivability of the shell during the process used to make cryogenic deuterium–tritium targets: specifically, the mechanical and permeation properties and the resistance of the material to embrittlement in a radioactive (tritium) environment. The rationale for choosing polyimide as a candidate material is that the polyimide chemical structure is one of the strongest polymeric materials, and among the most radiation resistant polymers,[6] and it should have the greatest likelihood of surviving demanding processing conditions.

Shells used for direct-drive ICF experiments need to be as robust as possible to withstand the inherent pressure gradients present when equipment has to operate over a wide pressure and temperature range. Shells are typically ~900 to 950 $\mu$m in diameter with the wall as thin as possible (1 to 3 $\mu$m) to minimize Raleigh–Taylor (RT) instabilities. The shell becomes an ICF target when it contains a nominal 100-$\mu$m layer of deuterium ice, which will include tritium in future experiments. The ice layer is achieved by first permeating gas at room temperature (or greater) into the shell and then cooling the shell and gas to below the triple point (for deuterium) at 18.73 K. The challenge in this process is caused by the fragility of the shell, which because of its large aspect ratio (diameter to wall thickness) can withstand only a very small pressure differential. This limits the driving force for permeation: it can take many days to fill the capsule with the sizeable gas inventory required to yield a 100-$\mu$m ice layer, and a well-controlled thermal environment is required to prevent the target from bursting or buckling.

During the permeation filling cycle, which can occur at temperatures from 270 to 500 K, and the subsequent cooling process to 18 K, the radioactive tritium gas decays with a half-life of 12.3 years and releases an electron with a mean energy of 6 keV. These high-energy electrons rupture chemical bonds, thereby weakening the capsule material. This creates a self-limiting cycle where increasingly long filling/cooling times de-rate the capsule's strength, which in turn requires even longer filling/cooling times. It has yet to be established that high-aspect-ratio shells can even be filled with tritium to the desired pressure without rupturing.

Finally, there is a requirement to minimize the processing time (filling and cooling cryogenic targets) as tritium decay produces a helium atom that will affect the convergence, and hence performance, of an imploding target. Given the tritium decay rate (0.015% conversion of T to $^3$He per day), the desired duration for filling and cooling cryogenic targets is less than three days.

The sections that follow discuss (1) the mechanical properties of polyimide shells; (2) the techniques for changing the

shell's permeability by controlling the composition and microstructure of the polyimide; (3) the cooling of targets; and (4) the effects of radiation on shell properties.

### The Structural Behavior and Properties of Polyimide Shells

1. The Mechanics of a Shell's Response to a Pressure Differential

A pressure differential across a shell's wall generates a uniform hydrostatic load within the wall that is resisted by in-plane forces (tension, compression, and shear) (see Fig. 92.18).[7] The magnitude of the induced forces can be analyzed solely by force-equilibrium equations (membrane theory) as long as the shell does not deform under the applied load, i.e., it is statically determined. Once the shell deforms, bending theory is needed to fully quantify the stress distribution in the shell and hence determine the maximum pressure differential a shell can withstand.

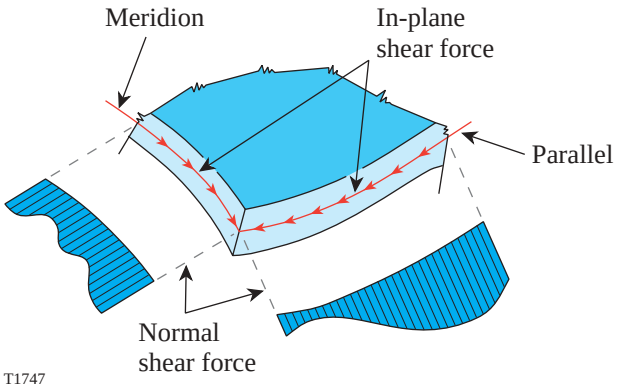


Figure 92.18
Schematic of the in-plane membrane forces present in a uniformly strained shell.

Direct-drive shells are classified as thin-walled shells; shells where the ratio of the wall thickness to the shell radius is less than 0.05 are categorized as "thin wall" and shells where the ratio is greater than 0.05 are "thick wall." This category of shell is unable to resist even small out-of-plane bending moments that easily deflect the wall. Once the shell is deformed, the intrinsic strength of the spherical geometry is compromised and the shell either shatters if it is brittle or collapses intact if it is elastic. Thicker-wall shells, such as indirect-drive shells, have a twofold strength advantage over thin-wall shells: first, the load-bearing capacity of the shell is greater, and second, once a shell begins to deflect to out-of-plane moments, the wall more effectively resists the bending moment. Calculating the strength of thick-wall shells is also more complex since the bending theory is now an effective secondary reinforcement mechanism (membrane theory describes the primary mechanism) for resisting the applied load.

The buckle pressure is defined as that uniform load where the shell wall is at its maximum in-plane compression and shear stress, and any infinitesimal increase in pressure will cause the shell wall to deform. Increasing the pressure subjects the shell wall to bending moments, and at a critical pressure—the collapsing pressure—the shell collapses. The shells of interest in direct-drive ICF are all thin-wall (<5-$\mu$m) polymers with little resistance to out-of-plane forces, so the collapsing pressure is equal to the buckling pressure. The buckling pressure $P_{\text{buckle}}$ is determined by the dimensions of the shell and the intrinsic properties of the material:[7]

$$P_{\text{buckle}} = \frac{2E}{\sqrt{3\left(1-\nu^2\right)}}\left(\frac{w}{r}\right)^2, \tag{1}$$

where $E$ is the elastic modulus, $\sigma$ is the tensile strength, $\nu$ is Poisson's ratio (0.34), $w$ is the wall thickness, and $r$ is the radius.

The bursting pressure $P_{\text{burst}}$ is analogous to the buckling pressure except that the internal pressure is greater than the external pressure and the in-plane forces are tensile ($\sigma$) and shear:

$$P_{\text{burst}} = 2\sigma\left(w/r\right). \tag{2}$$

ICF targets are not perfectly spherical, although the sphericity is excellent (0.5±0.2 $\mu$m out-of-round). This lack of sphericity decreases the buckling pressure from what would be expected for a perfectly spherical shell: At the region where the shell departs from perfect sphericity, the radius of curvature changes. Here the in-plane compressive stress acquires a shear component. This stress deflects the shell wall out-of-plane; the magnitude of the deflection and the affected area of the shell depend on the shear and flexural moduli, respectively. Thin-wall shells have little resistance to this out-of-plane force, so once the applied in-plane load can no longer be supported by in-plane compression, the strength of the spherical shape is compromised and the shell buckles. Shells where the radius of curvature changes abruptly, and that also have low shear and flexural moduli, will buckle at lower loads than rounder shells with greater stiffness.

Two phenomena combine to make thinner shells substantially more fragile: First, thinner-wall shells are more out-of-round than moderately thicker shell walls, a consequence of the shell fabrication process; second, as discussed above, thinner walls are inherently less resistant to bending moments than are moderately thicker shell walls. Experimentally it was observed that as the thickness of the shell wall decreases below 4 $\mu$m, the elastic modulus [Eq. (1)] becomes a weaker predictor of the maximum buckling pressure that a shell can withstand: There is a greater variation in the observed buckle pressure of a large sample of very thin wall shells (1 $\mu$m) compared to thicker shells. This behavior is not adequately explained by possible variations in the elastic modulus and Poisson ratios of different shells, which are intrinsic material properties independent of thickness; these properties depend upon the materials' microstructure, and supporting x-ray diffraction data show a similar microstructure for thick and thin films.[8,9] A more probable explanation for the greater variation in the buckle pressure of thin-wall shells is a greater variation in the roundness of the shells.

In the future, each shell will have to meet a specification for the maximum-allowable out-of-roundness to maximize the shell's survivability during processing. This will require the sphericity and uniformity of the wall thickness of each thin-wall shell to be quantified.

2. Fabrication of Thin-Wall Spherical Shells

Two effects can reduce the sphericity of the shell: First, there is the inherent out-of-roundness of the mandrel on which the polyimide shell is formed. Typically this value increases as the mandrel diameter increases. Second, a consequence of the polyimide-shell manufacturing is that additional out-of-roundness can be introduced during fabrication. Typically, this contribution is greater for thinner shell walls.[9]

The fabrication technique is summarized in Figs. 92.19 and 92.20. First, polyamic acid is deposited on a mandrel. The coated mandrel is then heated to convert polyamic acid into polyimide and simultaneously depolymerize the poly-$\alpha$ methyl-styrene mandrel. This depolymerization of the 30-$\mu$g mandrel would generate a burst pressure of 140 atm in the absence of permeation. Permeation does occur, however, and if the depolymerization rate is kept at or below the permeation rate, the polyimide shell will inflate only marginally and without exploding. Shells with walls as thin as 0.9 $\mu$m have been fabricated in this manner.[5,9] Shells can be made more out-of-round (beyond the limit established by the mandrel) during the depolymerization phase where expansion of the shell stresses the plastic: If the shell material is strained beyond the yield point, it will plastically deform in those areas where the wall is thinnest. This nonuniform and nonrecoverable expansion will cause the shell to lose its sphericity when the internal pressure is reduced.[9]

While it is possible to make polyimide shells with the desirable strength and modulus properties, strict quality control will be required to select only the best geometries. Otherwise the greater mechanical properties of polyimide will not be realized.

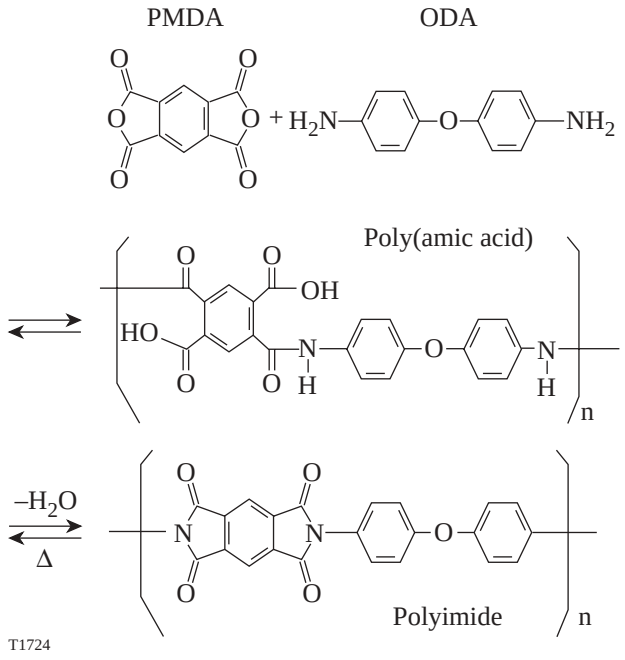


Figure 92.19
Schematic of the chemical process used to make polyimide shells using the vapor-deposition technique.

3. Stiffness, Strength, and Elasticity of Polyimide Shells

The physical properties of polyimide shells are listed in Table 92.I; the properties of plasma polymer shells are also listed for comparison. Generally, polyimide has greater physical properties than plasma polymer and, in addition, has a higher density, radiation resistance, and lower permeability, so the selection of one of these materials over the other as the optimal shell material is not immediately apparent. The implications of these other properties (permeability and radiation resistance) on the selection of polyimide or plasma polymer as a target material are expanded upon later.

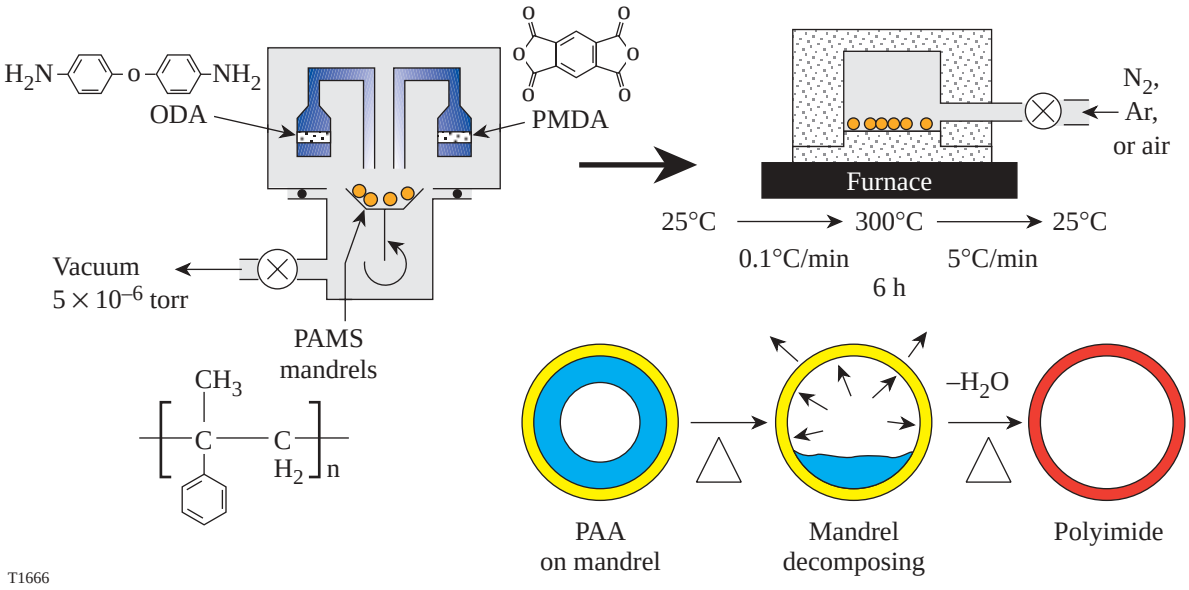


Figure 92.20
Sequence of operations used to make polyimide shells.

The elastic modulus of vapor-deposited polyimide shells [calculated from Eq. (1)] was marginally larger than the literature-reported values for the same chemical formulation made using liquid processing: 3.2 GPa and 3.0 GPa, respectively.[10,11] There is a difference, however, in the method used to measure these values: using overpressure to buckle shells measures a biaxial compressive elastic modulus, whereas literature values for a commercial polyimide, Kapton™, are measured using American Standards and Testing Materials (ASTM) procedures with uniaxial tensile loading. The elastic modulus for vapor-deposited polyimide was also measured using an accepted nano-indentation method and was determined to be 4.0 GPa.[9]

The tensile strength of the polyimide was calculated from Eq. (2) by changing the pressure on either side of the shell and measuring the commensurate change in the diameter of the shell.[9,10] Vapor-deposited polyimide shells are appreciably stronger than solution-cast films, with ultimate strengths of 280±20 MPa and 170 MPa, respectively. The greater strength of the vapor-deposited polyimide material is attributed to the preferential alignment of the crystalline lattice in polyimide shells (discussed in detail later). Similar to the elastic-modulus measurements, pressure testing a shell to determine the tensile strength is a measure of the biaxial tensile stress–strain behavior (in the plane of the shell), which is different from a uniaxial strength test of an ASTM-dimensioned measurement.

It is important to note that all testing of both polyimide and plasma polymer shells was to determine the optimal processing conditions as measured by each material's inherent stiffness, strength, and plasticity. No effort was intentionally made to preselect an underlying mandrel within a particular roundness and wall thickness specification. (This would have made the study too large, expensive, and intractable.) Therefore, the variation in the mandrels' sphericity is included in the statistical variation of the polyimide shells. This has the biggest effect on the reported elastic-modulus values of the shells, which are most susceptible to out-of-roundness effects. The possibility remains that future optimization and strict quality control of the underlying mandrels will improve the mechanical properties of both polyimide and plasma polymer shells.

The importance in ICF applications of having a higher-strength shell material is to improve the ability of the shell to (1) resist buckling pressures during permeation filling, (2) resist bursting and buckling pressures that develop within the permeation cell when a filled target is cooled to 20 K, and (3) resist bursting when the target is transferred (inside a cryostat) from the permeation cell to a cryostat.[12] This requires

Table 92.I: Comparison of the physical properties and chemical composition of available ICF shell materials.

| Polymer Material | Elastic Modulus (GPa) | Ultimate Strength (MPa) | Elongation (%) | Chemical Composition | |
|---|---|---|---|---|---|
| | | | | Atomic fraction (%) | |
| Polyimide (PMDA-ODA formulation) 1.42 gm/cm$^3$ | 3.2±0.1 | 280±12 | 27±2 | C<br>H<br>N | 56<br>26<br>5 |
| Polyimide (6FDA-ODA formulations) 1.42 gm/cm$^3$ | 2.6±0.1 | 221±15 | 15±2 | C<br>H<br>N<br>O<br>F | 54<br>24<br>3<br>9<br>13 |
| Plasma polymer[13] (high-density/ strength version) 1.18 gm/cm$^3$ | 2.7±0.2 | 88±10 | | C<br>H | 54<br>46 |
| Plasma polymer[13] (baseline) 1.04 gm/cm$^3$ | 1.6±0.4 | 80±5 | | C<br>H | 43<br>57 |
| Deuterated plasma polymer[13] (high-strength/ density version) 1.11 gm/cm$^3$ | 2.0±0.1 | 82±5 | | C<br>D | 61<br>39 |
| Deuterated plasma polymer[13] 1.09 gm/cm$^3$ | 0.9±0.2 | | | C<br>D | 59<br>41 |

that the elastic modulus and strength of the shell material be known over a wide temperature range (at least from 295 K to 18 K and more desirably from 573 K to 18 K to allow for higher-speed permeation at elevated temperatures). Typically, the room-temperature strength of the material is the most commonly reported value. The measured temperature dependences of the strength and elastic modulus are reported in Fig. 92.21. The elastic modulus is measured to increase by a factor of 2.5 over the temperature range 300 K to 130 K.

Polymers become stronger at lower temperatures, which increases the survivability of polymers in cryogenic applications. In ICF applications, however, use of only this value can be deceptive, since a plastically strained shell may have too high a permeability, which renders it useless, so the yield strength, below which a material behaves elastically, must also be known. Once a shell exceeds the yield strength, the change in the diameter in response to the applied stress is determined by the coefficient of hardening (the slope of the stress–strain curve in the plastic regime). This value is typically much smaller than the elastic modulus. A small stress in this regime can create a sizeable strain that will cause the shell to expand significantly and not recover its original dimensions. Moreover, the shell can deform (i.e., change in roundness) if the walls are not uniformly thick. By reason of this behavior the stress–strain relationship of the polyimide ideally should be known over the entire temperature range of interest (18 K to 573 K). This will allow the cryogenic target handling equipment to be designed to minimize the time required to provide ICF cryogenic targets (to limit the buildup of $He^3$). Obviously, equipment to handle cryogenic targets can be designed without detailed knowledge of the shell's behavior, but the design will

necessarily be conservative to ensure that the target survives processing, which is counter to the need to process targets as rapidly as possible.

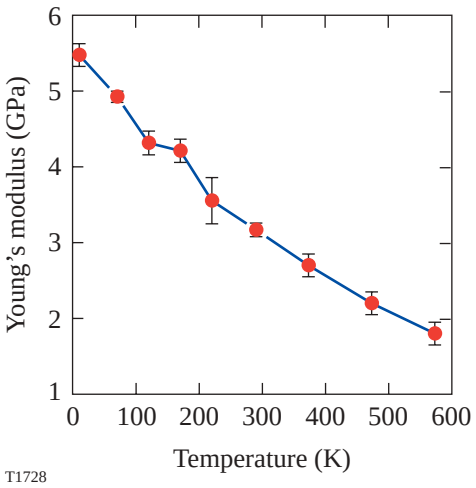


Figure 92.21
The temperature-dependent elastic modulus of polyimide from 12 K to 573 K.

4. Effects of Plastically Deforming Polyimide Shells

X-ray diffraction data of polyimide shells indicate the presence of a crystalline phase.[8] The crystal lattice plane is aligned perpendicular to the circumference of the shell as the polymer chain preferentially lies in the plane of the shell (see Fig. 92.22). This configuration gives the polyimide shell its strength and stiffness in compression/buckling, due to the stiffness of the lattice structure to out-of-plane forces, and also in tension/bursting, due to the alignment of the polymer backbone within the plane of the circumference.

When a polyimide shell is over-tensioned, as occurs when the internal pressure in the shell exceeds the yield stress of the material, the polyimide plastically deforms and the mechanical properties of the shell decrease: the buckle pressure decreases by 55%, which is attributed to the elastic modulus decreasing as the crystallinity of the material decreases,[9,10] and the shell becomes more nonspherical, which lowers the in-plane compressive and shear loads that the shell can withstand.

Of particular interest and relevance to ICF applications is the effect that plastically deforming polyimide has on the permeability of the material. A large sample of 120 polyimide shells were over-pressurized to determine the effect of strain on the permeability of the material to deuterium. The effect fell into one of two categories: the permeability changed either enormously (three orders of magnitude) or only slightly (from no change to a quadrupling). The biggest change occurred in 30% of the shells. Importantly, the gas transport mechanism remained permeation, where the gas must dissolve in the plastic material, since heating the capsule to 300°C completely recovered the initial permeation and strength/modulus properties. The alternative gas transport mechanism is Knudsen diffusion, which would occur if pinholes or voids were created. These features would allow a gas/gas-surface diffusion process where gas can pass through a membrane without being absorbed into the material. This would be unacceptable since the shell would remain permeable at cryogenic temperatures, allowing the low-viscosity gas and liquid to easily pass out of the shell; as a result, the target would be unable to retain the deuterium fill.

When polymers are cooled, the activation energy for permeation increases and the permeability of the material decreases (more detail later in this article); however, an internal overpressure within the shell strains the wall and counteracts the decrease in permeability. This phenomenon was observed in 0.9-mm-diam plasma polymer shells filled with liquid deuterium (~51 $\mu$g) at 20 K (which equates to 1000-atm pressure at room temperature). When the shell was allowed to warm gradually, the internal pressure increased and the gas permeated out of the shell. Following this observation, the perme-

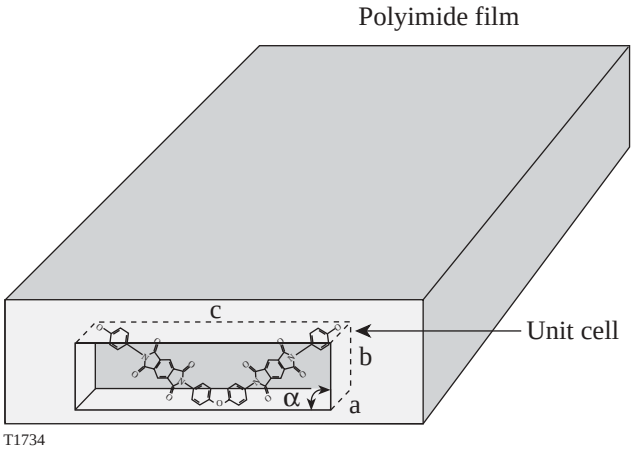


Figure 92.22
Schematic of the orientation of a polyimide crystal unit cell within the wall of a shell: $a$ = 6.31 Å, $b$ = 3.97 Å, $c$ = 32 Å, and $\alpha$ = 90°. The shaded planes of the unit cell represent the *00l* and *l00* lattice planes.

ation time constant for the shells at room temperature was measured and found to be unchanged. The only explanation for the shells not exploding when warmed gradually is that the permeability of the material changed as the shell expanded. By contrast, shells warmed rapidly explode as expected.

Once a thin-wall shell succumbs to an overpressure and bends, the intrinsic property of the material determines what happens next: brittle (plasma polymer, polystyrene) shells lack ductility and fracture into shards; polyimide, which is extremely elastic (typically tolerating up to 27% elongation), either collapses intact or tears apart, depending upon whether the overpressure is inside or outside the shell.

5. Surface Roughness of Polyimide Shells

Throughout this development program no effort has been made to optimize the smoothness of polyimide shells. This was considered a secondary priority, which would be addressed once the processing conditions and associated fundamental mechanical properties of the shell were accurately known.

Surface-roughness profiles of polyimide targets were acquired to establish a "typical" roughness power spectrum. Typically the roughness ranged from 0.5 to 1 $\mu$m with significant power throughout the spectrum. The low-order roughness was partially attributed to the quality of the mandrel on which the shell was formed; there had deliberately been no attempt to screen the quality of the mandrels for the smoothest and most-round ones because a large number of mandrels were required for the statistical study and the cost of analysis would have been prohibitive at that stage. The high-frequency roughness was corroborated with electron microscope images (Fig. 92.23) of the shells that showed "bumps" on the surface with lateral dimensions of 2 to 8 $\mu$m.

**Issues Regarding Shells Specific to Processing Cryogenic Targets**

1. Permeating Gas into Shells

The permeation coefficient ($P$) is the product of the diffusion coefficient ($D$) for a gas through a material and the solubility coefficient ($S$) of the gas in the material, where

$$P = S \times D = (\text{quantity of permeant}) \times (\text{wall thickness}) / [(\text{area}) \times (\text{time}) \times (\text{pressure drop across shell})]. \quad (3)$$

(The diffusivity has dimensions of area/time, and solubility has dimensions of molar-volume/pressure.)

The permeation time constant is an empirical figure of merit measured for all ICF capsules; it is the time required for 63% of the gas inside the shell to permeate out of the shell. This value depends on the wall thickness and the surface area and is independent of the pressure differential across the shell. Combining the time constant with the allowable buckling-pressure differential [Eq. (1)] gives the maximum rate at which a shell can be filled:

$$\text{Fill rate}(\text{atm/s}) = (\text{buckling} \times \text{pressure}) / (\text{permeation} \times \text{time} \times \text{constant}).$$

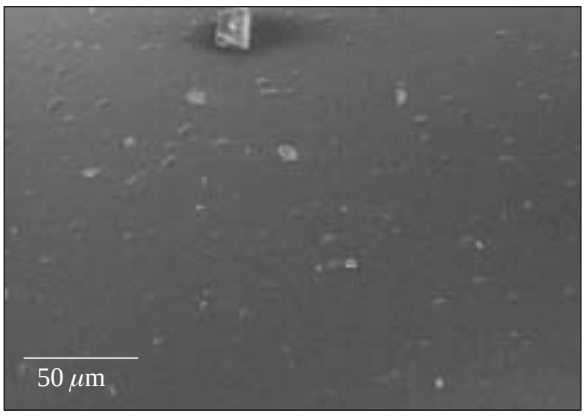


T1718a

Figure 92.23
Scanning electron micrograph of the surface of a 5-$\mu$m-wall PMDA-ODA shell. The overall surface is moderately smooth with the lateral dimensions of "bumps" below 10 $\mu$m. The larger particulates that are visible on the surface but removable are a consequence of the targets not being handled exclusively in a clean-room environment.

Direct-drive targets for experiments on the National Ignition Facility (NIF) are scaled versions of OMEGA targets and possess the same theoretical buckle pressures and time constants, so both types of shells can be filled at comparable rates. (Practically, larger-diameter targets are less spherical than smaller targets so the effective buckling pressure is marginally lower than would be expected by scaling smaller shells.) The larger diameter of a NIF target and the 350-$\mu$m-thick ice layer, however, will require 15 times more gas than an OMEGA target to achieve a scaled-thickness ice layer. A 100-$\mu$m ice layer for OMEGA targets requires approximately 1000 atm of gas at room temperature. (A 0.95-mm-diam shell at 295 K requires a fill pressure of 1027 atm to yield a 100-$\mu$m ice layer.) Filling targets at higher temperatures requires a higher pressure (1296 atm at 100°C for a 0.95-mm shell) since the gas density decreases with increasing temperature.

2. Effect of Temperature on the Permeability

Increasing the temperature not only increases the permeation rate but also decreases the elastic modulus (see Fig. 92.21), albeit less significantly, making permeation at elevated temperatures desirable. Table 92.II lists the time required to fill OMEGA and NIF direct-drive targets by permeation using different shell materials and different temperatures. Clearly, there is a major time benefit if shells can be filled at the maximum allowable temperatures. The maximum allowable temperature for the polyimide target is 400°C, which would require a fill pressure of 2210 atm, and the fill time would be reduced from 300 h to less than 10 h.

The temperature dependency of the permeability coefficient is given by

$$P = P_0 \exp\left(-E_p/\mathrm{RT}\right),$$

where $P_0$ is the pre-exponential value [$7 \times 10^{-28}$ mol m/(m s Pa) for polyimide] and $E_p$ (16.9 to 20.3 kJ/mol, depending upon the processing conditions) is the activation energy for permeation. The temperature dependency of the permeability of polyimide shells is reported from 130 K to 300 K[8,9] (Fig. 92.24) and for polyimide film to 523 K.[11]

3. Effect of Crystallinity on Permeability

The permeability of polyimide varies moderately according to the processing conditions and is affected by the crystallinity of the material. Permeation proceeds through a mechanism that requires polymeric chains to move over a very localized area to accommodate the movement of dissolved gas molecules through the plastic; this is referred to as the "segmental

Table 92.II: Calculated minimum time required to fill targets by permeation. The targets are (1) a 0.95-mm-diam shell with a 1-$\mu$m wall and a 100-$\mu$m ice layer for cryogenic experiments on OMEGA; and (2) a 3.4-mm-diam shell with a 3-$\mu$m wall and a 350-$\mu$m ice layer for cryogenic experiments on the NIF. Different permeation temperatures are presented where the mechanical and permeation properties are known. The $^3$He density increases at a rate of 0.02 mg/cm$^3$/day.

| Target | Permeation Time Constant (s) | Required Fill Pressure (atm) | Fill Time (h) |
|---|---|---|---|
| Plasma polymer at 295 K (OMEGA) | 10 | 1027 | 25.4 |
| Plasma polymer at 373 K (OMEGA) | 2.7 | 1296 | 8.5 |
| Plasma polymer at 295 K (NIF) | 106.8 | 101 | 375 |
| Plasma polymer at 373 K (NIF) | 28.5 | 1263 | 126 |
| Polyimide (PMDA-ODA formulation) at 295 K (OMEGA) | 184 | 1027 | 320 |
| Polyimide (PMDA-ODA formulation) at 573 K (OMEGA) | 1.8 | 1925 | 10.2 |

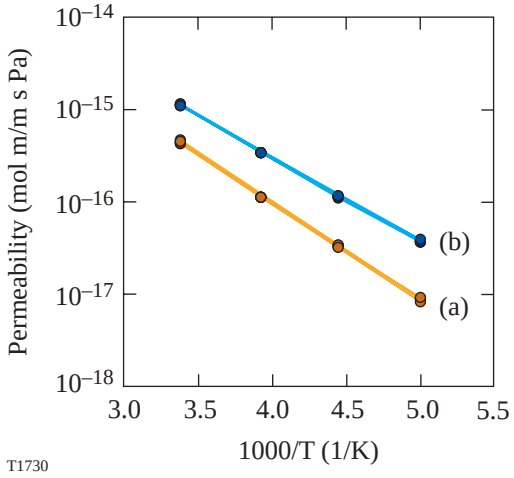


Figure 92.24
The temperature-dependent helium permeability of polyimide processed in nitrogen (a) is lower than when it is processed in air (b) due to the increased crystallinity and stiffness of the polymer.

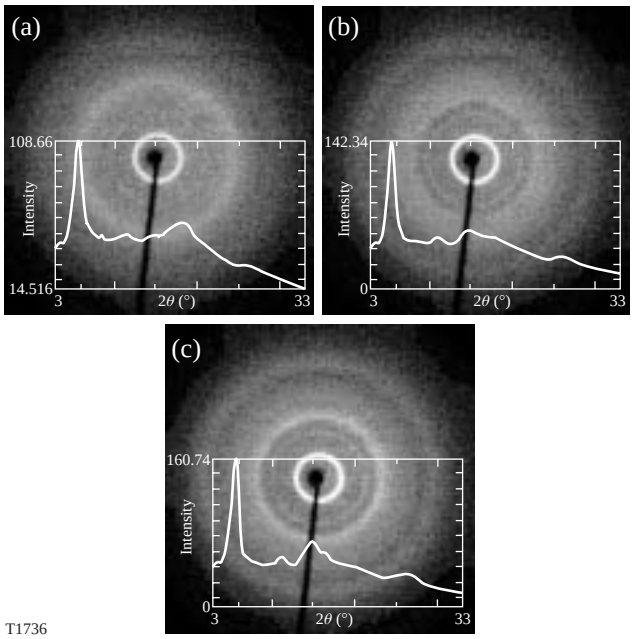


Figure 92.25
Comparison of transmission-mode x-ray diffraction patterns of polyimide shells imidized at increasing rates (a) 0.1 C/min, (b) 1 C/min, and (c) 5 C/min, together with integrated $2\theta$ plots. The increased intensity of the *002* peaks at 5.7°. $2\theta$ indicated greater crystallinity and is associated with lower permeability.

mobility" of the polymer. Amorphous material predictably is more permeable than crystalline material since the crystallinity increases the rigidity of the polymer chain. Another consideration is the scale length of the crystal: materials with similar overall crystallinity are more permeable if the crystalline regions are larger and more sparsely distributed than if there is a greater number of smaller, more-distributed regions—a channeling effect.[8,9]

The effect of changing an important processing variable—the imidization rate—is to change the size and distribution of crystals without changing the overall degree of crystallinity. Polyimide shells that are formed using a rapid imidization process (5 C/min) show more-intense, narrower 002 x-ray diffraction peaks than do polyimide shells that are made using a gradual imidization rate (0.1 C/min) (Fig. 92.25). The peaks of the rapidly imidized material are better aligned in the plane of the shell, as shown by grazing-angle x-ray diffraction data.[8,9] Finally, the material that was rapidly imidized has larger-scale, better-oriented crystalline regions that are more dispersed throughout the amorphous material, and this morphology corresponds to a more-permeable material.

By changing a second processing condition and imidizing polyimide shells in an air rather than a nitrogen atmosphere, the degree of crystallinity was reduced and the permeability of the material increased by 20%.

4. Effect of Mechanical Strain on the Permeability

Stressing polyimide beyond the yield stress—80 MPa at 3% strain—plastically deforms the material. (The ultimate yield stress of the vapor-deposited polyimide is 280 MPa at a biaxial strain of 27%.) As the polyimide shell is cooled inside the Cryogenic Target Handling System's (CTHS's) permeation pressure vessel, it is strained; the tensile and compressive nature of the strain varies over the entire temperature range as a complex function of the properties of the gas and materials at different temperatures. Given the exceptionally low buckling strength of the shell compared to the burst strength, it is desirable to maintain the shell in a regime where there is a net tensile (burst) force. This increases the risk that the stress may exceed the yield stress and the polyimide wall will be plastically deformed. The diameter of the shell will then increase, and the thickness of the ice layer will decrease proportionally, adding uncertainty to the dimensions of the target when it is shot. A maximum strain limit of 3% in the shell is the recommended design point for establishing the thermal performance of the permeation cell. Temperature gradients within the permeation cell, during either steady state or unsteady state, that translate into pressure gradients exceeding the 3% limit across the shell wall are unacceptable.

A consequence of biaxially straining polyimide shells beyond a 15% level is a change in the permeability of the material. As described above, approximately 1/3 of all shells strained to this level have an ~1000-fold increase in permeability. There are two intriguing aspects to this behavior: first, that the increased permeability is so sizeable, and second, that the behavior is stochastic. An explanation for this behavior is that strain introduces a microstructural change to the material. Supporting evidence is that the elastic modulus (stiffness) decreases by 56% (to 1.5 GPa) when strained and the crystallinity decreases substantially (see Fig. 92.26).[5,9,10] It is presumed that the statistical nature to the change in magnitude of the permeability is in the random initial distribution of crystalline and amorphous phases in the material, and the response of the material to the strain. Doubtlessly, strain changes the morphology; however, permeation will increase only if there is a contiguous alignment of highly mobile polymer chains through the shell wall—and this eventuality is statistical. Very important for confirming that this phenomenon is a microstructural event is the observation that the original elastic modulus and permeability values are returned when a strained and highly permeable shell is heated to 300°C. At the high temperature the plastic becomes more fluid and the strain-induced morphological change is reversed.

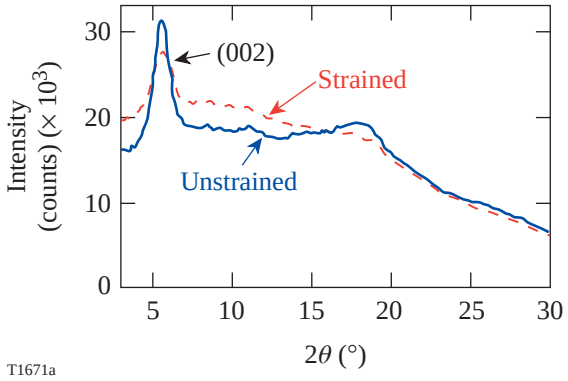


Figure 92.26
Comparison of transmission-mode x-ray diffraction patterns of polyimide shells for unstrained and mechanically biaxially strained polyimide shells showing appreciably greater crystallinity present in the unstrained shell.

5. Effect of Chemical Modification to the Polyimide on the Permeability

An alternative way to modify the segmental mobility of the polymer chain to enhance the permeability is to add flexible chemical units into the backbone of the polymer. Figures 92.19 and 92.27 compare the chemical formulation of two vapor-deposited polyimide shells: (a) the original PMDA-ODA–based polyimide discussed in detail here and (b) a 6FDA-ODA formulation that adds a flexible fluorine-based linkage to the polymer chain, respectively.[13,14]

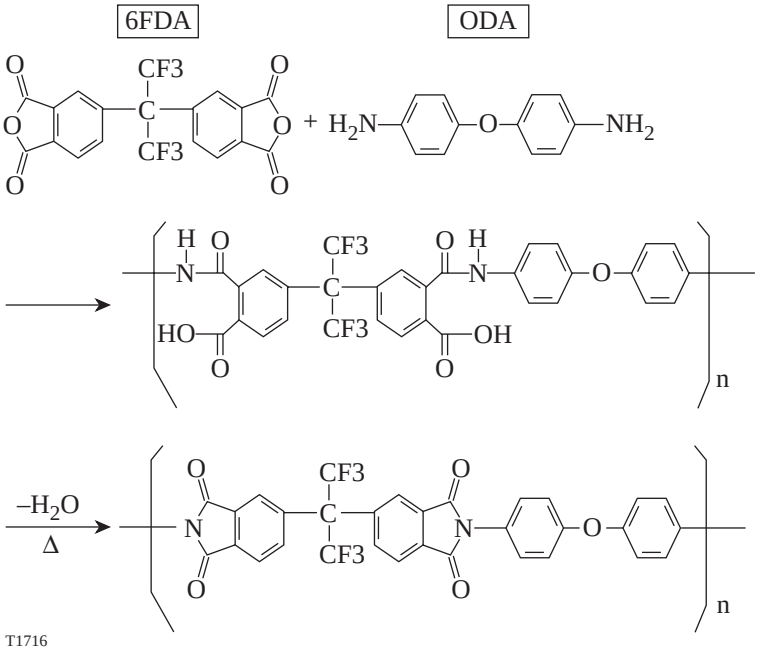


Figure 92.27
Structural and elemental composition of a permeable fluorinated-polyimide formulation.

The disadvantage of using the fluorinated polyimide for ICF experiments is the presence of fluorine (10 at. %) and the consequent x-ray preheat that will occur during an implosion. The advantages are numerous: The deuterium permeability is 50× greater than traditional PMDA-ODA–based polyimide, while the elastic modulus is only 18% lower. This reduces the time required to fill the shell with 1000 atm of deuterium at room temperature from 333 h to 8.8 h. (Note that this compares the fluorinated polyimide against the nonmechanically strained PMDA-ODA polyimide.)

The second advantage of using the polyimide based on 6FDA-ODA chemistry is the lower activation energy from permeation compared to polyimide made using PMDA-ODA chemistry, 12.3 versus 20.1 kJ/mol[12] (see Fig. 92.28). This will allow the fluorinated polyimide to retain higher permeability as the capsule is cooled (discussed in detail in the next section) to alleviate pressure differentials across the shell due to temperature gradients within the permeation pressure vessel.

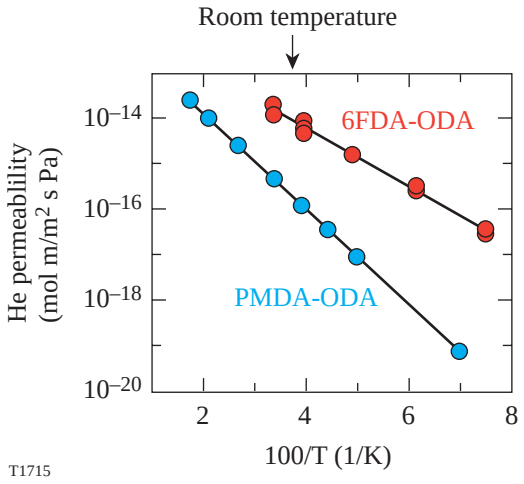


Figure 92.28
Arrhenius plot comparing the permeability of polyimide formulations: PMDA-ODA and 6FDA-ODA, over a wide temperature range.

6. Evaluation of Different Treatment Processes on the Processing Time Required to Fill Cryogenic Targets by Permeation

The critical parameters and the associated time required to fill OMEGA- and NIF-scale cryogenic shells are listed in Table 92.III for four different types of shells: (1) a standard plasma polymer shell, (2) a standard polyimide shell, (3) a polyimide shell structurally modified to enhance the permeability, and (4) a polyimide shell chemically modified to enhance the permeability. There is a clear time advantage, from a processing perspective, to using the more recently developed mechanically and chemically modified polyimide shells; however, these shells have other disadvantages when considering the processability of the target or the implosion performance of the target.

Table 92.III: Calculated minimum time to fill by permeation three different types of polyimide shells and a plasma polymer shell for OMEGA and the NIF. Target dimensions, respectively, are 0.95-mm-diam, 1.0-$\mu$m wall and 100-$\mu$m ice layer; and 3.5-mm-diam, 3.0-$\mu$m wall and 350-$\mu$m ice layer. The temperature is 295 K.

| Polyimide Material | Fill Time (h) (OMEGA) | Fill Time (h) (NIF) |
|---|---|---|
| Baseline polyimide (PMDA-ODA formulation) | 320 | 205 days |
| Mechanically strained polyimide (PMDA-ODA formulation) | 0.66 | 21 |
| Fluorinated polyimide (6FDA-ODA formulation) | 8.0 | 121 |
| High-density CH plasma polymer | 25.4 | 375 |

**Cooling Targets**

Once the permeation cycle is complete, the pressure inside the shell is equal to the pressure outside the shell. The entire pressure vessel is then cooled to 26 K. During this process the vessel must be cooled uniformly to minimize the pressure gradient that develops across the shell. Inevitably a thermal gradient will develop along the internal perimeter of the permeation pressure vessel and also between the perimeter and the center where the shell is located. This is the most-precarious phase for the survival of the target: while transient temperature gradients during cooling do not induce pressure gradients within the gas on the time scale of interest, a pressure gradient does develop across the shell wall.

The ideal shell material would be one with the highest-possible stiffness, strength, and yield strength (in both compression and tension) to resist the pressure difference, and the highest-possible permeability over the widest temperature range down to 30 K to alleviate the pressure differential. Finally, permeation must be negligible at 26 K, the temperature where the liquid/gaseous deuterium outside the shell is removed, leaving a shell containing 51 $\mu$g of liquid deuterium with a vapor pressure of ~2 atm. One last desirable property is that the material resists damage from electron radiation when tritium gas is used.

At the beginning of the cooling cycle, at temperatures where polyimide is still permeable, any pressure gradient is minimized by permeation. As the temperature decreases, the permeability of the shell also decreases. At lower temperatures, slower cooling rates are required to allow longer periods for the pressure gradient across the shell to be reduced. When the shell becomes impermeable, the survival of the shell depends on whether any further thermally induced pressure gradient exceeds the shell's buckle or burst strengths. If the thermally induced pressure gradients remain too high, the only remedy is to improve the thermal uniformity of the permeation pressure vessel.

Thermal modeling of the permeation cell in the OMEGA CTHS reveals that a 1-K temperature change at the perimeter induces a 0.5-atm pressure differential across the shell wall at 295 K and a 0.9-atm pressure differential at 60 K. At these densities the thermal diffusivity is moderately low, and the thermal time constant is ~30 s. This pressure differential creates a bursting force since the perimeter of the permeation vessel is colder and hence denser than the center of the vessel where the shell is located. This load is in addition to other phenomena such as the thermally induced contraction of the shell (which generates a net bursting pressure) and the temperature of the gas in the plumbing that connects the permeation vessel to a valve at room temperature (which creates a net buckling pressure). Depending on the cooling rate, the thermal uniformity of the permeation cell, and the temperature-dependent permeability of the polyimide, the shell can pass from a buckle to burst regime and back as the temperature decreases.

The weakest failure mode for shells is buckling, and the buckling strength of a thin-wall polyimide shell (nominal 1-$\mu$m wall) is 0.13 atm. The burst strength for a 1-$\mu$m wall shell is ~4 atm, whereas the yield strength is ~1 atm. A practical constraint in the design of the equipment is the accuracy of the silicon diode temperature sensor used to regulate the temperature ramp: in practice, the accuracy is ±0.5 K at 300 K. This value, the long thermal time constant for the permeation vessel, and the shorter thermal time constant for the gas to respond to temperature gradients combine to limit the value of using active temperature control over the temperature environment to minimize the likelihood of bursting/buckling the shell. Clearly the thermal environment within the pressure vessel has to be engineered to remain as constant as possible over a wide temperature and pressure range: from 18 K to 573 K and 1000 atm to a maximum of 2200 atm (33,000 psi), respectively.

The OMEGA Cryogenic Target Handling System has demonstrated that it is possible to process 0.95-mm-diam shells with walls as thin as 2.5 $\mu$m at room temperature over a period of three days. With the design goal being to process a 0.95-mm-diam shell with a 1-$\mu$m wall in less than two days, advanced shell materials and improved thermal engineering of the equipment are required. Greater strength will provide greater margin for the design of the permeation cell and will also offset possible strength degradation from radiation damage.

The future use of tritium adds two complications to the process: (a) hydrogen embrittles many metals, limiting the selection of available alloys for making the pressure vessel, and (b) the potential radioactive hazard requires heightened safeguards.

**Radiation Effects**

The decay of a triton produces an electron with a mean energy of 6 keV and an energy range of 2 to 18 keV.[6] The effect of this electron on a polymer is to rupture chemical bonds and weaken the material.[6] Given the high DT density in a target (0.11 gm/cm$^3$ for pressurized gas and 0.25 gm/cm$^3$ for ice), the stopping power of the medium is appreciable and the 1/*e*

penetration distance is less than 30 $\mu$m. Consequently, only tritium dissolved in the plastic wall and the tritium immediately adjacent to the plastic wall damage the plastic.

During the processing of cryogenic targets there are three phases where tritium decay is an issue: (1) during the pressure ramp, (2) during the cooling cycle, and (3) during layering. During the pressure ramp (0.05 atm/min for a 1-$\mu$m-wall shell) the dose from the tritium dissolved in the wall (assuming 10% solubility at 1 atm scales linearly with increasing pressure) will be approximately 50 MGy. Added to this is the contribution from tritium adjacent to the shell wall, which is less than 2 MGy. During cooling at a rate of 0.1 K/min, the dose will be 6 MGy, the majority coming from gas dissolved in the plastic and less than 1 MGy from the adjacent gas volume. When ice has formed and layered, the dose, primarily from the adjacent ice layer, will be 0.3 MGy/h. This contribution is smaller since the 1/*e* penetration distance is only 9 $\mu$m at ice density and the amount of tritium dissolved in the wall is negligible. Allowing 36 h to layer and deliver a target, the total dose to the shell material may be expected to be of the order of 70 MGy. These radiation doses are estimates based on the penetration distance of 6-keV electrons at discrete temperatures and densities. A rigorous analysis would be considerably more complex and require more-detailed information than is available. The purpose of this analysis was to estimate the dosage for subsequent radiation-induced damage experiments.

In an effort to quantify the effect that radiation damage from tritium decay may have on polyimide, polyimide shells were irradiated with an electron beam from a scanning electron microscope. The electron energy was 8 keV, and the current flux calculated to be 7 mA/m$^2$. The total integrated dose was 60 and 120 MGy. The results are summarized as follows: the elastic modulus showed no change with exposure; the tensile strength decreased from 280 MPa (initially) to 266 MPa at the 60-MGy dose and 240 MPa at the 120-MGy dose; and the permeability did not change with dose. The property that showed the biggest change was the elasticity/plasticity of the system: the maximum elongation that polyimide can withstand is 27%. Exposure to 60 MGy reduces this to 20%, and exposure to an additional 60 MGy further reduces this to 14%. None of these performances will impair polyimide sufficiently to affect the likely survivability of the shell, but two important issues remain: any impairment to the yield strain was not determined, and any change in the transparency of the material was not investigated.

The observed radiation resistance is an important consideration when evaluating polyimide material as a potential shell material. Literature values for the performance of polystyrene (which possesses a chemical composition similar to plasma polymer) suggest that the mechanical properties are considerably more impaired than for heavily conjugated organic structures such as polyimide.[6]

**Conclusions**

Polyimide shells suitable for ICF cryogenic experiments on OMEGA were developed, and the associated mechanical properties were determined to define the processing conditions for operating the OMEGA Cryogenic Target Handling System. Overall, polyimide targets offer a viable alternative to plasma polymer capsules currently in use. The greatest virtue for the polyimide material is its high radiation resistance (for tritium application) and its excellent mechanical properties, which lessen the demanding specifications for the equipment needed to provide cryogenic targets.

The single biggest limitation to using the most thoroughly developed and characterized polyimide, based on PMDA-ODA chemistry, is the low permeability of the material at room temperature. This increases the processing time and exacerbates the deleterious effect of $^3$He production on the performance of the implosion. Importantly, there are solutions to this problem, but each has its own implications: (1) The permeation time can be reduced substantially by filling shells at elevated temperature (up to 300°C), but this adds to the complexity of the cryogenic system needed to provide these targets. (2) The permeability can be dramatically increased by mechanically straining polyimide to modify the crystalline microstructure of polyimide, which achieves the shortest-possible fill time. The technique has not been thoroughly developed, however, and cannot yet be relied upon for routine production: the yield is low and the magnitude and effect of the shell deformation during the process remain too variable and not fully determined. The production aspects for this process have to be developed further. (3) The final option for increasing the permeability of polyimide is the most promising: change the chemical formulation to add flexibility to the polymer chain. Not only does this increase the permeability at room temperature, but it also increases the permeability of the material over a broad temperature range—a property that will increase the survivability of thin-wall targets during processing. The disadvantage of this approach is the presence of fluorine in the polymer and the effect fluorine has on the implosion physics.

## REFERENCES


1. S. A. Letts *et al.*, Fusion Technol. **28**, 1797 (1995).
2. J. J. Sanchez and S. A. Letts, Fusion Technol. **31**, 491 (1997).
3. E. L. Alfonso, S. H. Chen, R. Q. Gram, and D. R. Harding, J. Mater. Res. **13**, 2988 (1998).
4. F.-Y. Tsai, E. L. Alfonso, S. H. Chen, and D. R. Harding, Fusion Technol. **38**, 83 (2000).
5. F.-Y. Tsai, D. R. Harding, S. H. Chen, T. N. Blanton, and E. L. Alfonso, Fusion Sci. Technol. **41**, 178 (2002).
6. *Safe Handling of Tritium: Review of Data and Experience*, Technical Reports Series No. 324 (IAEA, Vienna, 1991).
7. E. H. Baker, L. Kovalevsky, and F. L. Rish, *Structural Analysis of Shells* (McGraw-Hill, New York, 1972).
8. F.-Y. Tsai, T. N. Blanton, D. R. Harding, and S. H. Chen, "Temperature Dependency of the Properties of Vapor-Deposited Polyimide," to be published in the Journal of Applied Physics.
9. F.-Y. Tsai, "Engineering Vapor-Deposited Polyimides," Ph.D. thesis, University of Rochester, 2002.
10. F.-Y. Tsai, E. L. Alfonso, D. R. Harding, and S. H. Chen, J. Phys. D: Appl. Phys. **34**, 3011 (2001).
11. *Polyimides: Fundamentals and Applications*, edited by M. K. Ghosh and K. L. Mittal, Plastics Engineering, Vol. 36 (Marcel Dekker, New York, 1996).
12. Laboratory for Laser Energetics LLE Review **81**, 6 and 21, NTIS document No. DOE/SF/19460-335 (1999). Copies may be obtained from the National Technical Information Service, Springfield, VA 22161.
13. A. Nikroo, General Atomics, private communication (2002).
14. F.-Y. Tsai, D. R. Harding, S. H. Chen, and T. N. Blanton, "High-Permeability Fluorinated Polyimide Microcapsules by Vapor-Deposition Polymerization," to be published in Polymer.

# Anomalous Stimulated Raman Scattering and Electron Acoustic Waves in Laser-Produced Plasmas: A Linear Model

Stimulated Raman scattering (SRS), an instability in which light is scattered by and amplifies electron plasma waves, has long been a concern in laser-fusion research because of its potential to reduce absorption and implosion efficiency. This concern is enhanced by the unsatisfactory state of the theory, particularly in accounting for the prevalence of anomalous SRS—scattering from plasma waves that according to conventional theory should be very heavily Landau damped.[1–5] Furthermore, scattering from waves satisfying the electron-acoustic (EA) dispersion relation (see below), which according to conventional theory should also be very heavily damped, has recently been identified.[2,4] These observations imply that Landau damping in laser-produced plasmas is often lower by an order of magnitude than would be predicted by the conventional linear theory of waves in a Maxwellian plasma.[5]

Since nonlinear Berstein–Green–Kruskal (BGK)[6] waves are undamped and under some conditions satisfy the EA dispersion relation,[7] they have recently been invoked to account for these phenomena.[2,4,8] However, the observed EA wave scattering (as well as much of the anomalous SRS) is at low levels, so that the fundamental question is how the associated plasma waves are amplified from small amplitudes (noise) despite prohibitive linear damping, rather than how they behave at large amplitudes. While nonlinear analysis has a place in modeling large-amplitude processes such as saturation, it seems appropriate to seek a linear explanation of the small-amplitude aspects of anomalous SRS and EA waves.

We begin by observing that the undamped nature of BGK waves stems not from their nonlinearity but rather from the fact that they represent a local flattening of the distribution function at the wave phase velocity (since the trapped distribution must be an even function of velocity in the wave frame). Our model of anomalous SRS posits a local flattening of the distribution function resulting from Landau damping of thermal noise driven by SRS. We shall see that such a locally flattened distribution function (LFDF) supports linear waves with reduced damping and enhanced SRS growth. Flattening resulting from Landau damping is a well-known process and represents a nonlinear modification of the original Maxwellian but does not imply the formation of BGK waves. In fact the evolution of the flattening is usually analyzed using so-called quasi-linear (that is, nonlinear only in the sense that it involves products of linear wave quantities) theory,[9] as a result of the damping of a continuum of linear waves. For our purposes the significant properties of the flattening (its location, width, etc.) can be ascertained from linear theory, and a detailed nonlinear analysis of the dynamics of the flattening process is unnecessary. We first demonstrate that a LFDF arbitrarily close to a Maxwellian supports linear undamped plasma waves. We take a model LFDF of the form

$$f(u) = f_0(u) + f_1(u) + f_2(u), \tag{1a}$$

where

$$f_0(u) = \frac{1}{\sqrt{\pi}} e^{-u^2}, \tag{1b}$$

$$f_1(u) = -f_0'(u_0)(u-u_0) e^{\frac{(u-u_0)^2}{(\Delta u)^2}}, \tag{1c}$$

and

$$f_2(u) = \frac{1}{3}\left[\beta - f_0''(u_0)\right]\left[(u-u_0)^2 - \frac{1}{2}(\Delta u)^2\right] e^{\frac{(u-u_0)^2}{(\Delta u)^2}}. \tag{1d}$$

Velocities are normalized to $\sqrt{2}v_T$, where $v_T$ is the electron thermal velocity. The model thus comprises a Maxwellian that has been "flattened" near $u_0 = v_0/\left(\sqrt{2}v_T\right)$ over the range $\Delta u$, so that $f'(u_0) = 0$ and $f''(u_0) = \beta$, an arbitrary parameter. Note that $\int_{-\infty}^{\infty} f(u)\,du \equiv 1$ and that $f(u)$ is an analytic function of $u$ that becomes arbitrarily close in $L_p$ norm to the Maxwellian $f_0(u)$ as $\Delta u$ is made small.

The corresponding dielectric function for waves of frequency $\omega$ and wave number $k$ is given by

$$\varepsilon(k,\omega) = 1 - \frac{1}{2(k\lambda_D)^2}\int_{-\infty}^{\infty} \frac{f'(u)}{u - \dfrac{\omega}{\sqrt{2}kv_T}}\,du. \qquad (2)$$

Substituting (1a)–(1d) into (2) gives

$$\varepsilon(k,\omega) = 1 + \frac{1}{(k\lambda_D)^2}\left[1 + \Omega Z(\Omega)\right]$$

$$+ \frac{u_0 e^{-u_0^2}}{(k\lambda_D)^2}\left[2y + \left(2y^2 - 1\right)Z(y)\right]$$

$$+ \frac{\Delta u}{(k\lambda_D)^2}\left[\frac{\sqrt{\pi}}{2}\beta + \left(1 - 2u_0^2\right)e^{-u_0^2}\right]$$

$$\times\left[\frac{2}{3}\left(y^2 - 1\right) + \left(\frac{2}{3}y^3 - y\right)Z(y)\right], \qquad (3)$$

where $Z$ denotes the plasma dispersion function, $\Omega \equiv \omega/\left(\sqrt{2}kv_T\right)$, and $y \equiv (\Omega - u_0)/\Delta u$. The first two terms on the right of (3) give $\varepsilon_0(k,\omega)$ the dielectric function for a Maxwellian.

For each value of $k\lambda_D$ there are an infinite number of roots of (3). For the Maxwellian case, the least-damped root is usually referred to as "the" electron plasma wave; the other roots are very heavily damped and have little physical significance.[10] The flattening in the LFDF case introduces a new set of roots corresponding to waves with phase velocities near $u_0$. The least damped of these has much smaller damping than the plasma wave for large $k\lambda_D$. It is of interest to determine the conditions under which the damping of this root vanishes. In that case $\Omega$ is real, and

$$Z(\Omega) = i\sqrt{\pi}e^{-\Omega^2} - 2\ \mathrm{Daws}(\Omega),$$

where the Dawson function is defined as

$$\mathrm{Daws}(x) \equiv e^{-x^2}\int_0^x e^{t^2}\,dt = \frac{1}{2}\sqrt{\pi}e^{-x^2}\,\mathrm{erfi}(x).$$

Then for $\Omega = u_0$ we see from (3) that $\mathrm{Im}(\varepsilon) = 0$, and the condition for a root as $\Delta u \to 0$ is

$$1 + \left[1 - 2\Omega\,\mathrm{Daws}(\Omega)\right]\Big/(k\lambda_D)^2 = 0,$$

which is just the dispersion relation for electron-acoustic waves in a Maxwellian plasma. Electron-acoustic modes were proposed in 1962 by Stix,[11] who speculated that a particular relative drift velocity of electrons and ions might cancel $\mathrm{Im}\left[\varepsilon(\omega,k)\right]$ and allow such modes to exist. As this seemed rather contrived, EA modes attracted little interest and were dropped from the second edition of Stix's book.[12] The experimental observation of scattering from EA waves[4] therefore came as somewhat of a surprise, and at first they were not recognized as such.[13] We will return to EA waves after investigating anomalous SRS in a LFDF.

We combine in the usual way[14] the electromagnetic equations for the pump and scattered light waves with the dielectric function for the plasma waves (3) to obtain the dispersion relation for SRS backscatter:

$$D(k,\omega) \equiv \varepsilon(k,\omega)\left[(\omega - \omega_0)^2 - (k - k_0)^2c^2 - \omega_p^2\right]$$

$$-\left[1 - \varepsilon(k,\omega)\right]\frac{k^2 v_{\mathrm{osc}}^2}{4} = 0. \qquad (4)$$

Here $k_0$ and $\omega_0$ are the wave number and frequency of the pump (laser) wave, $\omega_p$ is the electron-plasma frequency (a homogeneous plasma and fixed ions are assumed), and $v_{\mathrm{osc}} \equiv eE_0/m\omega_0$ is the electron quiver velocity in the laser field $E_0$.

We begin by studying a Maxwellian (unflattened) plasma, substituting $\varepsilon_0$ $(k,\omega)$ in (4). Temporal growth rates of the SRS instability are found by solving (4) for $\omega$ as a function of $k$. The growth rate is a maximum at the resonance where both factors of the first term in (5) are small. Figure 92.29 shows normalized growth rates $\gamma/\left(\sqrt{2}\,kv_T\right)$ for a laser intensity of $10^{15}$ W/cm$^2$, temperature of 4 keV, and various values of the normalized electron-plasma density $n/n_c = \omega_p^2/\omega_0^2$, where $n_c$ is the critical density. In the absence of damping, the growth

rate would be $\gamma_0/\left(\sqrt{2}kv_T\right) \sim 10^{-2}$, so it is evident that Landau damping has substantially decreased the growth rate. Note that the resonant value of $k\lambda_D$ increases and the resonance becomes broader as the density decreases.

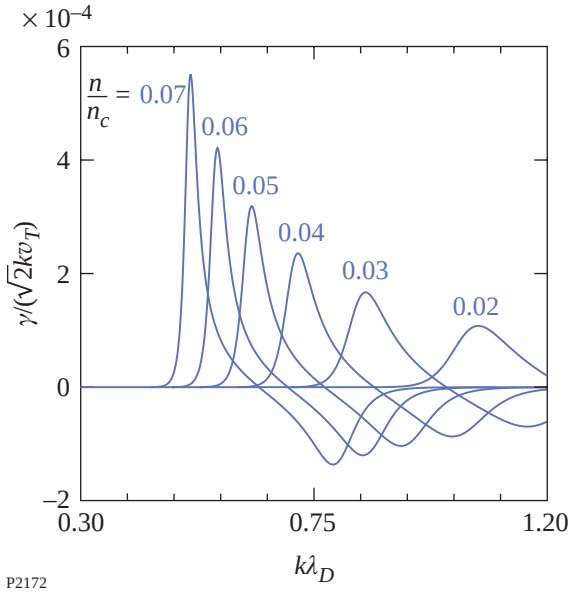


Figure 92.29
The SRS growth rates in a Maxwellian plasma with an incident laser intensity of $10^{15}$ W/cm$^2$ and an electron temperature of 4 keV.

Since monotonic distribution functions support only damped waves, we may expect the localized distortion of the distribution function resulting from damping of the SRS-driven plasma waves to continue until there is a point of inflection at the wave phase velocity. Such a situation can be represented by a LFDF with $\beta = 0$. To model the flattening effect of SRS we choose the flattening velocity $u_0 = \mathrm{Re}\left(\Omega_{\max}\right)$, where $\Omega_{\max}$ is the root corresponding to the peak growth rates in Fig. 92.29. The effects of interest are insensitive to $\Delta u$ as long as it is small, so we take $\Delta u = 0.1$. Results for a density of $n/n_c = 0.05$ are shown in Fig. 92.30(a). The upper line represents the electromagnetic mode, effectively undamped in hot, low-density plasma, and the lower curve represents the least-damped plasma mode. In the absence of the pump these two modes would propagate independently, but the coupling due to the pump produces the SRS instability near the resonance at $k\lambda_D \cong 0.63$. Owing to the reduced Landau damping of the plasma mode resulting from the flattening, the peak SRS growth rate is larger than in Fig. 92.29 for the same plasma conditions by a factor of ~3. Note that the flattening has also resulted in an undamped electron-acoustic mode at $k\lambda_D \cong 0.5$. This mode does not satisfy the wave-vector-matching conditions for Raman scattering, however, so it is not driven.

While substantially reduced by the flattening, the Landau damping of the SRS plasma mode in Fig. 92.30(a) is still significant. This damping will continue the net transfer of particles from velocities below $u_0$ to velocities above $u_0$ until the wave is undamped. We may thus expect the flattening to overshoot, resulting in a small secondary maximum of the distribution function near $u_0$. This situation can be modeled by a nonzero value of $\beta$; the value of $\beta$ giving an undamped plasma wave at the SRS matching wave vector is

$$\beta = \frac{3}{\sqrt{\pi}}\left[\frac{1+\left(k\lambda_D\right)^2 - 2u_0\,\mathrm{Daws}\left(u_0\right)}{\Delta u} + \frac{2}{3}\left(2u_0^2 - 1\right)e^{-u_0^2}\right].$$

For the parameters of Fig. 92.30, $\beta \cong 2.54$, and the resulting plot is seen in Fig. 92.30(b). The reduction in damping of the plasma mode has increased the peak SRS growth rate as seen at $k\lambda_D \cong 0.63$ in Fig. 92.30(b) by a factor of ~3 over the SRS growth rate in Fig. 92.30(a). Note however that, owing to the secondary maximum of the distribution function, the EA mode has now become unstable, with an even larger growth rate than the SRS. This suggests that the EA wave may quickly grow to large amplitudes and disrupt the SRS process. Such a quench-

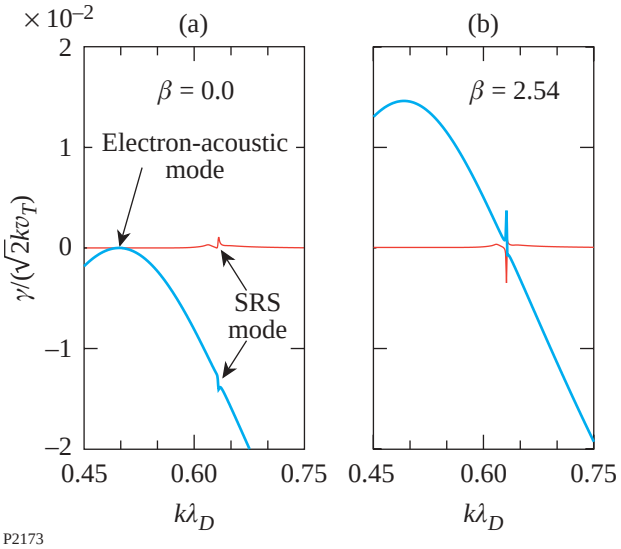


Figure 92.30
(a) The imaginary parts of the two least-damped roots of the SRS dispersion relation for a flattened distribution with $u_0 = 1.71$, corresponding to the peak of the SRS growth curve in Fig. 92.29 for $n/n_c = 0.05$. (b) The same distribution function, but with $\beta$ increased to give zero damping of the plasma mode at the SRS resonance.

ing mechanism may be related to the intermittent interruptions in the SRS reflectivity seen in simulations [Fig. 1(a) of Ref. 15] and may help to explain why anomalous SRS reflectivities saturate at much lower levels than standard (small $k\lambda_D$) SRS reflectivities, though both have similar initial growth rates (see, e.g., Fig. 4 of Ref. 5). It is also noteworthy that the SRS growth rate peak in the $\beta = 0$ case is much narrower than in the original Maxwellian and consists of a sharp peak with a smaller subsidiary peak at slightly smaller $k\lambda_D$; this strongly resembles the form of the plasma-wave spectrum seen in SRS simulations [Fig. 1(b) of Ref. 15].

This analysis of anomalous SRS has been based on a locally flattened Maxwellian, an idealization capturing the essential aspects of a distribution function modified by Landau damping while remaining mathematically tractable. However, the Maxwellian itself represents an idealization; in a real plasma, thermal and other fluctuations are continually causing local, temporary distortions in the form of the distribution function. In particular, we may expect that such local distortions will on occasion result in a reduction or elimination of the slope of the distribution function. As noted above, such a distortion may represent an arbitrarily small deviation from the Maxwellian and still allow propagation of undamped EA waves. As the slope of the distribution function relaxes back to its equilibrium value, such a wave would ordinarily become heavily Landau damped and disappear. However, if it satisfies the frequency and wave-number-matching conditions for SRS, it will be driven just as the plasma wave in the case of anomalous SRS, resulting in amplification of the EA wave, maintenance of the local flattening by Landau damping, and the production of scattered light.

Such scattering has recently been seen at low levels in experiments,[4] though it was attributed to a nonlinear EA-like BGK mode. In fact, Refs. 4 and 8 suggest that such waves are the source of anomalous SRS and, on that basis, propose limiting SRS reflectivities in NIF targets by modifying plasma parameters so that $k\lambda_D > 0.53$ for the SRS-driven BGK wave (such waves are limited to $k\lambda_D < 0.53$). However, experiments in which SRS originates from low densities indicate that this nonlinear interpretation is implausible. To see this it is useful to combine the EA dispersion relation with the SRS resonance conditions to obtain a relation between the scattered light wavelength and the density at which scattering occurs. This relation is shown in Fig. 92.31 for the plasma parameters of the experiments in Ref. 3 (laser wavelength 351 nm, electron temperature $T_e \cong$ keV). Note that EA-wave scattering does not occur at densities below 0.08 critical; this is related to the $k\lambda_D < 0.53$ restriction (at lower densities the Debye length becomes too large to satisfy this condition for the SRS $k$). At higher densities there are two possible scattered wavelengths; the upper solution corresponds to plasma-wave scattering and the lower to EA-wave scattering.

Two types of experiments are described in Ref. 3. In the first, an interaction beam is focused on a relatively homogeneous plasma formed by an exploding foil; the density in the interaction region is (from hydro simulations) about 0.2 critical. From Fig. 92.31 it is seen that plasma waves at this density produce scattered light at about 650 nm, and that is what is seen in the experiment. No EA-wave scattering (at about 450 nm) is detected. In the second type of experiment, however, the interaction beam is focused on a plasma derived from a solid target, so that a full range of densities down to vacuum is represented in the interaction region. The SRS spectrum in these experiments extends from 420 to 540 nm, indicating that low densities are necessary to produce scattering at these wavelengths. The absence of SRS at higher densities is likely due to the steeper density gradients there that hydro simulations show in the solid-target experiments; such gradients would equally rule out EA waves at these densities as the source of the scattering. The scattering is, however, consistent with anomalous SRS from plasma waves in densities $\lesssim$0.04 critical. At such densities and temperatures (~4 keV) EA

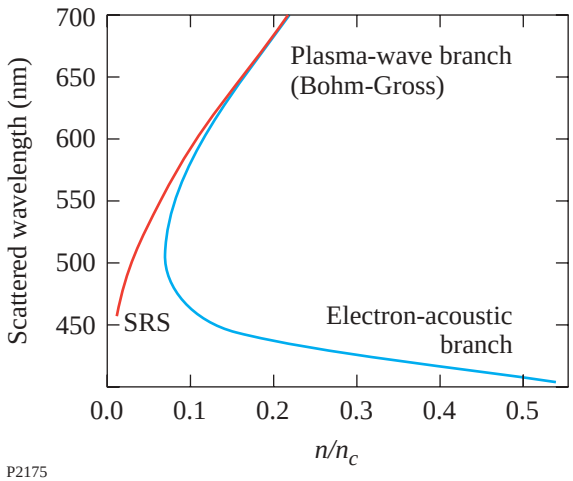


Figure 92.31
The scattered wavelength as a function of density for incident laser wavelength 351 nm for EA scattering and SRS. At long scattered wavelengths both waves approach the Bohm-Gross dispersion relation but diverge at shorter wavelengths (larger $k\lambda_D$).

scattering does not exist, and reduced damping of the SRS plasma wave ($k\lambda_D \sim 1$) is required to account for the dominance of these wavelengths in the observed spectrum. Local flattening of the distribution function as described above therefore seems the most satisfactory explanation for these results.

In summary, the model presented here shows that linear waves in a locally flattened distribution function can account for both anomalous SRS and EA-wave observations. Several predictions of the linear model differ qualitatively from those of the nonlinear approach. Among these: the linear model accommodates coexistence of SRS and EA waves, as seen in Refs. 4 and 13, and the occurrence of SRS at very low densities, as in Ref. 3. The linear model also suggests that proposals[2,4,8] to eliminate SRS in the NIF by altering plasma parameters so that $k\lambda_D > 0.53$ may not be successful.

## ACKNOWLEDGMENT

This work was supported by the U.S. Department of Energy Office of Inertial Confinement Fusion under Cooperative Agreement No. DE-FC03-92SF19460, the University of Rochester, and the New York State Energy Research and Development Authority. The support of DOE does not constitute an endorsement by DOE of the views expressed in this article.

## REFERENCES

1. A. Simon, W. Seka, L. M. Goldman, and R. W. Short, Phys. Fluids **29**, 1704 (1986) and references therein.

2. D. S. Montgomery *et al.*, Phys. Plasmas **9**, 2311 (2002).

3. S. P. Regan, D. K. Bradley, A. V. Chirokikh, R. S. Craxton, D. D. Meyerhofer, W. Seka, R. W. Short, A. Simon, R. P. J. Town, B. Yaakobi, J. J. Caroll III, and R. P. Drake, Phys. Plasmas **6**, 2072 (1999).

4. D. S. Montgomery *et al.*, Phys. Rev. Lett. **87**, 155001 (2001).

5. J. C. Fernandez *et al.*, Phys. Plasmas **7**, 3743 (2000).

6. I. B. Bernstein, J. M. Greene, and M. D. Kruskal, Phys. Rev. **108**, 546 (1957).

7. J. P. Holloway and J. J. Dorning, Phys. Lett. A **138**, 279 (1989); J. P. Holloway and J. J. Dorning, Phys. Rev. A **44**, 3856 (1991).

8. H. A. Rose and D. A. Russell, Phys. Plasmas **8**, 4784 (2001).

9. E. M. Lifshitz and L. P. Pitaevskifi, *Physical Kinetics*, 1st ed., Course of Theoretical Physics, Vol. 10 (Pergamon Press, Oxford, 1981), pp. 199–205.

10. These correspond to the alternative definition of electron-acoustic modes; see Ref. 11.

11. T. H. Stix, *The Theory of Plasma Waves* (McGraw-Hill, New York, 1962), p. 218. The term "electron-acoustic wave" is also often used to refer to the infinite set of solutions to the Landau dispersion relation other than the least-damped one [e.g., D. C. Montgomery, *Theory of the Unmagnetized Plasma* (Gordon and Breach, New York, 1971), p. 69]. Since in the past all these modes were usually mentioned only to be dismissed, many authors confuse or conflate the two definitions; our usage conforms to that of Stix.

12. T. H. Stix, *Waves in Plasmas* (American Institute of Physics, New York, 1992).

13. J. A. Cobble *et al.*, Phys. Plasmas **7**, 323 (2000).

14. J. F. Drake *et al.*, Phys. Fluids **17**, 778 (1974).

15. H. X. Vu, D. F. DuBois, and B. Bezzerides, Phys. Plasmas **9**, 1745 (2002).

# Time Delay of the Resistive-State Formation in Superconducting Stripes Excited by Single Optical Photons

Recently proposed superconducting single-photon detectors (SSPD's), based on ultrathin, submicrometer-width NbN superconducting stripes, are characterized by picosecond response times, high quantum efficiency, broadband single-photon sensitivity, and extremely low dark counts.[1,2] The devices have immediately found a variety of applications ranging from noninvasive testing of very-large-scale integrated (VLSI) circuits[3] to quantum cryptography.[4,5] Their single-photon-counting ability has been interpreted within a phenomenological hot-electron photoresponse model proposed in Ref. 1 and elaborated in Ref. 6. The model describes the formation of a hotspot,[7] right after the single-photon absorption event, followed by in-plane growth of a resistive hotspot area due to the high efficiency of the excited quasiparticle multiplication process in NbN films.[8] During this stage, however, the resistive state does not appear across the superconducting stripe because the size of a single normal hotspot, created by an optical photon, is significantly smaller than our stripe width.[2] The resistive state appears due to a supplementary action of the device's bias current density $j$, which should be close to the stripe's critical current density $j_c$. After the supercurrent is expelled from the normal hotspot region, the bias current density in the stripe's "sidewalks" $j_{sw}$ exceeds $j_c$ [see Fig. 92.32(c)], resulting in the penetration of the electric field in the sidewalk areas of the stripe.[6] As a result, we observe a voltage pulse that reflects the initial act of photon capture.

The resistive-state development process presented above should lead to an experimentally observable time delay in the superconducting stripe's resistive photoresponse.[9] This delay, in turn, if measured, would give direct confirmation of a supercurrent-enhanced, hotspot-induced photoresponse mechanism of our SSPD.[1]

The dynamics of the resistive-state formation in a photon-illuminated, two-dimensional (2-D) superconducting stripe depends on the radiation flux density incident on the device and the bias current density, as is schematically illustrated in Fig. 92.32. At relatively high (macroscopic) incident photon fluxes, a large number of hotspots are simultaneously formed in our superconducting stripe [Fig. 92.32(a)]. In this case, the hotspots overlap with each other across a cross section of the stripe. Since the stripe thickness $d$ is comparable with coherence length $\xi$, we can assume that for overlapping hotspots, a resistive barrier is instantaneously formed across the NbN stripe and, as a result, a voltage signal is generated within an electron thermalization time of 6.5 ps.[10] When the photon flux is decreased, the hotspots become isolated [Fig. 92.32(b)]. Finally, for the flux containing one or less than one absorbed photon per pulse, we can expect that, at best, only one resistive

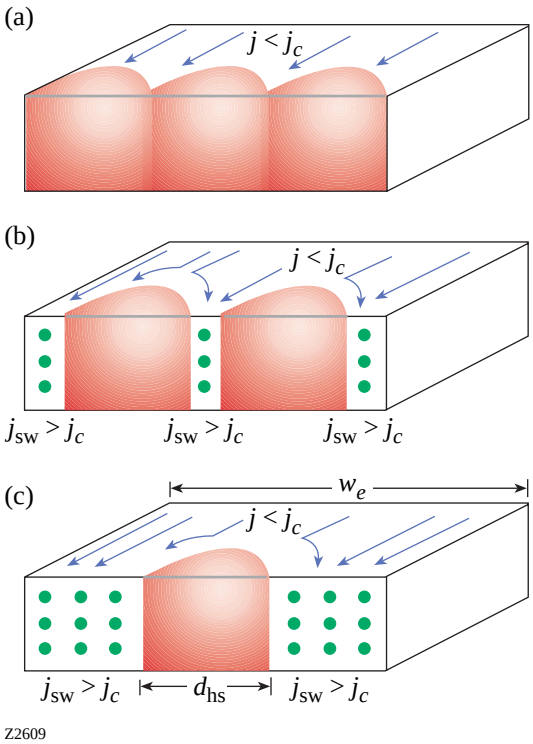


Figure 92.32
Schematic presentation of the dynamics of resistive-barrier formation across a superconducting stripe: (a) high (macroscopic) incident photon flux, (b) the two-photon regime, leading to the generation of two hotspots in the cross section of the superconducting stripe, and (c) the single-photon regime.

hotspot will be formed in our stripe [Fig. 92.32(c)]. As we mentioned above, in the single-photon regime, we postulate that the formation of a macroscopic resistive barrier can be realized only when $j_{sw}$ surpasses $j_c$, which is associated with macroscopic current redistribution and should lead to a certain time delay in the resistive-state formation.

Even if the two-photon detection mechanism[1,2] does not correspond exactly to the situation presented in Fig. 92.32(b) since the hotspots can either partially overlap or coincide, the scenario illustrated in Fig. 92.32(b) should result in a measurable time delay $t_d$ for the voltage pulse generation, corresponding to the time period between the initial hotspot appearance and the eventual development of a resistive barrier across the entire cross section of the superconducting stripe. In terms of the superconductor dynamics, $t_d$ is the time required for a superconductor energy gap $\Delta$ to be reduced to zero by the current in the sidewalks and, for $j_{sw} > j_c$, can be calculated using the Tinkham model[11] as

$$t_d = 2\tau_\Delta \int_0^1 \frac{f^4}{\left[2j_{sw}/\left(3\sqrt{3}j_c\right)\right]^2 + f^6 - f^4}\, df, \qquad (1)$$

where $\tau_\Delta \cong 2.41\tau_E/\sqrt{1-T/T_c}$ is the gap relaxation time[9] ($\tau_E$ is the inelastic electron–phonon collision time at the Fermi level at $T_c$) and $f = \Delta/\Delta_0$ ($\Delta_0 = \Delta$ at 0 K).[11]

The devices used in our experiments were $4 \times 4$-$\mu$m$^2$-area, meander-type, NbN stripes with $d$ = 10 nm, a nominal width $w$ = 130 nm, and the total length of about 30 $\mu$m. The structures were superconducting at $T_c$ = 10.5 K and exhibited $j_c = 6 \times 10^6$ A/cm$^2$ at 4.2 K. Details of their fabrication and implementation as SSPD's are described in Refs. 2 and 4; here we only wanted to stress that with the constant $j_c$, $I_c$ of the meander is determined by its narrowest segment, and, according to our supercurrent-enhanced, resistive-state formation model, the narrowest segments of the stripe contribute the most to the SSPD photoresponse.[2] The atomic force microscope images showed that irregularities in our stripes were up to 25 nm, close to the cantilever resolution limit. At the same time, the $I_c$ of the meander structures, measured at 4.2 K, was typically 60% lower than $I_c$ for the control (short) stripe fabricated in the same process. Thus, to account for the width variations, we introduce the effective stripe width $w_e$, corresponding to the detector segments most active in the resistive-state formation and photon detection, and we estimate $w_e$ to be 80 nm.

Our devices were mounted inside a cryostat on a cold base plate maintained at 4.2 K, wire-bonded to a 50-$\Omega$ microwave stripe line, and connected to the bias and output circuitry through a cryogenic bias-tee.[4] As optical excitation, we used 100-fs-wide pulses from a Ti:$Al_2O_3$ laser with a wavelength of 810 nm and a repetition rate of 82 MHz. The laser radiation power was attenuated down to a picowatt range using banks of neutral-density filters. Voltage pulses generated by our SSPD's were amplified directly by a room-temperature amplifier and fed to a synchronously triggered Tektronix 7404 single-shot digital oscilloscope, or they were counted by a fast electronic counter. The photon counter was used to determine the single-photon, two-photon, or multiphoton regimes of operation of our devices, as described in detail in Refs. 1 and 2. The amplifier and the oscilloscope had bandwidths of 0.01 to 12 GHz and 0 to 4 GHz, respectively. Thus, the ~100-ps real-time resolution of our entire readout system was determined mainly by the oscilloscope performance. On the other hand, digital averaging procedures of acquired pulses allowed us to achieve the relative-time resolution (e.g., delays between the photoresponse pulses generated under different photon excitations) of ~5 ps, due to extremely low intrinsic jitter in our measurement system.

Figure 92.33 presents the measured time delays in the photoresponse signal versus the number of absorbed photons, calculated as the photon flux density incident upon the meander multiplied by the device detection efficiency (DE).[2] The data are presented for two experimental bias conditions at $j/j_c = 0.85$ (open circles) and $j/j_c = 0.6$ (closed circles) and correspond to the SSPD single-photon and two-photon regimes of operations, respectively.

We will discuss the single-photon $\left(j/j_c = 0.85\right)$ regime first, remembering that for our $4 \times 4$-$\mu$m$^2$ device, DE for counting single, 810-nm photons at $j/j_c = 0.85$ is ~$10^{-3}$ (Ref. 2). We observe that for large absorbed photon fluxes (macroscopic number of photons per pulse) $t_d$ does not depend on the radiation flux. Clearly, this situation corresponds to the multi-hotspot-generation case presented in Fig. 92.32(a). We will use this condition as a reference and refer to it as $t_d = 0$. When the incident flux is decreased to about 10 absorbed photons/pulse, the arrivals of the photoresponse signals start to be time delayed with respect to the multiphoton response and $t_d$ increases. Subsequently, $t_d$ saturates when the flux density is decreased down to about $10^{-1}$ absorbed photons/pulse. In this case, we are in the single-photon counting mode [Fig. 92.32(c)]. Thereafter, the arrival of the photoresponse pulse is not further delayed in time scale even if we attenuate

the flux down to $10^{-3}$ absorbed photons/pulse. We interpret the measured time interval between the multiphoton and the single-photon responses, $\Delta t_d$ = 65±5 ps, as the time needed for supercurrent redistribution around a single, photon-created hotspot and subsequent formation of the resistive barrier for $j_{sw} > j_c$.

We repeated the same experiment, but with a significantly lower bias current applied to the detector (curve $j/j_c = 0.6$ in Fig. 92.33). In this case, according to Ref. 2, the probability of detecting a single, 810-nm photon by our $4 \times 4$-$\mu$m$^2$ device is negligibly small; thus, at least two photons are needed to generate the resistive response. As seen in Fig. 92.33, the observed behavior (closed circles) is very similar to that measured for $j/j_c = 0.85$; we can clearly identify the time-delay phenomenon and find $\Delta t_d$ = 70±5 ps. The main difference is that the observed photoresponse delay is now shifted into significantly higher levels of the incident photon flux. The value of $t_d$ starts to be nonzero for ~$10^3$ absorbed photons/pulse, and it flattens at ~10 absorbed photons/pulse. The latter value is very consistent with the two-photon detection mechanism.[1,2]

Finally, we can compare our experimental results with $t_d$ calculated for our experimental conditions, using Eq. (1) and $\tau_E \approx 10$ ps.[10] The current density in the sidewalks in the narrowest (most-active) segments of the meander can be calculated as $j_{sw} = j\left[w_e/\left(w_e - d_{hs}\right)\right]$, where $d_{hs} \approx 30$ nm is the diameter of the hotspot for 810-nm photons.[2] Thus, for the experimental $j/j_c = 0.6$ condition, $j_{sw}/j_c = 0.96$ and is subcritical in a single-hotspot regime. However, doubling the hotspot size[12] gives $j_{sw}/j_c = 1.28$, which is sufficient to generate a resistive barrier across our stripe. In a similar manner, when $j/j_c = 0.85$, $j_{sw}/j_c$ is supercritical and reaches 1.36 when the single hotspot is formed. Figure 92.34 shows the $t_d$ dependence on $j_{sw}/j_c$; the solid line represents the Tinkham model,[11] while the two closed circles refer to our measured $\Delta t_d$ values, corresponding to the $j_{sw}/j_c = 1.36$ and $j_{sw}/j_c = 1.28$ conditions, respectively. We note that our experimental values are reasonably close to the theoretical prediction, remembering that the Tinkham theory is applicable for clean superconductors, while our 10-nm-thick NbN films are in the dirty limit. In addition, the discrepancy can be related to the accuracy of our $w_e$ estimation.

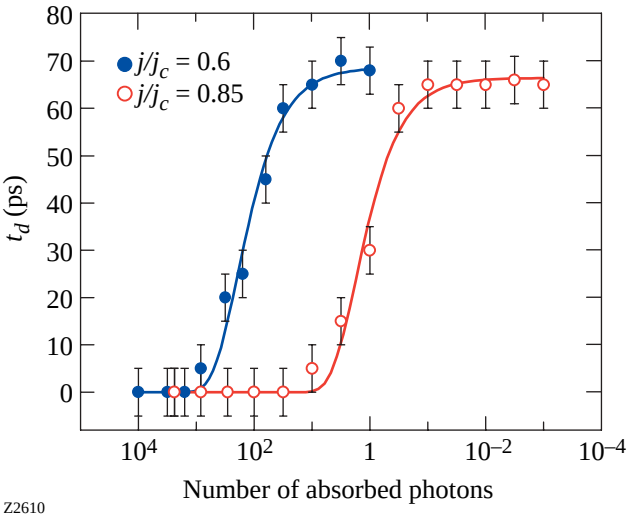


Figure 92.33
Experimental time delay $t_d$ of the resistive-state formation in a NbN superconducting stripe as a function of the incident absorbed photon flux density. Open circles correspond to $t_d$ measured when the stripe was biased with $j/j_c = 0.85$ (single-photon regime), and closed circles represent $j/j_c = 0.6$ and the two-photon regime. Solid lines are guides to the eye. The measurement error is ±5 ps.

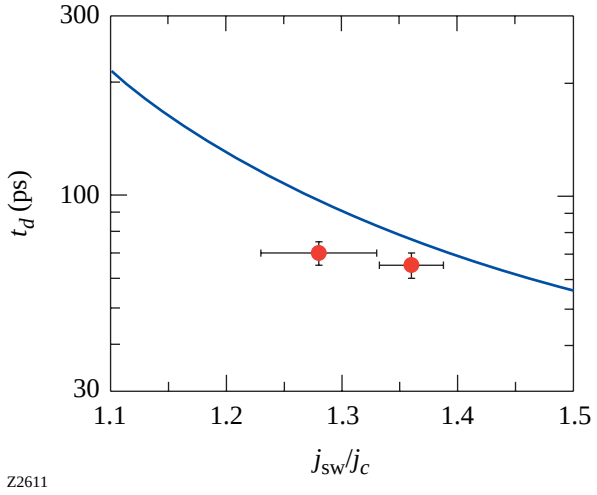


Figure 92.34
Time delay $t_d$ as a function of the normalized current in the sidewalks of the superconducting stripe $j_{sw}/j_c$. The two measured values of $\Delta t_d$ (solid circles) correspond to the single-hotspot and two-hotspot formation at $j_{sw}/j_c = 1.36$ and $j_{sw}/j_c = 1.28$, respectively. The solid line represents the theoretical prediction, calculated using Eq. (1), and the horizontal error bars are calculated for the hotspot-diameter variations of 30±1 nm.

In conclusion, we observed the time-delay phenomenon in the resistive-state response in ultrathin, submicrometer-width NbN superconducting stripes, excited by single optical photons. The observed phenomenon directly shows that the resistive state across an ultrathin, submicrometer-width superconducting stripe upon absorption of an optical photon is due to photon-induced hotspot formation and subsequent redistribution of the supercurrent into the sidewalks of the stripe. Our measurements agree well with a theoretical prediction based on the Tinkham model of the resistive-state formation in superconducting stripes under the supercurrent perturbation.[11]

## ACKNOWLEDGMENT

The authors thank Ken Wilsher for many valuable discussions. This work was funded by the NPTest, San Jose, CA. Additional support was provided by the US Air Force Office for Scientific Research Grant F49620-01-1-0463 (Rochester) and by the RFBR grant 02-02-16774 (Moscow).

## REFERENCES

1. G. N. Gol'tsman, O. Okunev, G. Chulkova, A. Lipatov, A. Semenov, K. Smirnov, B. Voronov, A. Dzardanov, C. Williams, and R. Sobolewski, Appl. Phys. Lett. **79**, 705 (2001).

2. A. Verevkin, J. Zhang, R. Sobolewski, A. Lipatov, O. Okunev, G. Chulkova, A. Korneev, K. Smirnov, G. N. Gol'tsman, and A. Semenov, Appl. Phys. Lett. **80**, 4687 (2002).

3. S. Somani, S. Kasapi, K. Wilsher, W. Lo, R. Sobolewski, and G. Gol'tsman, J. Vac. Sci. Technol. B, Microelectron. Nanometer Struct. **19**, 2766 (2001).

4. A. Verevkin, J. Zhang, W. Slysz, R. Sobolewski, A. Lipatov, O. Okunev, G. Chulkova, A. Korneev, and G. N. Gol'tsman, "Superconducting Single-Photon Detectors for GHz-Rate Free-Space Quantum Communications," to be published in SPIE's *Free-Space Laser Communication and Laser Imaging II*.

5. A. Verevkin, G. Gol'tsman, and R. Sobolewski, in *OPTO-Canada: SPIE Regional Meeting on Optoelectronic, Photonics, and Imaging* (SPIE, Bellingham, WA, 2002), Vol. TD01, pp. 39–40.

6. A. D. Semenov, G. N. Gol'tsman, and A. A. Korneev, Physica C **351**, 349 (2001).

7. A. M. Kadin and M. W. Johnson, Appl. Phys. Lett. **69**, 3938 (1996).

8. K. S. Il'in, I. I. Milostnaya, A. A. Verevkin, G. N. Gol'tsman, E. M. Gershenzon, and R. Sobolewski, Appl. Phys. Lett. **73**, 3938 (1998).

9. D. J. Frank *et al.*, Phys. Rev. Lett. **50**, 1611 (1983); D. J. Frank and M. Tinkham, Phys. Rev. B **28**, 5345 (1983).

10. K. S. Il'in, M. Lindgren, M. Currie, A. D. Semenov, G. N. Gol'tsman, R. Sobolewski, S. I. Cherednichenko, and E. M. Gershenzon, Appl. Phys. Lett. **76**, 2752 (2000).

11. M. Tinkham, *Introduction to Superconductivity*, 2nd ed., International Series in Pure and Applied Physics (McGraw-Hill, New York, 1996).

12. In a case where two hotspots are present in the film, we have taken the average effective size of the double hotspot across the cross section of the NbN stripe to be $\sqrt{2}d_{\mathrm{hs}}$ to take into account a possible overlap between the hotspots.

# LLE's Summer High School Research Program

During the summer of 2002, 15 students from Rochester-area high schools participated in the Laboratory for Laser Energetics' Summer High School Research Program. The goal of this program is to excite a group of high school students about careers in the areas of science and technology by exposing them to research in a state-of-the-art environment. Too often, students are exposed to "research" only through classroom laboratories, which have prescribed procedures and predictable results. In LLE's summer program, the students experience many of the trials, tribulations, and rewards of scientific research. By participating in research in a real environment, the students often become more excited about careers in science and technology. In addition, LLE gains from the contributions of the many highly talented students who are attracted to the program.

The students spent most of their time working on their individual research projects with members of LLE's technical staff. The projects were related to current research activities at LLE and covered a broad range of areas of interest including laser optics modeling, analysis of OMEGA implosion experiments, hydrodynamics modeling, cryogenic target physics and characterization, liquid crystal chemistry, thin-film deposition, and the development and control of laser fusion diagnostics (see Table 92.IV).

The students attended weekly seminars on technical topics associated with LLE's research. Topics this year included lasers, fusion, holographic optics, hydrodynamic stability, laboratory astrophysics, computer-controlled optics manufacturing, and microcontrollers and their applications. The students also received safety training, learned how to give scientific presentations, and were introduced to LLE's resources, especially the computational facilities.

The program culminated on 28 August with the "High School Student Summer Research Symposium," at which the students presented the results of their research to an audience including parents, teachers, and LLE staff. The students' written reports will be bound into a permanent record of their work that can be cited in scientific publications. These reports are available by contacting LLE.

One hundred forty-five high school students have now participated in the program since it began in 1989. This year's students were selected from approximately 50 applicants.

At the symposium, LLE presented its sixth annual William D. Ryan Inspirational Teacher Award to Mr. James Keefer, a physics and chemistry teacher at Brockport High School. This award includes a $1000 cash prize. Alumni of the Summer High School Research Program were asked to nominate teachers who played a major role in sparking their interest in science, mathematics, and/or technology. Mr. Keefer was nominated by Priya Rajasethupathy, a participant in the 2000 Summer Program. Priya credits Mr. Keefer with preparing her well for college and writes of her former teacher: "What impresses me most about Mr. Keefer is his teaching style, his ability to communicate with his students and captivate their interest." Mr. Jeff Brown, principal of Brockport High School, also had many words of high praise for Mr. Keefer. He noted that Mr. Keefer "is an exceptional teacher recognized by our students, faculty, administration, and community." He also said that Mr. Keefer "has some unique qualifications" as he is certified in five areas of science (earth science, chemistry, biology, physics, and general science).

Table 92.IV: High School Students and Projects—Summer 2002.

| Name | High School | Supervisor | Brief Project Title |
|---|---|---|---|
| Megan Alexander | Honeoye Falls–Lima | J. Zuegel/W. Seka | Picket Pulse Shaping with Phase and Amplitude Modulation in the Frequency Domain |
| Stefan Astheimer | Honeoye Falls–Lima | P. B. Radha | Estimation of Magnetic Fields in Direct-Drive Implosions |
| Christine Balonek | Byron–Bergen | K. Marshall | Optical Applications of Lyotropic Liquid Crystalline Polysaccarides |
| David Dingeldine | Churchville–Chili | J. Knauer | Plasma Energy Measurement with an Open-Cell Metal Foam |
| Sonya Dumanis | Harley School | V. Smalyuk | Structure of Shell Modulations Near Peak Compression of Spherical Implosions |
| Sid Ghosh | Pittsford–Mendon | P. Jaanimagi | Secondary Electrons from X-Ray Photocathodes |
| Kyle Gibney | Livonia | C. Stoeckl | Computer-Controlled Neutron Diagnostics |
| Sharon Jin | Victor | S. Craxton | A Ray-Tracing Model for Cryogenic Target Uniformity Characterization |
| Jue Liao | Brighton | R. Epstein | Rayleigh–Taylor Growth Rates for Arbitrary Density Profiles Calculated with a Variational Method |
| Christopher Moody | Spencerport | D. Harding | Characterization of the Absorption Spectrum of Deuterium for Infrared Wavelengths |
| Phoebe Rounds | Irondequoit | S. Craxton | Multiple-Tripler Broad-Bandwidth Frequency Conversion |
| Micah Sanders | Pittsford–Mendon | N. Bassett | Thin Film Characterization of $Al_2O_3$ Utilizing Reactive Pulsed dc Magnetron Sputtering |
| Gurshawn Singh | Rush–Henrietta | J. Marozas | 2-D Pulsed Laser Beam Modeling Using PROP |
| Archana Venkataraman | Brighton | F. Marshall | Characterization of Multilayer Diffractors for Framed Monochromatic Imaging |
| Joy Yuan | Pittsford–Mendon | M. Guardalben | Noncollinear Phase Matching in Optical Parametric Chirped-Pulse Amplification |

# FY02 Laser Facility Report

Increased user demand was met in FY02 by expanding the available shot time during select weeks. Ten weeks were extended to four shot days by shooting one 8-h day, two 12-h days, and one 16-h day. This adjustment raised the total executed shots by 11%—from 1289 in FY01 to 1428 in FY02 (see Table 92.V). Shaped-pulse cryogenic implosions highlighted the ongoing development of direct-drive cryogenic capability. A total of 21 spherical cryogenic $D_2$ targets were shot on OMEGA. Some of the cryogenic target shot time was devoted to characterization and system reliability improvements. Planar cryogenic target capability was also activated, and many shots were executed under LLE's Stockpile Stewardship Program (SSP) campaign. Highlights of other achievements and active projects as of the end of FY02 include the following:

- An IR streak camera with pulse-shape analysis software became a key operational tool to optimize pulse-shape performance. Combined with some changes to the control system for pulse-shape setup and upgrades to the regenerative oscillator hardware, the changes have resulted in dramatic improvements to delivered-pulse-shape performance.

- Infrared amplification occurs across a large variety of gain stages. By far, the highest gain stage is the regenerative (regen) amplifier, with $1 \times 10^5$ gain. One of the flash-lamp-pumped laser regens for OMEGA was replaced by a diode-pumped version that operates consistently without feedback stabilization. This diode-pumped laser improves pulse-shape performance. The remaining regens on OMEGA will be changed over to the new design in FY03.

- The distributed polarization rotator (DPR)—one of the key optics for beam smoothing on target—was modified for remote removal and reinstallation. The cassette-style removal system retracts the optic from the UV beamline into a protective housing. Having the capability to insert or remove these components improves flexibility for reconfiguring to indirect-drive setups. The full 60-beam complement of actuators will be completed early in FY03.

- The OMEGA laser is designed to provide a high degree of uniformity and flexibility in target illumination. The ability to impose a controlled assymmetric on-target irradiation pattern was developed and used extensively. This capability is used to benchmark multidimensional hydrodynamic simulations by imposing known nonuniform compression conditions on spherical targets. It is also used to modify laser-irradiation conditions for beam-to-beam x-ray yield balance.

- Modifications to the stage-A alignment sensors on OMEGA have streamlined an item of flexibility frequently exploited by LLE principal investigators. The backlighter driver alignment handoff to the OMEGA beamlines was re-engineered to expedite configuration setups that require the use of this source.

- Scientists and engineers from Lawrence Livermore National Laboratory along with LLE collaborators successfully implemented a green (second harmonic, 527 nm) target irradiation capability on one of the 60 OMEGA beams. This capability utilizes the existing OMEGA frequency-conversion crystals with the tripler detuned so that maximum 527-nm conversion is achieved.

- A revised set of direct-drive phase plates was designed and is being fabricated to further optimize irradiation uniformity for spherical implosions. These optics are going to be available in mid-FY03 and are expected to have improved smoothing characteristics in the mid-spatial-frequency range.

Table 92.V: The OMEGA target shot summary for FY02.

| Laboratory | Planned Number of Target Shots | Actual Number of Target Shots |
|---|---|---|
| LLE | 755 | 720 |
| LLNL* | 405 | 413 |
| LANL | 130 | 132 |
| SNL | 20 | 24 |
| NLUF | 120 | 118 |
| CEA | 20 | 19 |
| Total | 1450 | 1426 |
| | | |
| LLE ISE | | 306 |
| LLE SSP | | 204 |
| LLE RTI | | 66 |
| LLE LPI | | 44 |
| LLE Astro | | 46 |
| LLE Cryo | | 21 |
| LLE DD | | 18 |
| LLE PB | | 15 |
| LLE Total | | 720 |

*Includes ten in collaboration with LANL and seven with SNL.

# National Laser Users' Facility and External Users' Programs

During FY02, 698 target shots were taken on OMEGA for external users' experiments. This is the highest number of target shots ever taken by external users on OMEGA in a single year and represents a 16% increase in external user shots over FY01. The external user shots accounted for 49% of the total OMEGA target shots in FY02. External users' experiments were carried out by eight collaborative teams under the National Laser Users' Facility (NLUF) Program as well as collaborations led by scientists from Lawrence Livermore National Laboratory (LLNL), Los Alamos National Laboratory (LANL), Sandia National Laboratory (SNL), the Nuclear Weapons Effects Testing (NWET) Program, and the Commissariat à l'Énergie Atomique (CEA) of France.

**NLUF Programs**

FY02 was the second of a two-year period of performance for the eight NLUF programs approved for FY01–FY02 experiments. The eight NLUF campaigns received a total of 118 target shots on OMEGA in FY02.

The Department of Energy (DOE) issued solicitations in mid-FY02 for NLUF proposals to be carried out in FY03–FY04. DOE raised the NLUF funding allocation to $800,000 for FY03 and is expected to increase it to $1,000,000 for FY04 to accommodate the high level of interest shown in the use of OMEGA to carry out experiments of relevance to the National Nuclear Security Agency (NNSA) Stockpile Stewardship Program. NLUF participants use these funds to cover their costs for carrying out experiments on OMEGA. The participants do not pay the OMEGA operating costs for carrying out their experiments; the operation of OMEGA is funded by the DOE-LLE Cooperative Agreement.

A total of 13 NLUF proposals were submitted to DOE for consideration for FY03–FY04 support and OMEGA shot allocation. An independent DOE Technical Evaluation Panel comprised of Dr. Tina Back (LLNL), Dr. David Bradley (LLNL), Dr. David Montgomery (LANL), and Dr. Richard Olson (SNL) reviewed the proposals on 10 June 2002 and recommended that up to nine of the proposals be approved for partial funding and shot allocation during FY03–FY04. Table 92.VI lists the successful proposals.

**FY02 NLUF Experiments**

The eight NLUF experiments carried out in FY02 included the following:

*Atomic Physics of Hot, Ultradense Plasmas.*
Principal Investigators: C. F. Hooper, Jr. (University of Florida), D. A. Haynes (Fusion Technology Institute, University of Wisconsin), and collaborators from Los Alamos National Laboratory, the University of Wisconsin, and LLE.

The objective of this study is to produce hot (electron temperature $T_e > 1.5$ keV), dense (electron density $\sim 5 \times 10^{24}$ cm$^{-3}$) plasmas on OMEGA and to study these plasmas using x-ray spectroscopy. The focus of the work over the last two years has been on studying direct-drive implosions of CH shells filled with deuterium doped with Ar. A total of 11 shots were taken this year, and the results are currently being analyzed.

*Determination of Temperatures and Density Gradients in Implosion Cores of OMEGA Targets.*
Principal Investigators: R. C. Mancini (University of Nevada, Reno), J. A. Koch (LLNL), and collaborators from Prism Computational Sciences, LLE, LLNL, and Howard University.

The goal of this project is the spectroscopic determination of 1-D temperature and density gradients in implosion cores produced in OMEGA indirect-drive implosion experiments. The method is based on a novel self-consistent analysis of data from simultaneous x-ray line spectra and x-ray monochromatic images. This represents a significant advance on previous efforts of x-ray spectroscopy of implosion cores that relied solely on the analysis of space-integrated spectra to extract spatially averaged temperature and density in the core.

Targets consisted of Ar-doped, $D_2$-filled plastic shells placed inside Au hohlraums, and the targets were driven by 30 OMEGA UV beams. During FY02, the spectroscopic method

Table 92:VI: List of successful FY03–FY04 NLUF Proposals.

| Principal Investigator | Affiliation | Proposal Title |
|---|---|---|
| R. P. Drake *et al*. | University of Michigan | Experimental Astrophysics on the OMEGA Laser |
| B. B. Afeyan | Polymath Research, Inc. | Optical Mixing Controlled Stimulated Scattering Instabilities: Generating Electron Plasma Waves and Ion-Acoustic Waves to Suppress Backscattering Instabilities |
| R. D. Petrasso and C. K. Li | Massachusetts Institute of Technology | Time Evolution of Capsule $\rho R$ and Proton Emission Imaging of Core Structure |
| C. McKee *et al*. | University of California, Berkeley | OMEGA Laser Studies of the Interaction of Supernova Blast Waves with Interstellar Clouds |
| R. K. Fisher | General Atomics | High-Spatial-Resolution Neutron Imaging of Inertial Fusion Target Plasmas Using Neutron Bubble Detectors |
| M. Meyers *et al*. | University of California, San Diego | Dynamic Properties of Shock-Compressed Single Crystals by *in-situ* Dynamic X-Ray Diffraction |
| H. Baldis *et al.* | University of California, Davis | Studies of Ion-Acoustic Waves (IAW) Under Direct-Drive NIF Conditions |
| R. Mancini *et al*. | University of Nevada, Reno | Experimental and Modeling Studies of 2-D Core Gradients in OMEGA Implosions |
| R. Jeanloz | University of California, Berkeley | Recreating Planetary Core Conditions on OMEGA |

for core gradient determination was expanded in two ways. First, the original method based on the self-consistent analysis of Ar x-ray line spectra and Ar $He_\beta$ line monochromatic images (i.e., two criteria) was extended to a three-criteria (i.e., more-stringent) method based on the search for plasma gradients that yield the best fits to x-ray line spectra and the Ar $He_\beta$ and $Ly_\beta$ monochromatic emissivities. The spatial distribution of monochromatic emissivities is extracted via an Abel inversion of intensity lineouts from x-ray images. This multi-objective data analysis problem is efficiently solved with a niched Pareto genetic algorithm. The algorithm is general and can be applied to other cases of multi-objective data analysis as well. Second, an alternative technique to analyze the temperature gradient was developed. It is based on the fact that the local ratio (i.e., point-by-point in the plasma source) of $Ly_\beta$ to $He_\beta$ emissivities is a strong function of the temperature with a weak (residual) dependence on the density. As a result, temperature gradients can now be determined by two different techniques and cross-checked for consistency.

The MMI-2 x-ray imager for indirect-drive implosions was successfully fielded and tested. This new instrument uses a target-mounted pinhole array and a flat multilayer-mirror Bragg reflector to record numerous narrowband x-ray images spanning the 3- to 5-keV photon energy range (see Fig. 92.35). The pinhole diameters are 5 $\mu$m, and the spatial resolution is 10 $\mu$m.

Figure 92.36 shows typical data recorded by MMI-2. Each image spans ≈75 eV along the spectral axis. Groups of images can be combined to produce line-based images. Continuum-based images can also be extracted from the data. As a result, several line- and continuum-based images can now be recorded in the same shot. In particular, the problem of intensity

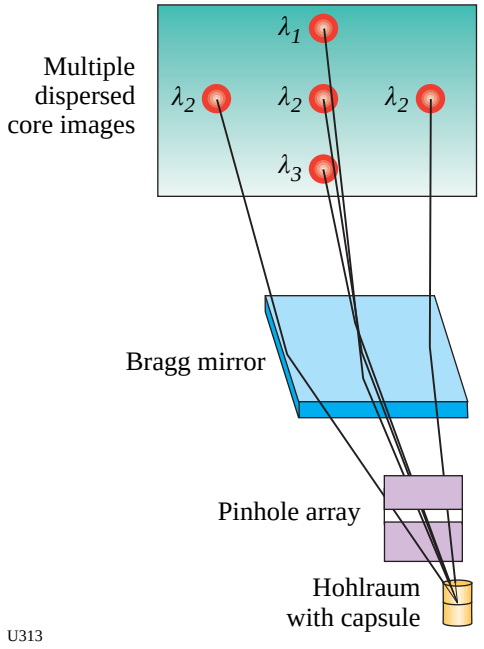


Figure 92.35
Schematic illustrating the concept of the MMI-2 x-ray imager. A target-mounted pinhole array provides numerous high-resolution, high-brightness x-ray images, and in combination with a multilayer Bragg mirror, it produces an array of quasi-monochromatic dispersed core images. This multispectral imaging technique is based on an LLE-developed technique.[1]

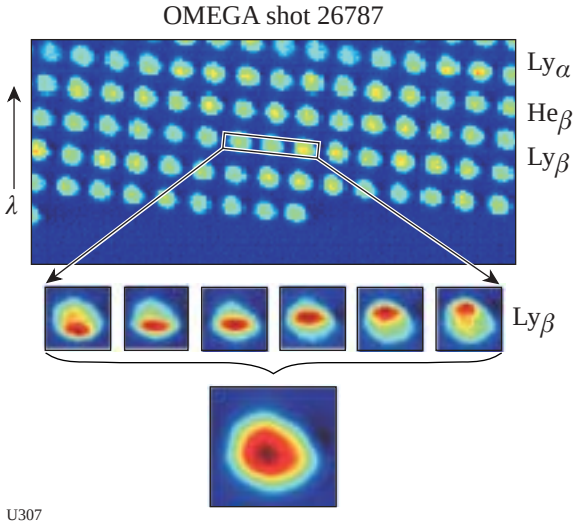


Figure 92.36
An array of implosion-core images recorded with MMI-2 in OMEGA shot 26787. Three Ar line transitions are indicated along the spectral dispersion axis: Ly$_\alpha$ (3.734 Å), He$_\beta$ (3.369 Å), and Ly$_\beta$ (3.151 Å). The subgroup of six images shows different portions of each image covered by the Ly$_\beta$ emission. This subgroup of images is used to produce the Ly$_\beta$-based image of the core shown at the bottom of the figure.

and structure of continuum-photon contribution to line-based images can now be addressed with greater accuracy. An interactive data language (IDL)–based code was written to process MMI-2 data, combine subgroups of images, and produce different types of x-ray core images.

*Studies of the Fundamental Properties of High-Energy Density Plasmas.*
Principal Investigator: R. D. Petrasso (MIT Plasma Science and Fusion Center) and collaborators from MIT, LLE, LLNL, and SUNY Geneseo.

Proper assembly of capsule mass in inertial confinement fusion (ICF) implosions is of fundamental importance for achieving ignition,[2–4] and experimental information about implosion dynamics is crucial both for understanding how assembly occurs and for validating numerical simulations. Without carefully tailored assembly of the fuel, hot-spot ignition planned for the National Ignition Facility (NIF)[2–5] and the Laser Megajoule Facility (LMJ)[6] will fail. Hot-spot ignition relies on shock coalescence to "ignite" the hot spot, followed by burn of the compressed "shell" material (compressive burn). The relationship between these events must be understood to ensure the success of ICF ignition.

In the last year, the MIT/LLE collaboration, as part of the MIT NLUF program, obtained gated measurements of areal density ($\rho R$) at pivotal moments in the target's evolution: first at shock coalescence and then 400 ps later during compressive burn. These measurements were accomplished through the use of 14.7-MeV protons generated by the fusion of the fuel constituents—deuterium (D) and helium ($^3$He)—in imploding capsules with 24-$\mu$m-thick plastic (CH) shells.[7,8] An accurate determination of $\rho R$ evolution and asymmetry is made by measuring the proton energy downshift at different times and in many different directions.

Earlier measurements of $\rho R$ utilizing primary 14.7-MeV protons[7–9] and secondary protons[10] concentrated on properties and dynamics during compressive burn for implosions of capsules with 20-$\mu$m-thick CH shells. These studies included $\rho R$ asymmetries,[9–11] fuel–shell mix,[12–15] and the effects of beam smoothing upon fuel $\rho R$.[9,12,16] In addition, x-ray absorption techniques[17] have been used to study aspects of $\rho R$ modulations at peak compression and during decompression.

Direct-drive implosions were conducted on OMEGA, with 60 beams of frequency-tripled (351-nm) UV light in a 1-ns square pulse and a total energy of ~21 kJ.[18] Full smoothing of

the laser beams was used,[12] and beam-to-beam energy imbalance was typically ≤5% rms. Two types of hydrodynamically similar capsules were used, all with a nominal diameter of 940 μm and a shell thickness of 24 μm. CH-shell capsules were filled with approximately 6 atm of $D_2$ and 12 atm of $^3$He. Capsules with shells of CD (or 1 μm of CD inside of 23 μm of CH) were filled with approximately 20 atm of $^3$He. The principal diagnostics for this work were high-resolution, charged-particle spectrometers simultaneously viewing each implosion from different directions (the spectrometers and their properties are described in Ref. 8). In addition, the neutron temporal diagnostic (NTD) measured the D fusion burn histories.[19]

The following reactions occur in imploding capsules fueled with D and $^3$He:

$$\mathrm{D} + \mathrm{D} \rightarrow \mathrm{p}(3.0\ \mathrm{MeV}) + \mathrm{T}(1.0\ \mathrm{MeV}), \tag{1}$$

$$\mathrm{D} + \mathrm{D} \rightarrow \mathrm{n}(2.5\ \mathrm{MeV}) + {}^3\mathrm{He}(0.8\ \mathrm{MeV}), \tag{2}$$

$$\mathrm{D} + {}^3\mathrm{He} \rightarrow \mathrm{p}(14.7\ \mathrm{MeV}) + \alpha(3.6\ \mathrm{MeV}). \tag{3}$$

This analysis uses the high-energy proton of Reaction (3) because it can easily penetrate the larger $\rho R$ during compressive burn while, in contrast, the 3.0-MeV protons of Reaction (1) are ranged out. Figure 92.37 shows proton spectra obtained simultaneously at five different viewing angles for shot 24811. In each spectrum, two distinct peaks are clearly evident. The narrow, higher-energy peak is associated with burn of ~40-ps duration at shock coalescence, while the broader, lower-energy peak is associated with the ~150-ps compressive burn that occurs about 400 ps after the shock.[20] For each of the two peaks in each spectrum, the average energy downshift of the 14.7-MeV protons was evaluated and is shown in Fig. 92.38 along with data from several other shots. Through the use of plasma stopping power calculations,[21] these energy downshifts are related to the capsule $\rho R$ (Fig. 92.38 and Table 92.VII). The capsule $\rho R$ at shock coalescence, which occurs 1.7±0.1 ns after the beginning of the 1-ns laser pulse, is ~13.0±2.5 mg/cm$^2$. During compressive burn, the average $\rho R$ increases to 70±8 mg/cm$^2$. Since the temperature of the shell is at or below 1 keV at both shock and compression times, and since nearly all energy loss occurs through the shell,[7,10] these $\rho R$ determinations are insensitive to exact values of the evolving temperature and density.[21] Table 92.VII summarizes the data of Fig. 92.38, which also show that asymmetries as large as 30 mg/cm$^2$ in areal density exist during compressive burn in these implosions. This effect has been reported for capsules with 20-μm-thick shells[9,10] and for cryogenic capsules.[10]

The ion temperature at shock burn can be measured from the spectra. As shown in Fig. 92.39, the shock peak is well fit by a Gaussian. After accounting for the effects of the instrument response,[7,8] a Doppler-derived ion temperature of 6±1 keV is obtained. This temperature is higher than the neutron-derived Doppler-width temperature characterizing the compressive burn, which is about 3 keV. This method of temperature determination from the width of the 14.7-MeV proton spectrum has been previously used for thin-shell, high-temperature implosions.[7] At shock burn (for thick-shell implosions), the shell is relatively "thin," the shock-induced ion temperature is relatively high, and the duration (~40 ps) is sufficiently short that little evolution in $\rho R$ occurs. In contrast, the compression

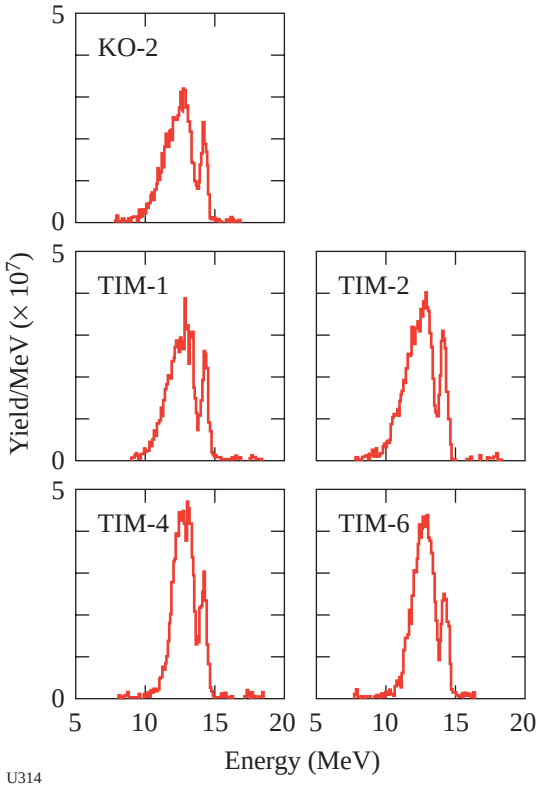


Figure 92.37
Spectra of high-energy protons generated from the fusion of D and $^3$He in an imploding ICF capsule (shot 24811). The spectrometers viewed the implosion from five different directions; each plot is identified by the OMEGA port used.[8] The narrow high-energy peak is associated with shock-coalescence burn; the broad low-energy peak is associated with compressive burn.

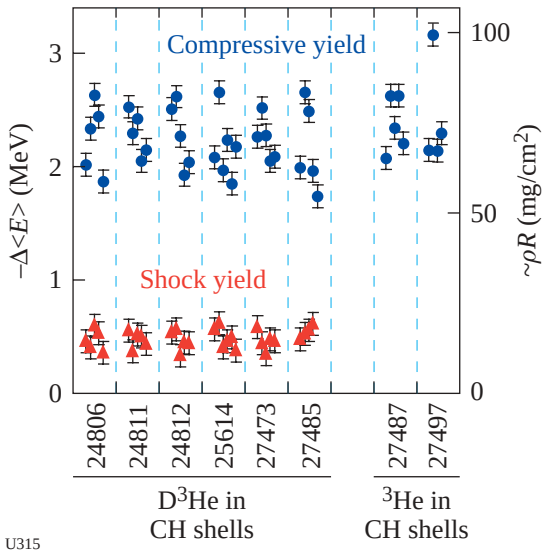


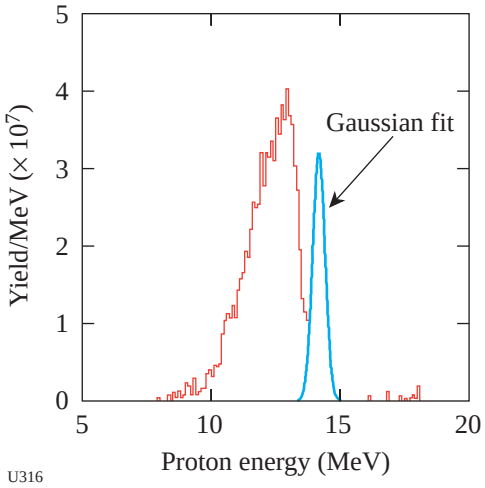


Figure 92.38
The average energy downshifts (from 14.7 MeV) for the shock and compression burn peaks of each spectrum from shot 24811 (as shown in Fig. 92.37) and from several others. From plasma stopping power calculations,[21] values of $\langle \rho R \rangle$ can be associated with the plotted values of $\Delta E_p$, and the right-hand vertical axis scale is meant to show the approximate correspondence (Table 92.VII lists more-exact values for averages over groups of shots).

Figure 92.39
A shock-induced ion temperature can be determined by fitting a Gaussian to the shock peak, correcting for the instrument response, and assuming Doppler broadening. For this spectrum the result is 6.8 keV, and the mean for all spectra from this shot (24811) is 6 keV with a standard deviation of 1 keV.

Table 92.VII: Values of $\langle \rho R \rangle$ inferred from measured $D^3He$ proton energy losses (calculated with the slowing-down formalism of Ref. 21, using energies averaged over all available spectra for each shot). For capsules with $D^3He$ fuel and CH shells, it was assumed that the slowing was dominated by CH at $T_e \leq 1$ keV and $\rho = 2$ g/cm$^3$ at shock coalescence or 20 g/cm$^3$ at compression burn. For capsules with $^3He$ fuel in CD shells, which produce no shock yield, it was assumed that the slowing was dominated by CD at $T_e \leq 1$ keV and $\rho = 20$ g/cm$^3$. The "±" refers not to measurement uncertainties but to the standard deviation about the mean of individual measurements for each shot.

| Shot | Fuel | Shell | $\langle \rho R \rangle_{shock}$ (mg/cm$^2$) | $\langle \rho R \rangle_{comp}$ (mg/cm$^2$) |
|---|---|---|---|---|
| 24086 | 18 atm $D^3He$ | 24 $\mu$m CH | 13.2±2.6 | 70.6±9.7 |
| 24811 | 18 atm $D^3He$ | 24 $\mu$m CH | 13.3±2.0 | 71.6±6.1 |
| 24812 | 18 atm $D^3He$ | 24 $\mu$m CH | 13.0±2.5 | 71.1±9.2 |
| 25614 | 18 atm $D^3He$ | 24 $\mu$m CH | 13.7±2.6 | 67.6±8.7 |
| 27473 | 18 atm $D^3He$ | 24 $\mu$m CH | 12.9±2.3 | 70.1±5.8 |
| 27485 | 18 atm $D^3He$ | 24 $\mu$m CH | 15.2±1.6 | 67.8±12.1 |
| 27474 | 20 atm $^3He$ | 24 $\mu$m CD | — | 79.5±8.3 |
| 27479 | 20 atm $^3He$ | 24 $\mu$m CD | — | 81.5±16.4 |

burn peak for the protons (as noted previously[7]) is far wider than the Doppler width and, the effects of measured asymmetry[7–9] and geometry[8] notwithstanding, largely reflects $\rho R$ evolution over the compressive burn (~150 ps).

To validate the interpretation that the high-energy peak (Fig. 92.37) is due to shock coalescence, and to explore other important aspects of implosion physics, a second series of implosions were performed using a hydrodynamically similar capsule with 20 atm of $^3$He in a 24-$\mu$m-thick CD shell. Spectra from these implosions [see the example in Fig. 92.40(b)] show a single compression peak downshifted in energy by about the same amount as measured in the first series of experiments [see Fig. 92.40(a)]. Notably absent, however, is the shock peak in Fig. 92.40(a) that occurs between 14 and 15 MeV. This means that no D from the shell has mixed into the central, high-temperature region at shock time.[22] Conversely, by the time of compressive burn, mixing of the CD shell with the $^3$He must have occurred (Fig. 92.40) in order for D$^3$He reactions to be present (see Refs. 12–15 for more discussion of mix).

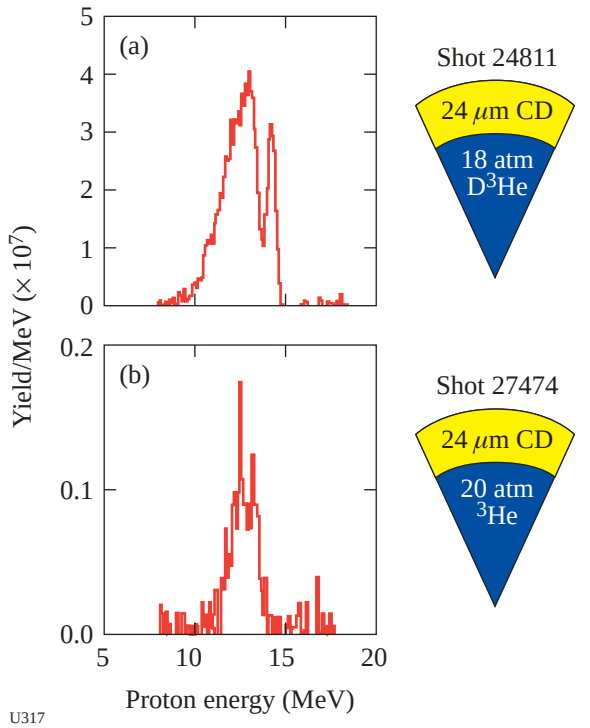


Figure 92.40
The shock-induced burn that is present in plot (a) is absent when the fuel is changed to pure $^3$He within a CD shell [plot (b)], although the compressive burn is still present because of fuel–shell mix. Besides validating the identification of the shock-induced peak, these data demonstrate the absence of fuel–shell mix in the central regions of the capsule at shock coalescence.

The spectrum of Fig. 92.40(b) can also be directly interpreted to mean that, at least for these implosions, the shell is not riddled with holes during compressive burn even though low-mode asymmetries exist (Fig. 92.38). If there were holes, there would be a high-energy peak in Fig. 92.40(b). This issue is important since concern exists as to whether shell breakup, as a consequence of Rayleigh–Taylor instability, occurs prior to burn propagation and ignition, thereby quenching ignition.

To improve the understanding of the physical processes and to test the validity of 1-D hydrodynamic simulations in realistic circumstances, we show a comparison of simulated[23] and experimental charged-particle spectra in Fig. 92.41. The basic structure of the experimental data is reproduced reasonably well by the simulation. Of particular relevance is the comparison at shock coalescence since, as experimentally demonstrated, the effects of mix are minimal and 1-D simulations should be at their most accurate because they do not include mix effects. In this context, the ratio of experimental yield to theoretical yield [so called yield-over-clean (YOC)] is about 60%; the predicted $\rho R$ is 10 mg/cm$^2$ while the experimental value is 13 mg/cm$^2$; the predicted shock temperature is 8 keV, while the measurement is 6±1 keV. It is also noteworthy that the predicted interval between shock and compression burn is 500 ps, while the measured interval is ~400 ps. Since shock timing and coalescence are critical to ignition at the NIF and the LMJ,[2–6] experiments to test the limits of validity of ignition simulation codes should be helpful to this endeavor. In addition, it seems entirely plausible that similar measurements could be made at the NIF at various phases in the development and testing of ignition capsules.

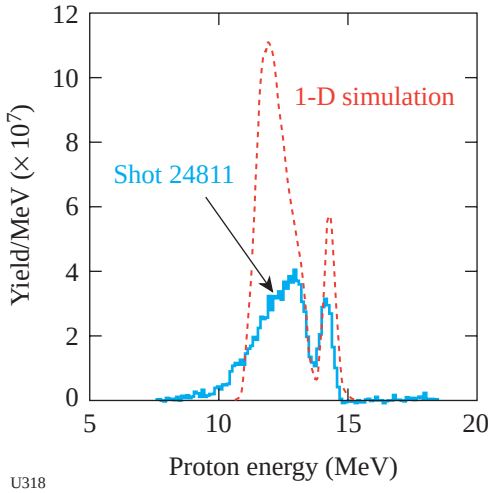


Figure 92.41
A comparison of 1-D simulation to data from shot 24811.

In summary, the first measurements of $\rho R$ evolution occurring in ICF implosions were conducted in the course of this past year's work on this program. In the 400-ps interval between shock coalescence and compression burn, the azimuthally averaged $\rho R$ changed from 13.0±2.5 to 70±8 mg/cm$^2$. The experiments demonstrated that fuel–shell mix has not occurred in the central regions of the imploding capsule at shock coalescence, and that the shock-induced temperature is about 6 keV. As mix is inconsequential at this stage of the implosion, these and other measured parameters offer a sensitive test of 1-D shock physics simulations. The experiments further demonstrated that, at least for these types of implosions, gaps and holes do not riddle the shell at compression burn.

Several intriguing avenues exist for advancing these measurements and improving the understanding of implosion dynamics. As $\rho R$ is sufficiently small at shock coalescence, 3.0-MeV protons from Reaction (1) will readily penetrate the shell and lead, in principle, to an even more accurate measurement of the shell $\rho R$ at that instant. Such experiments, as well as higher-accuracy spectrometers for $D^3He$ fusion reactions, are being planned. With more-accurate $\rho R$ measurements at shock coalescence, studies will be undertaken to establish whether $\rho R$ asymmetries exist at that time, and whether these asymmetries persist and amplify through the compression burn phase,[10,11] thereby accounting for the notable asymmetries that have been measured at that critical stage.

*High-Spatial-Resolution Neutron Imaging of Inertial Fusion Target Plasmas Using Bubble Neutron Detectors.*
Principal Investigator: R. K. Fisher (General Atomics) and collaborators from LLE, CEA, and LLNL.

Bubble detectors that can detect neutrons with a spatial resolution of 5 to 30 $\mu$m are a promising approach to high-resolution imaging of NIF target plasmas. Gel bubble detectors were used in successful proof-of-principle imaging experiments on OMEGA. The results were presented in an invited talk at the October 2001 Meeting of the Division of Plasma Physics of the American Physical Society and published in Physics of Plasmas.[24]

Until recently, bubble detectors appeared to be the only approach capable of achieving neutron images of NIF targets with the desired 5-$\mu$m spatial resolution in the target plane. In 2001, however, NIF reduced the required standoff distance from the target, so that diagnostic components can now be placed as close as 10 cm to the target plasma. This will allow neutron imaging with higher magnification and may make it possible to obtain 5-$\mu$m-resolution images on the NIF using deuterated scintillators.

Since gel detectors (which consist of ~10-$\mu$m-diam drops of bubble detector liquid suspended in an inactive support gel that occupies ~99% of the detector volume) are easy to use, they were chosen for the initial tests on OMEGA. The bubbles could be photographed several hours after the neutron exposure. Imaging NIF target plasmas at neutron yields of $10^{15}$ will require a higher-detection-efficiency detector. A liquid bubble chamber detector should result in an ~1000-times-higher neutron detection efficiency, which is comparable to that possible using scintillation detectors.

A pressure-cycled liquid bubble detector will require a light-scattering system to record the bubble locations a few microseconds after neutron exposure, when the bubbles have grown to be ~10 $\mu$m in diameter. The next major task planned under this grant will be to perform experimental tests to determine how accurately the spatial distribution of the bubble density can be measured under the conditions expected in the NIF. The bubble density will be large enough to produce significant overlap in the two-dimensional images, so we will need to be able to measure bubbles behind bubbles. One of the goals of these tests is to determine if a simple light-transmission approach is feasible. One of the concerns at very high bubble densities is that light scattered out of the path can be rescattered back into the transmitted light path by bubbles in neighboring paths.

*Examination of the "Cone-in-Shell" Target Compression Concept for Asymmetric Fast Ignition.*[*]
Principal Investigators: R. B. Stephens (General Atomics) and collaborators from LLNL and the Institute of Laser Engineering (ILE), Osaka University, Osaka, Japan.

Investigation of the compression hydrodynamics of fast-ignition targets continued in FY02 with several shots taken on "cone-in-shell" indirect-drive targets. The results from these experiments showed that while the hydrodynamic codes used to design these targets captured the gross dynamics well, there were details of the experiment that were not predicted by the code calculations.

[*]This work was performed under the auspices of the U.S. Department of Energy under Contract No. DE-FG03-00SF2229, by the University of California, Lawrence Livermore National Laboratory under Contract No. W-7405-ENG-48, and with the additional corporate support of General Atomics.

The separation of compression and ignition in the fast-ignition (FI) concept[25] requires a new approach to target design. The strict symmetry and smoothness requirements of a target compressed to generate and enclose an ignition spark by dense, cold fuel are replaced by a much more complex set of considerations. The fusion burn is optimized by creation of a uniformly dense fuel mass. The symmetry of that mass is relatively unimportant, but its surface must be pure DT and accessible to an ignition beam. The ignition energy must be delivered by a short-pulse laser, but the compression drive can be accomplished by any means—laser (direct and indirect drive), heavy ion beam, or *z*-pinch.

S. Hatchett (LLNL) designed an indirect-drive target based on the cone-in-shell FI target concept[26] [Fig. 92.42(a)]: A hollow cone is inserted in the side of the shell to provide a protected line of sight to the assembled fuel mass. Modeling suggests that the presence of the cone substantially changes the target's implosion dynamics [Fig. 92.42(b)]; surprisingly, one should achieve the most-compact target with a deliberately asymmetric drive [Fig. 92.42(c)]. The modeling might not properly capture details of the flow as the shell slides down along the cone surface; there is a concern that high-*Z* material from the cone might mix into the assembled fuel mass, thereby hindering ignition. This model was tested on a scale-1 hohlraum at OMEGA. Each collapse was radiographed with an x-ray framing camera, which took a sequence of 16 x-radiographs (Fig. 92.43). With this information it was possible to determine the implosion velocity and diameter, density, and symmetry at stagnation. X-ray images were taken alternately through different filters to identify any gold contamination in the assembled fuel. The experimental radiographs were very similar to the simulations; apparently the effect of the inserted cone was well described by *LASNEX* modeling, and both the shell and the drive were smooth enough that compression instabilities had minimal effect. As predicted, it was found that an asymmetric drive does seem to result in a more-compact target, but that that configuration also generates a gas flow that blows out the tip of the cone just about at the stagnation point. There were subtle differences between simulation and experiment.

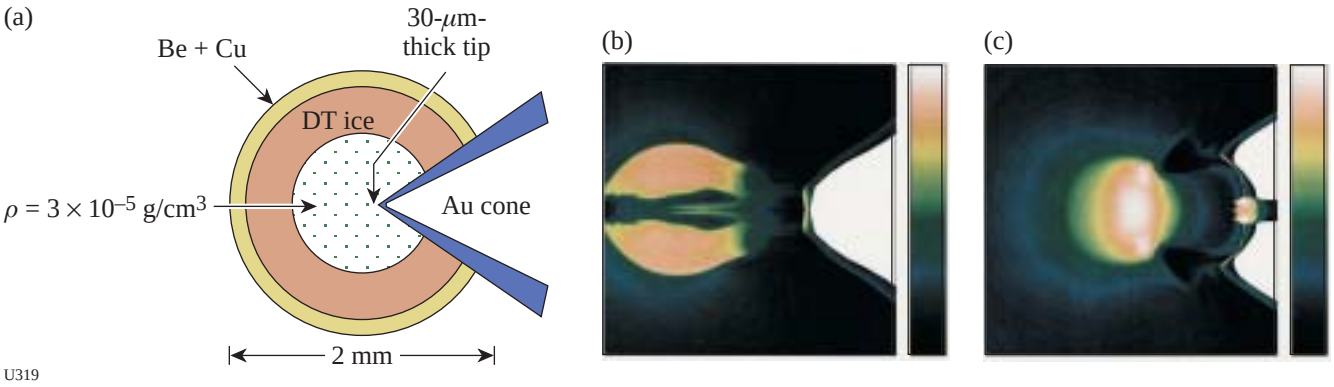


Figure 92.42
(a) Cross section of a FI cryo target designed to implode to $\rho R \sim 2$ g/cm$^2$ when driven by a 190-eV hohlraum; (b) density cross section of target at stagnation when driven symmetrically; and (c) density cross section when drive is 10% hotter on the side away from the cone.

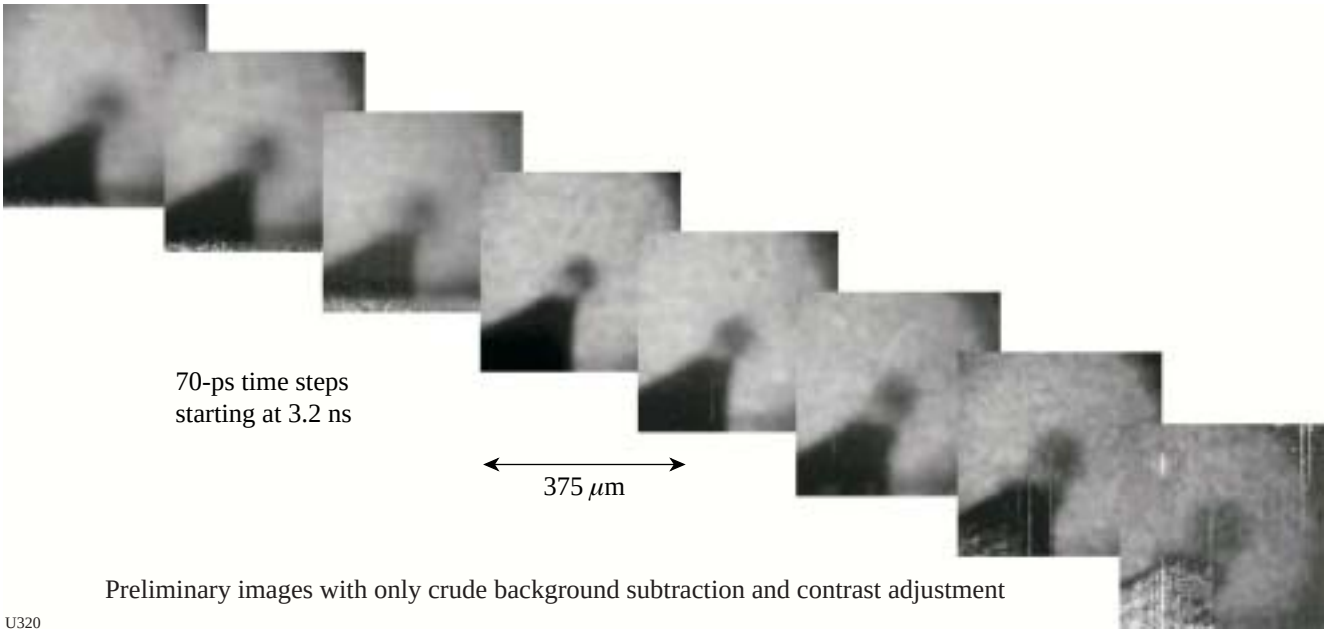


Figure 92.43
Eight of a series of 16 x-radiographs taken during a test of the cone-in-shell target design on OMEGA. The frames are 70 ps apart.

*Supenova Hydrodynamics on the OMEGA Laser.*
Principal Investigators: R. Paul Drake (University of Michigan), B. Remington (Center for Laser Astrophysics-ILSA, LLNL), and collaborators from LLNL, CEA Saclary (France), LLE, LANL, University of Arizona, University of Colorado, University of Chicago, SUNY Stony Brook, Naval Research Laboratory, and Eastern Michigan University.

The fundamental motivation for this work is that supernovae are not well understood. Recent observations have clarified the depth of this ignorance by producing observed phenomena that current theory and computer simulations cannot reproduce. Such theories and simulations involve, however, a number of physical mechanisms that have never been studied in isolation. During FY02 experiments were performed under this NLUF Program in compressible hydrodynamics and radiation hydrodynamics, relevant to supernovae and supernova remnants. These experiments produce phenomena in the laboratory that are believed, based on simulations, to be important to astrophysics but that have not been directly observed in either the laboratory or an astrophysical system. The experiments were focused on the scaling of an astrophysically relevant, radiative-precursor shock, preparations for studies of collapsing radiative shocks, and the multimode behavior and onset of turbulence in three-dimensional, deeply nonlinear evolution of the Rayleigh–Taylor (RT) instability at a decelerating, embedded interface. These experiments required strong compression and decompression, strong shocks (Mach ~10 or greater), flexible geometries, and very smooth laser beams, which means that the 60-beam OMEGA laser is the only facility capable of carrying out this program.

The experiments benefited from a strong collaborative effort that coupled a core experimental team to theoretical groups at several institutions. This enabled the development of experimental designs through advance simulations and the comparison of the results of the experiments to simulations by more than one code. A standardized approach to the experiments was also developed, enabling the pursuit of more than one experiment simultaneously, and thus the exploitation of the extensive theoretical capabilities of this collaboration. These experiments are sufficiently complex yet diagnosable, so they are excellent for verification and validation (V&V) of complex computer codes, including those produced by the Advanced Scientific Computing Initiative (ASCI) Alliance Center at the University of Chicago. This program is also a

critical stepping stone toward the use of the National Ignition Facility (NIF) both for fundamental astrophysics and as a critical component of ASCI V&V.

The supernova hydrodynamics experiments conducted in FY02 included the following:

*a. Radiative Precursor Shocks:* The scaling of radiative precursor shocks was investigated. These experiments involved the initial acceleration of a block of material to high velocity. The block of material then drove a shock wave through low-density foam at approximately 100 km/s, which was fast enough to produce a radiative precursor. The precursor is strongly sensitive to the shock velocity, so it was possible to control it by varying the laser energy. Figure 92.44 shows a photograph of a target used for experiments on OMEGA. Up to ten laser beams struck the front surface of this target, delivering several kJ of energy to an 800-$\mu$m-diam spot in a 1-ns pulse. The laser irradiation shocked and accelerated a 60-$\mu$m-thick plastic layer that crossed a 160-$\mu$m vacuum gap to impact the low-density foam, usually of density 0.01 g/cm$^3$.

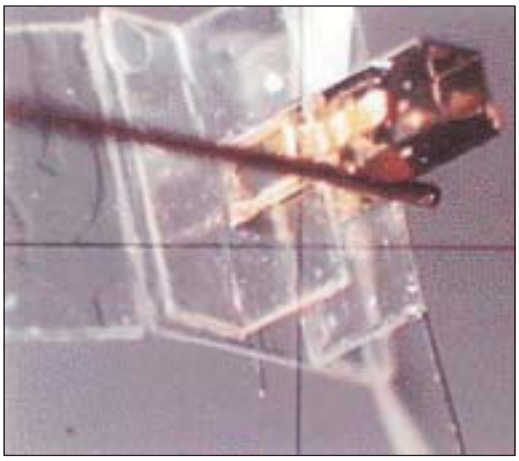

U321

Figure 92.44
An image of the target for the radiative precursor experiments. The laser beams approach from the left, driving a shock wave through the foam contained in the rectangular structure.

The structure of the precursor was investigated using absorption spectroscopy. Additional laser beams irradiated a thulium backlighter plate, permitting an imaging crystal spectrometer to obtain absorption spectra like those shown in Fig. 92.45. Absorption lines were detected from up to six different ionization states. The lines from higher ionization states appear at higher temperatures. From the entire spectrum, one could determine the location of the shock, the temperature of the shocked material, and the temperature profile in the radiative precursor, with the help of the OPAL[27] atomic code. It was observed that the precursor became longer as the laser drive energy increased, and that its behavior was consistent with a simple model of the threshold velocity for the production of a precursor. A paper based on these data was recently published in Physical Review Letters.[28] These experiments are now entering an analysis and writing phase. In addition, it is anticipated that such experiments will provide quality benchmark cases for astrophysical modeling. Participants in such comparisons will include the University of Maryland and the ASCI Flash Center at the University of Chicago.

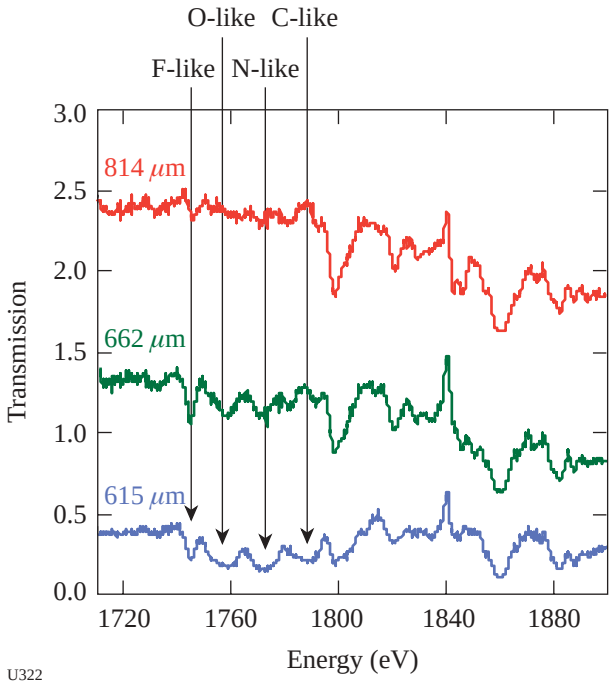


U322

Figure 92.45
Absorption spectra at three locations, showing the spatial development of four of the absorption lines. The spectra are offset vertically for clarity.

*b. Radiative Shocks:* Astrophysical shocks, when they become cool enough, enter a radiatively collapsing phase in which their density can increase several orders of magnitude. All supernova remnants eventually pass through this phase, and such shocks arise in a number of other contexts. This team's work with radiative-precursor shocks in foams represented a first step into radiative hydrodynamics. With the adoption of gas targets, however, shocks can be produced on OMEGA that

radiatively collapse. Several OMEGA shots were devoted to a preliminary attempt at such an experiment during FY02. They used only radiography as a diagnostic. Figure 92.46 shows the data that were obtained on the first attmpt. The overlaid profile shows the average of a 290-$\mu$m-high horizontal strip through the unobstructed portion of the image. One can clearly see the absorption feature due to the shock. Its position confirms that the shock velocity is well above 100 km/s. The laser and diagnostic settings were optimized for other experiments on this day, causing significant motional blurring (and weakening the absorption feature). Much better data can and will be obtained in future experiments. Such experiments will occupy approximately half of the target shots planned for the next year under this NLUF program.

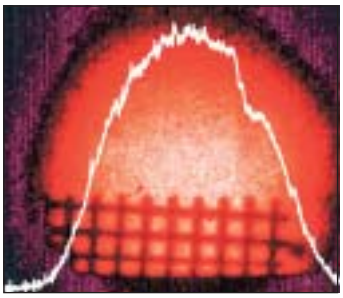
U310

Figure 92.46
Image and profile from a first attempt to produce a collapsing radiative shock. The notch in the profile toward the right is produced by the shocked gas.

*c. Multimode Rayleigh–Taylor (RT) Instability at a Decelerating, Embedded Interface:* It is fruitful to examine multimode systems because (a) the actual stellar explosions involve many modes and (b) the growth of multimode structures is a more-severe test of simulations. During FY02 data were obtained that showed the time evolution of the structures produced from initial conditions including one mode, two modes, and eight modes. The perturbations were designed to keep the global peak-to-valley amplitude constant at 5 $\mu$m as the number of modes changed. Figure 92.47 shows some data that were obtained using a two-mode perturbation, and Fig. 92.48 shows some data for an eight-mode perturbation. At earlier times, the multimode data show articulated spikes. Later, as in these figures, they show the emergence of large-scale features. Additional data are needed and will be obtained soon. The emergence of the large-scale features will be compared with theories of bubble merger. The effect of the number of modes on the width of the "mix region" will also be examined.

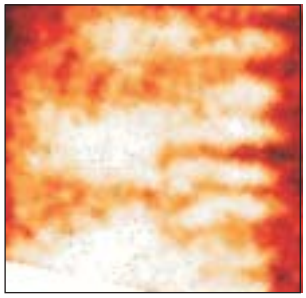
U323

Figure 92.47
Structures developed at 26 ns from a two-mode perturbation.

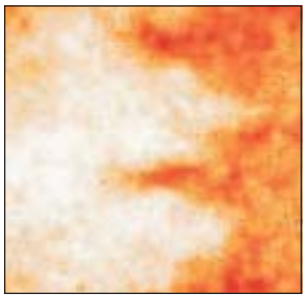
U324

Figure 92.48
Structures developed at 26 ns from an eight-mode perturbation.

*d. Onset of Turbulence in RT Instability at a Decelerating, Embedded Interface:* Based on a scaling analysis, it is believed that it will be possible to observe the transition to a turbulent state in the evolution of RT that develops from a 3-D initial condition. Figure 92.49 shows a radiograph of the structures produced from an initial 3-D perturbation that included a single mode with 71-$\mu$m wavelength and noise at much shorter wavelengths introduced when the (50-mg/cc) foam was machined. By this time, the unstable fingers have developed significant modal structure and have moved forward and overtaken the shock. Earlier, the fingers have a simpler spectral structure and remain well behind the shock. Later, the ability to distinguish the fingers is lost perhaps due to rapid diffusion caused by turbulence. Continuations of these experiments will determine whether, in fact, the onset of turbulence is being observed, and further analysis will evaluate the implications for astrophysics. Several publications based on this work have appeared in print during the last year.[29–31] One additional manuscript has been submitted for publication.[32]

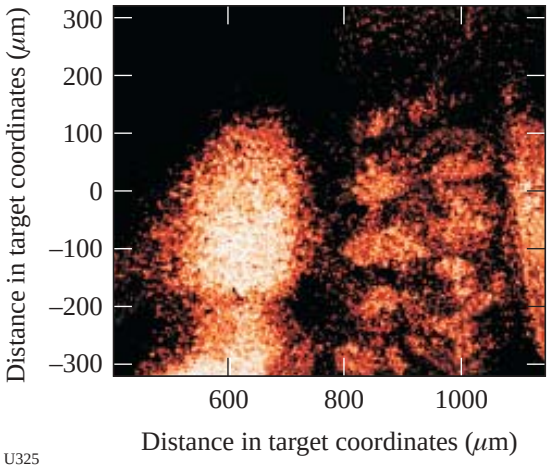


Figure 92.49
An experiment with a 3-D initial single-mode perturbation produced these structures 17 ns into the experiment.

*Studies of the Dynamic Properties of Shock-Compressed FCC Crystals by* In-Situ *Dynamic X-Ray Diffraction.*
Principal Investigators: H. Baldis (University of California at Davis), D. Kalantar (LLNL), and collaborators from LLNL, LLE, the University of California at San Diego, University of Oxford, and LANL.

This experiment uses time-resolved dynamic x-ray diffraction to investigate the response of a lattice under shock compression. Over the last two years this work included studies of shocked single-crystal Si with peak pressures ranging from <100 kbar to 200 kbar, experiments on single-crystal Cu[32] to study the dislocation density in the post-shocked material (these studies included recovery of shocked samples) at pressures ranging from 100 to 600 kbar, and investigations of deformation substructure in Cu.

Major accomplishments during the reporting period include the following:

- Implementation of multi-target shots. In several series of shots during this year, diffraction targets, VISAR wave profile targets, and shock-recovery targets were simultaneously fielded on shots. This approach greatly increases the effectiveness of target shots providing triple the data per shot than would have been available if the three experiments were individually shot.[33]
- A pressure scan for Si was completed to record multiple lattice planes.
- The wave profile of shocked Si was recorded.
- The shock breakout from 200 mm Cu was used to determine the timing for future diffraction measurements.
- Shocked crystals were recovered and examined.

In recent experiments a multiple film plane (MFP) diagnostic has been implemented that allows the observation of x-ray diffraction from a wide range of lattice planes (Fig. 92.50). The MFP has been used to record diffraction from Si shocked at a range of pressures as seen in Fig. 92.51. Figure 92.52 illustrates the analysis of such images showing a multi-wave structure that depends on intensity. A maximum of 6% compression is observed for the range of pressures attained on Nova and OMEGA in x-ray and direct-drive modes.

A two-phase approach has been adopted to analyze these data. First, the line pattern of known crystal configurations is predicted; then the diffracted lines are fit to the prediction to determine the lattice spacing and unit normal vector. An IDL code is used to calculate the expected diffraction pattern for a given crystal lattice.

*Optical Mixing of Controlled Stimulated Scattering Instabilities (OMC SSI) on OMEGA.*
Principal Investigator: Bedros Afeyan (Polymath Research Inc.) and collaborators from LLNL, LANL, and LLE

The goal of this experiment is to examine suppression of backscattering instabilities by the externally controlled generation of ion-acoustic-wave or electron-plasma-wave turbulence. The experiments in general consist of using optical mixing techniques to generate resonant ion-acoustic waves (IAW) in flowing plasmas created by the explosion of foils irradiated by the OMEGA laser. During this year the interaction scaling with probe intensity was examined.

The transmission of the probe beam and the Raman reflectivity of the pump beam were measured systematically for a large number of probe beam energies. The scaling of the Raman suppression with probe beam energy was examined, and transmission enhancement at low energies that saturates at high energies was observed (see Fig. 92.53). The energy transfer at high probe energies is significant, and the SRS suppression in the wavelength or plasma density window that corresponds to Mach-1 flow is suppressed significantly, upwards of factors of 8.

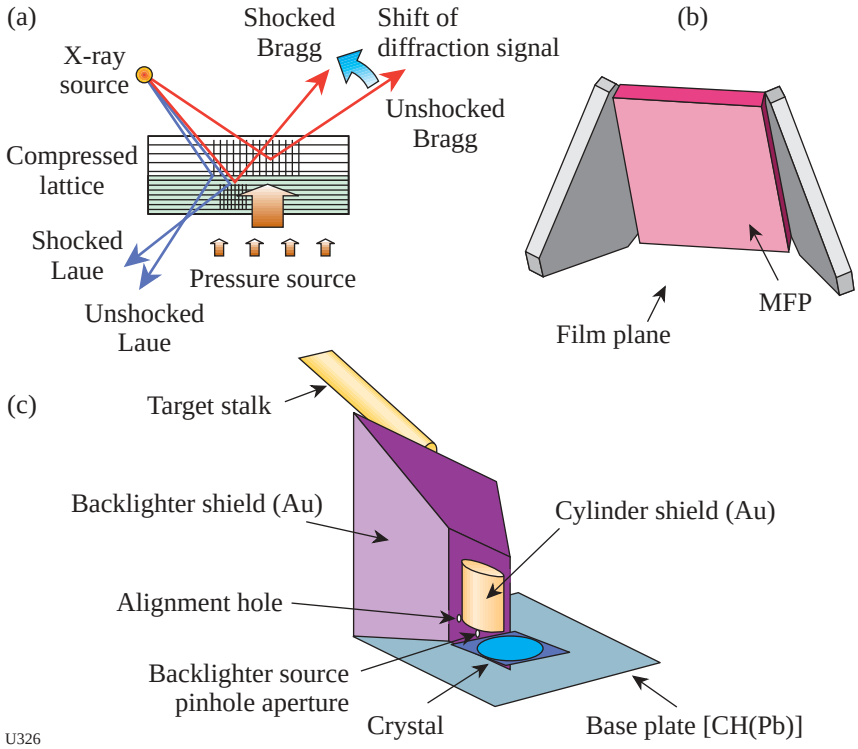


Figure 92.50
(a) Illustration of the concept of dynamic x-ray diffraction in probing response of crystals to laser-driven shocks; (b) schematic showing the MFP diagnostic; and (c) illustration of typical experimental configuration used on the x-ray diffraction experiments.

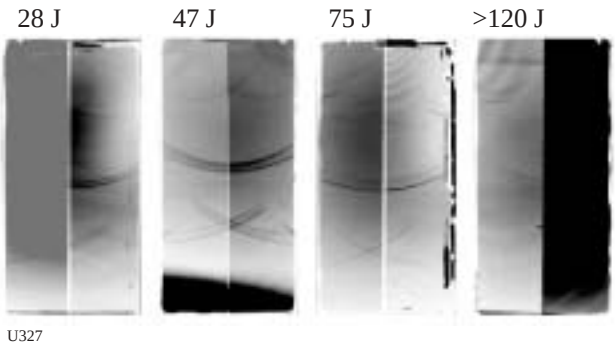


Figure 92.51
Images of a diffracted signal from different lattice planes taken from a shocked-Si experiment on OMEGA at different laser-drive energies.

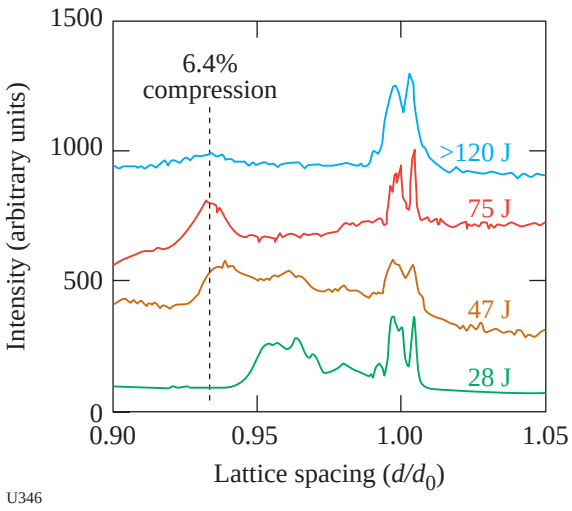


Figure 92.52
Lineout from x-ray diffraction data of Si for various energies showing a maximum lattice compression of ~6.4%.

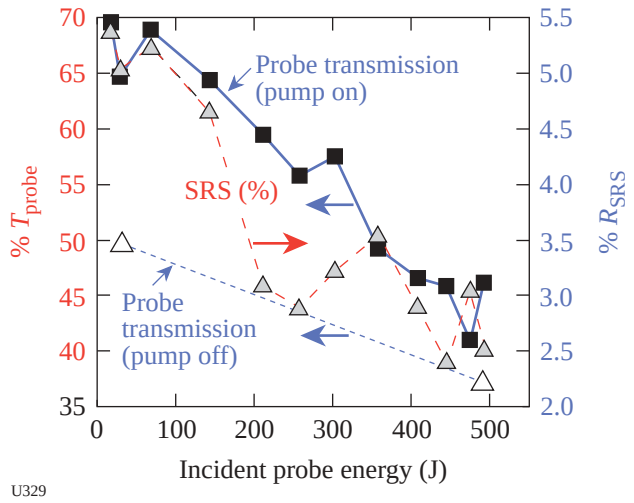


Figure 92.53
Measured transmission of the probe beam and the Raman reflectivity of the pump beam as a function of probe beam energy. Note that with the pump beam off, the transmission of the probe beam is less than 50%, even at moderately low energies, and decreases with energy down to less than 40% at a probe beam energy of ~490 J. The reflectivity of the pump beam falls with increasing probe energy. The energy transfer at high probe energies is significant, and the SRS suppression in the wavelength or plasma density window that corresponds to Mach-1 flow is suppressed significantly, upward of factors of 8.

### FY02 LLNL OMEGA Experimental Program

The LLNL program on OMEGA in FY02 totaled 406 target shots for target ignition physics, high-energy-density science, and NWET (Nuclear Weapons Effects Testing). This represents a 30% increase over the target shots taken by LLNL on OMEGA in FY01. Highlights of these experiments include the following:

*Laser–Plasma Interactions:* Beam-energy-transfer experiments were continued during FY02 to investigate beam-energy transfer[34] for a variety of NIF target/beam configurations in order to select the optimum configuration to minimize the potential deleterious effects of this process on NIF targets.

To expand the LPI (laser–plasma interaction) database on OMEGA, one of the OMEGA beamlines was modified to allow it to generate second-harmonic radiation for LPI experiments.

*Cocktail Hohlraums:* Experiments continued to investigate the potential of "cocktail" hohlraum materials to increase the soft x-ray emission and energy coupling to capsule in NIF targets. During FY02, detailed atomic physics model predictions were verified on OMEGA experiments by observing enhanced cocktail re-emission at 450 eV (see Fig. 92.54).

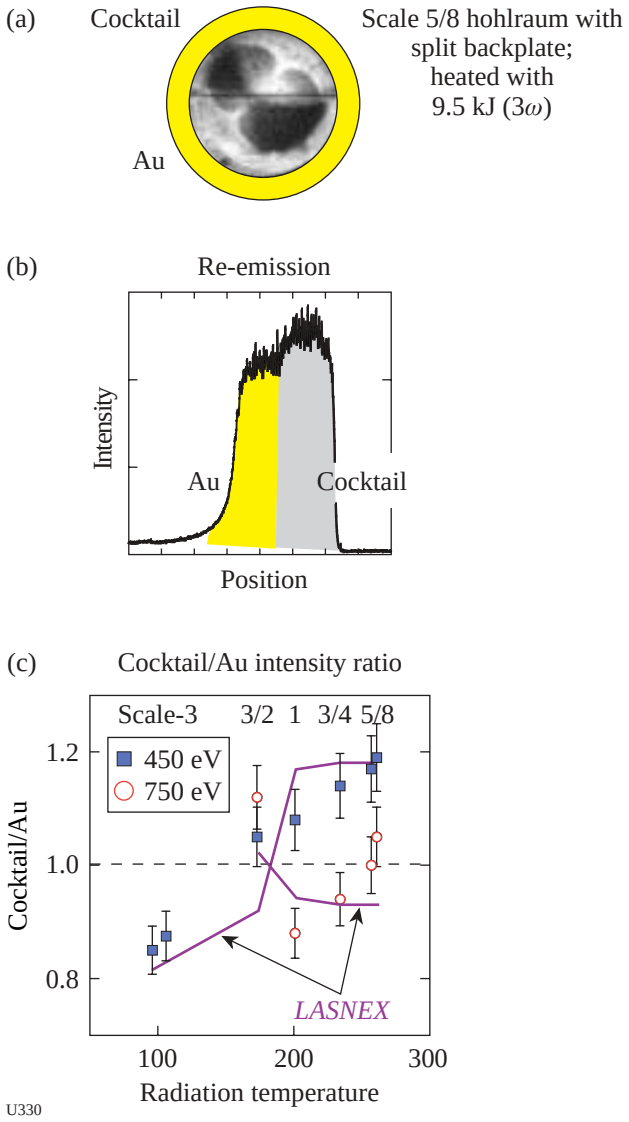


Figure 92.54
During FY02 cocktail hohlraum experiments were conducted on OMEGA that in conjunction with *LASNEX* code simulations indicate that cocktail materials may be advantageous compared to Au for the NIF hohlraums. (a) Cocktail geometry; (b) experimental data from cocktail hohlraum experiment comparing Au and "cocktail" re-emission; (c) cocktail-to-Au intensity ratio at 450 eV (squares) and 750 eV (circles) plotted as a function of radiation temperature from the OMEGA experiments compared to the *LASNEX* predictions.

*X-Ray Thomson Scattering:* X-ray Thomson scattering can access the density/temperature parameter space that is characteristic of the Fermi degenerate to warm dense matter regime (see Fig. 92.55). OMEGA experiments have demonstrated for the first time spectrally resolved x-ray Thomson scattering data[35] (Fig. 92.56). These experiments are important because they indicate that x-ray Thomson scattering may work for ICF implosions. Future experiments are planned to investigate superdense matter using this technique.

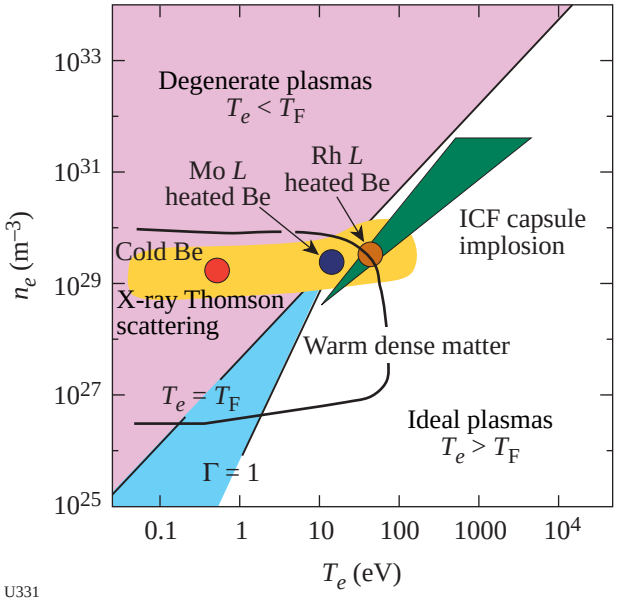


U331

Figure 92.55
The density and temperature space of interest to the study of dense matter showing the relevance of x-ray Thomson scattering as a diagnostic in this regime. The solid points correspond to the measurements made on the OMEGA experiments using Rh and Mo $L$-shell emission as a source of x-rays to conduct x-ray Thomson scattering measurements on cold and heated Be plasmas.

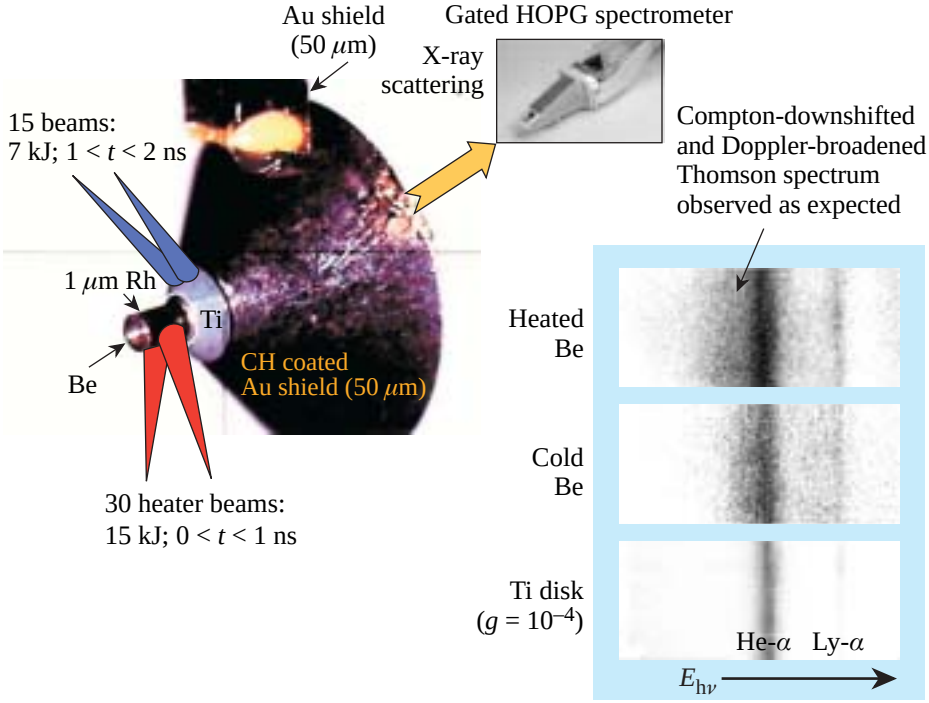


U332

Figure 92.56
Illustration of the x-ray Thomson scattering experiment on OMEGA. Thirty OMEGA beams are used as heater beams to heat a Be plasma. A separate x-ray source is used to probe the hot plasma and produces the scattered Ti-disk spectrum irradiated with up to 15 beams (at the right).

*Albedo Experiments:* A series of experiments were initiated in FY02 on OMEGA to measure the absolute albedo of a secondary hohlraum as shown in Fig. 92.57. Three detectors are used in this measurement: DANTE, a PCD in H11, and a PCD in P11. DANTE is the primary diagnostic, while the P11 PCD monitors the effect of the secondary hohlraum and the H11 PCD serves as backup for the DANTE measurement. Initial measurements confirmed that the secondary hohlraum has no significant effect on the primary's radiation temperature. In measurements comparing the albedo of Au and U, the Au albedo was observed to be smaller than that of U.

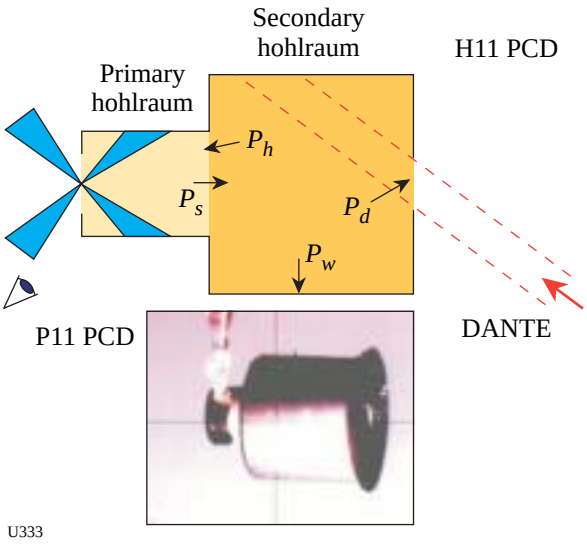


Figure 92.57
Schematic of the "Albedo" experiment. A half-hohlraum is irradiated by a set of OMEGA beams and provides radiation that heats a secondary hohlraum attached to its back. DANTE is the primary diagnostic viewing the wall of the secondary hohlraum; the H11 PCD is a backup for DANTE. The P11 PCD monitors the primary hohlraum to determine the effect of the secondary on its radiation temperature.

*Hot Hohlraum:* A series of experiments are underway on OMEGA to produce high-radiation-temperature hohlraums by reducing the scale size of the hohlraums. Hot hohlraums are needed for NIF opacity experiments, but their physics regime is not well understood. Scaled experiments at OMEGA are used to compare experimental results to theoretical models. The laser coupling to the hohlraum was determined as a function of scale size by measuring x-ray drive, backscatter, and intensity of hot electrons. Scale-1/2 and -1/4 hohlraums were driven in a half-hohlraum configuration, and radiation temperatures of ~350 eV were demonstrated.

*Gas-Filled Radiation Sources:* Experiments continued under an NWET program to develop high-efficiency x-ray sources for the NIF. During FY02 the experiments were designed to explore x-ray emission in the >10-keV region. Typical targets included Kr-filled CH cans (1.2 mm long, 1.5 mm in diameter). Figure 92.58 shows time-framed x-ray images from two experiments with 0.5-atm- and 1.5-atm-Kr-filled cans. X-ray emission is observed from the full extent of the can (1.2-mm × 1.5-mm diameter) and beyond the duration of the 1-ns laser pulse in both cases.

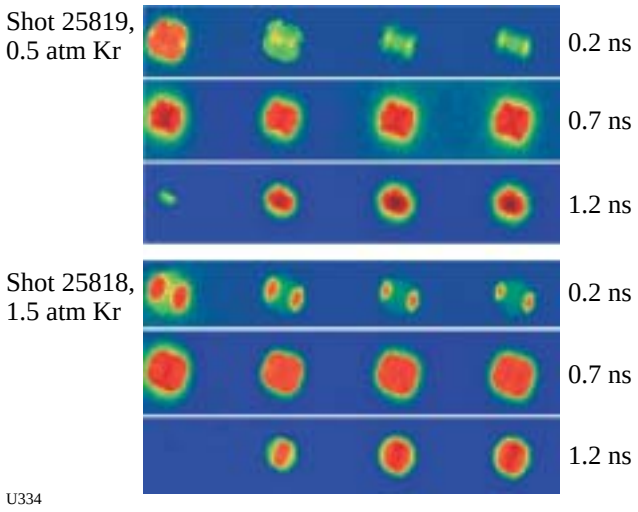


Figure 92.58
X-ray framing camera images from shot 25819 (0.5 atm Kr) and 25818 (1.5 atm Kr) show the pressure dependence in the evolution of >10-keV x-ray emission. The times are referenced to the start of the ~1-ns-long laser pulse.

*Dynamic Hohlraums:* A series of experiments dubbed "dynamic hohlraums" were carried out on OMEGA in direct-drive mode. These experiments were designed to image a radiatively collapsed shock. The configuration is shown schematically in Fig. 92.59. A gas-filled CH shell is irradiated directly by 40 OMEGA beams. To achieve as uniform a drive as possible with only 40 polar beams, the polar-beam energies are lowered in comparison to the rest of the beams. Typical data from these implosions are shown in Fig. 92.60.

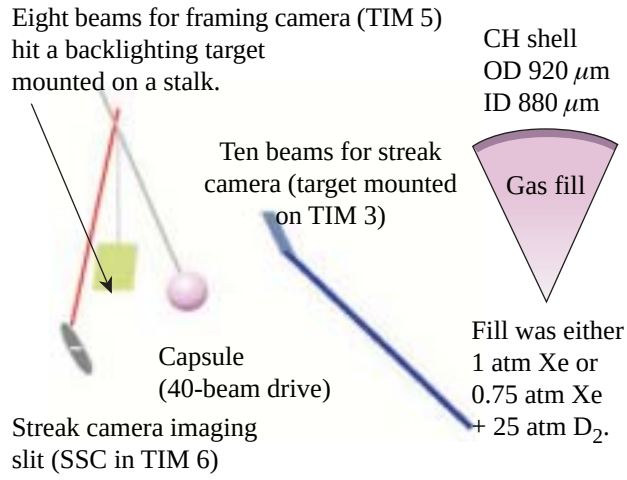


Figure 92.59
Schematic illustration of the "dynamic hohlraum" direct-drive implosion experiment designed to image a radiatively collapsed shock.

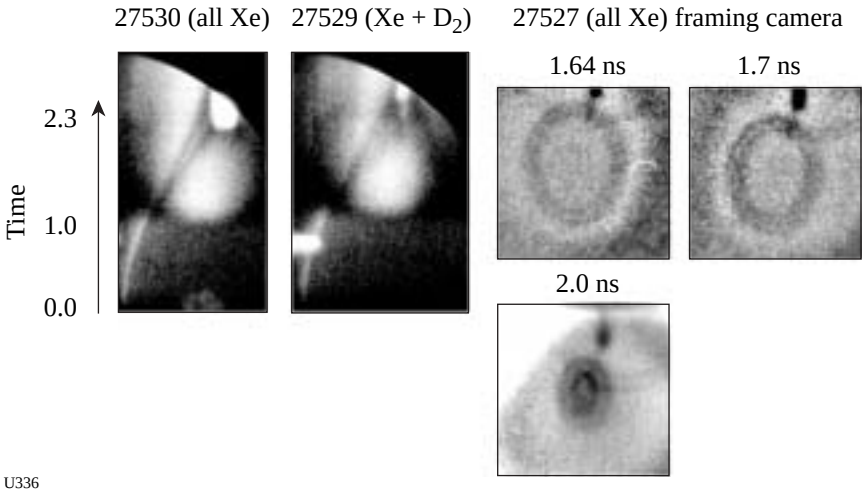


Figure 92.60
Streaked (left) and gated (right) x-ray images of x-ray-backlit implosions of Xe- and Xe/$D_2$-filled CH shells. The separation between the plastic shell and the collapsed shock is discernable in shots with Xe fill but not on shots with partial $D_2$ fills

*Nonideal Implosions:* The nonideal implosion (NIBI) experiment is designed to study highly distorted implosions. This experiment, carried out on OMEGA in FY02, used the direct-drive configuration shown in Fig. 92.61.

Experiments were carried out with symmetrical capsules as well as machined capsules with a 50° radiographic tracer "cap" as shown in Fig. 92.62.

*Double-Shell Implosion Experiments:* The effect of Au M-band asymmetry on the implosion of double-shell capsules is being investigated on OMEGA. The motivation for this work is that 80% of the radiation reaching the inner shell in a double-shell configuration is 2 to 4 keV Au "M-band" radiation. Simulations indicate that the inner glass shell will suffer an ~25% distortion from an ~10% P2 M-band asymmetry at a convergence of ~60%. To ameliorate this problem, an elongated hohlraum configuration is being explored.

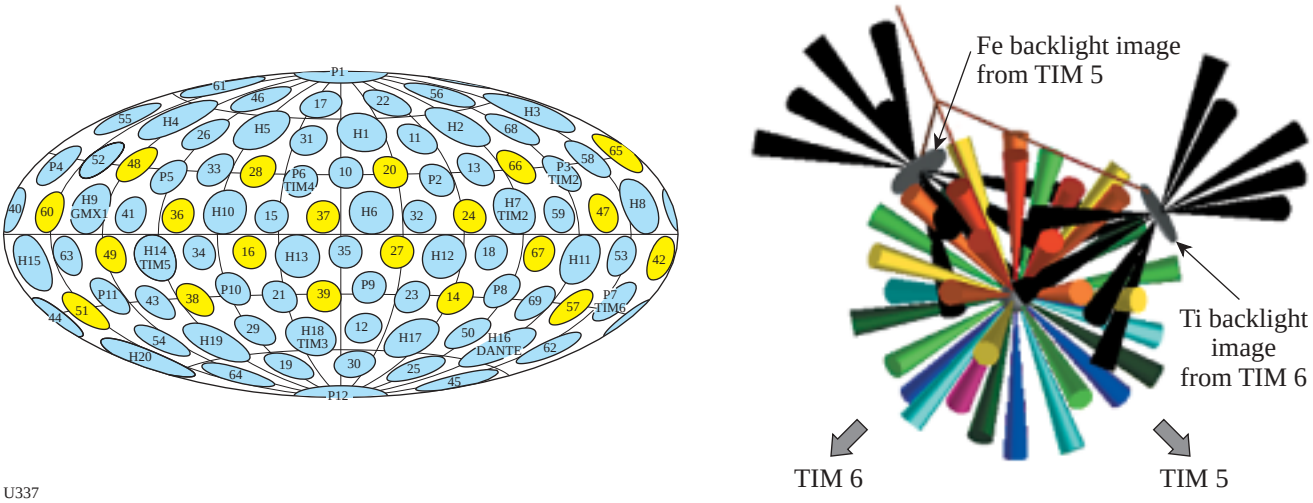


Figure 92.61
System configuration for the OMEGA NIBI experiment. Forty OMEGA beams are used to drive the implosion while twenty beams are used to produce two separate backlighting views. The forty drive beams can be adjusted to produce various asymmetric drive configurations. The beams indicated in yellow on the left are used for the two backlighting views.

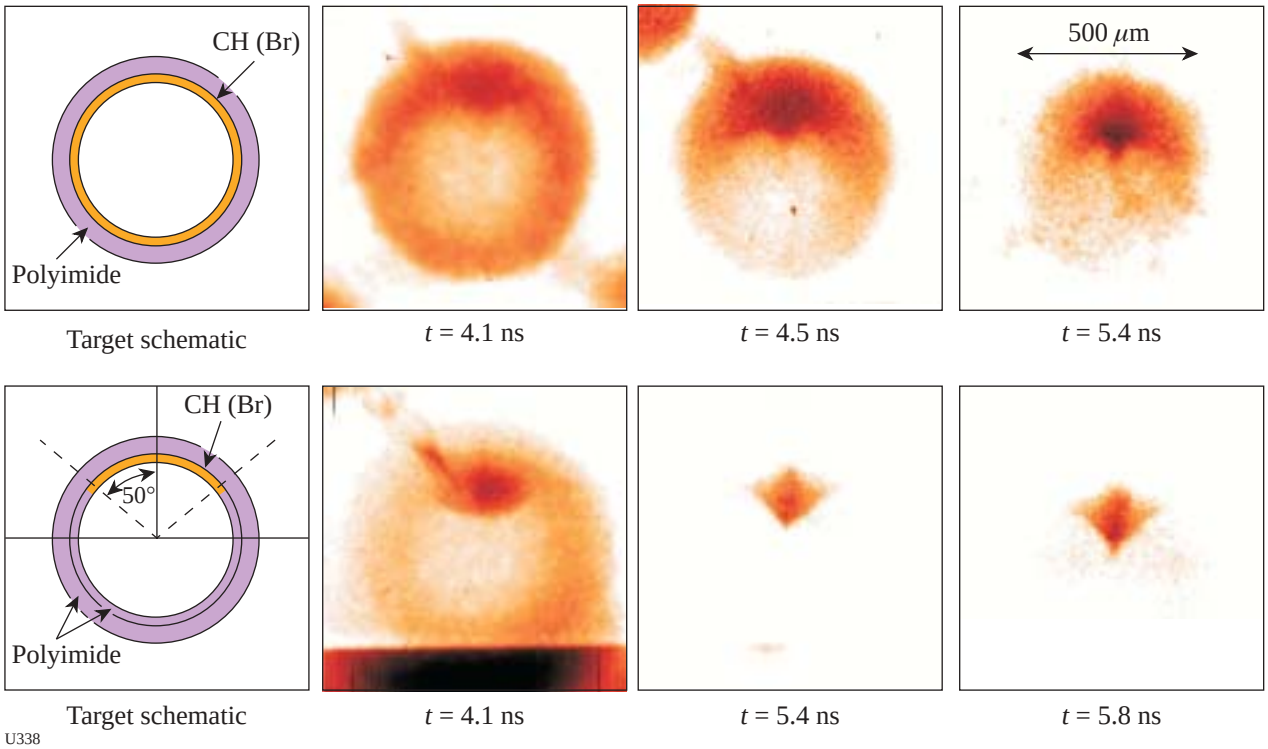


Figure 92.62
Target schematics (left top and bottom) for some of the NIBI implosion targets. The time-gated x-ray-backlit images on the right show the evolution of the core asymmetry when the targets are driven with a strong $\ell = 1$ mode (higher energy on the top pole).

*Charged-Particle Spectrometry in Indirect-Drive Implosions:* To assess the effectiveness of charged-particle spectrometry on the NIF, a collaborative experiment involving LLNL, MIT PSFC, and LLE was implemented on OMEGA in FY02. During the experiment $D^3He$-filled shells were imploded in a conventional hohlraum configuration. Wedged-range-filter (WRF) spectrometers were used to measure the yield, spectrum, and spatial distribution of primary $D^3He$ protons. Initial results from these shots indicate that capsule areal density can be measured with this configuration. When viewed through a diagnostic hole in the hohlraum, the proton slowing down indicated a capsule $\rho R \sim 42 \pm 9$ mg/cm$^2$ compared to a predicted areal density of ~49 mg/cm$^2$. No large asymmetries in proton emission were observed. It was concluded that charged-particle spectrometry can be an important diagnostic technique for indirect-drive targets. Improvements in the diagnostic were suggested by the results of these experiments to optimize the technique for indirect-drive experiments.

*IDrive:* Work continued on OMEGA in FY02 to implement the IDrive technique as a high-pressure drive technique for materials studies. One of the goals of this program is to measure the material strength of solid aluminum (6061) at peak pressures of ~300 kbar. The experiments include soft recovery of accelerated foils in order to provide the opportunity for microscopic analysis of the highly strained regions of the materials.

**FY02 LANL OMEGA Experimental Program**

The LANL program on OMEGA in FY02 continued experiments in support of stockpile stewardship (ACE), cylindrical mix (CYLMIX), and double-shell implosion campaigns and began the asymmetric direct-drive sphere (ADDS) campaign. LANL continued NIF phase-2 diagnostic development and also collaborated with a large national group on the hydrodynamic jet experiment. LANL also provided shock-breakout measurements for the Sandia National Laboratory (SNL) ablator characterization campaign. Each of these experimental campaigns has been documented in pre- and post-shot reports. Highlights of these experiments include the following:

*ACE Experiments:* The ACE experiments successfully obtained data in support of the Stockpile Stewardship Program. This year a new backlighter configuration was developed that provides views of the experiment at two different times, thus increasing the efficiency of the experiments. In collaboration with AWE, a fluorescence-based spectro-meter was fielded to measure temperatures in radiation-driven experiments.

*Asymmetric Direct-Drive Spheres:* The goal of the asymmetric direct-drive spheres (ADDS) campaign is to elucidate the effect of mix on imploding capsules. The experiment uses directly driven DT-filled capsules. The energies of each laser beam are adjusted so that the capsule sees a positive or negative drive asymmetry as measured by the second Legendre mode. Theoretical calculations predict a difference in neutron yield and core shape, depending on the sign and magnitude of the asymmetry. The primary diagnostics of mix are neutron yield, imaging of the emitted neutrons, and x-ray imaging (in collaboration with LLE).

Figure 92.63 presents the first simultaneous neutron and x-ray images of asymmetric implosions. The predicted shapes and neutron yields agree with the measurements in direction and magnitude.

*CYLMIX:* The Richtmyer–Meshkov instability occurs whenever a strong shock passes through an interface between two materials. The CYLMIX experiments study this instability under unique convergent, compressible, miscible plasma conditions in the presence of a strong (Mach number greater than 5) shock. To produce a strong shock, small plastic cylinders (Fig. 92.64) are directly driven by the OMEGA laser.[36] The implosion trajectory has been carefully mapped and simulations tuned to match the measurements, as in Fig. 92.65.

As the cylinders implode, the marker band mixes into the surrounding material and the mix width is measured. This year, extensive measurements spanning several nanoseconds were made of the dependence of the mix width on the initial surface roughness of the marker layer as a function of time. Comparisons with simulations to validate hydrodynamic models have been made.

*Hydrodynamic Jet Experiment:* LANL also participated in a large collaboration that includes researchers from LLNL, AWE, LLE, U. Michigan, and NRL to simulate jets in supernova explosions.[37] Astrophysical codes will be validated by comparison to OMEGA experimental data. The experiments are presently optimizing the target and diagnostics while design work linking 2-D *LASNEX* calculations to the radiation-hydrodynamic code *RAGE* is underway. Exploratory experiments were conducted this year.

*NIF Diagnostics:* Development continued on Phase 2 fusion product diagnostics for the NIF. A second Gas–Cerenkov gamma-ray burn-history diagnostic, with increased time reso-

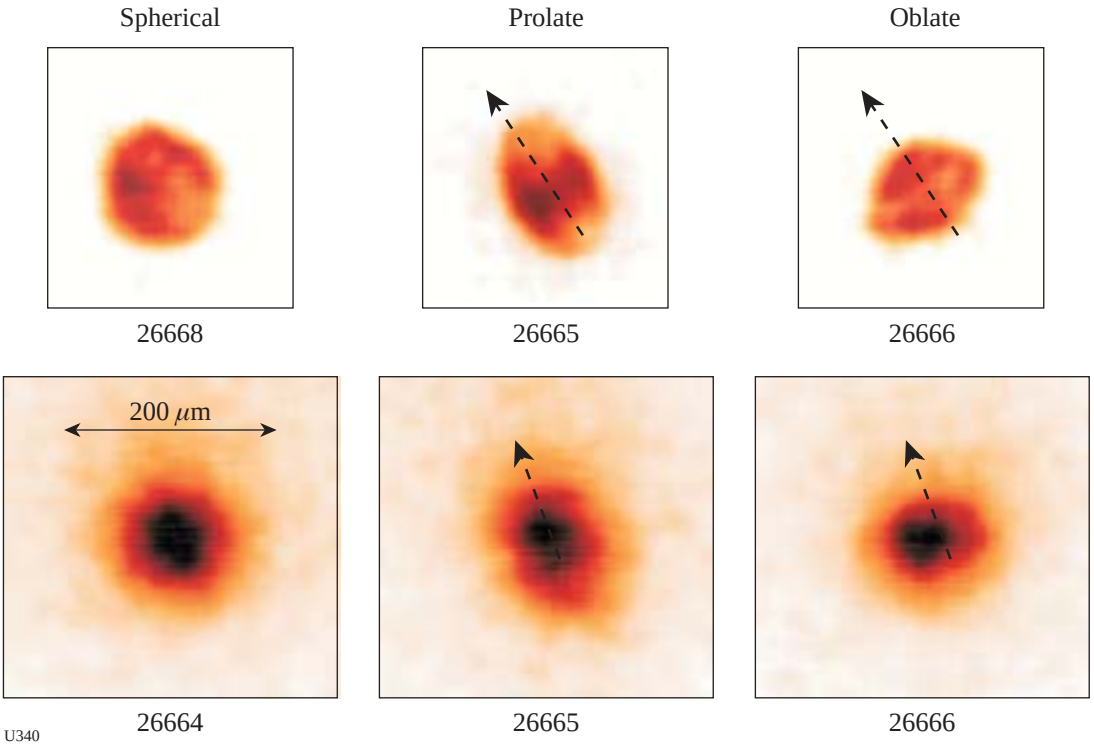


Figure 92.63
X-ray (top) and neutron (bottom) images for three different degrees of asymmetric drive. The x-ray images are from the GMXI diagnostic, and the 14.1-MeV neutron images were obtained in a LANL/CEA/LLE collaboration. All images are as seen by the diagnostic. The arrows indicate the perturbation axis.

Figure 92.64
A view of a typical CYLMIX target from the side showing the backlighter disk on the right, the Al marker band in the middle, the foam inside the cylinder (white areas), and the viewing aperture on the left. The primary diagnostic is an x-ray framing camera with a line of sight down the axis of the cylinder.

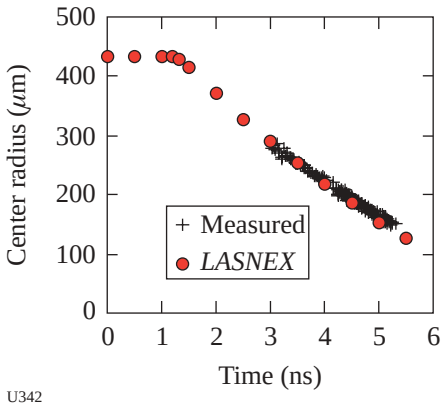


Figure 92.65
Measured radius versus time plot demonstrating good modeling of the experiment.

lution, was built and fielded in conjunction with LLNL. Development continued on the neutron imaging system (NIS), which was a primary diagnostic for the ADDS experiment, as illustrated in Fig. 92.63. The NIS is fielded in collaboration with CEA and LLE.

**FY02 SNL OMEGA Programs**

SNL carried out a total of 24 target shots on the OMEGA laser in FY02 and also participated in several of the campaigns led by other laboratories. The SNL-led campaigns included the following:

*Indirect-Drive Ablator Shock Coalescence:* The achievement of indirect-drive ignition of a NIF capsule requires capsule shock timing precision of ~150 ps. The first attempts at time-resolved measurement of the coalescence of two shocks (at pressures of ~10 and 50 Mbar, respectively) in a Be + 0.9% Cu wedge ablator were made in a collaborative effort involving SNL and LANL. The principal diagnostic was the LANL Streaked Optical Pyrometer (SOP).[38] The hohlraum drive for this experiment consisted of a 2-ns square pulse in six beams followed by a 1-ns square pulse in nine beams delayed by 1 ns. As shown in Fig. 92.66, shock coalescence occurred within about 300 ps of the pre-shot calculation.

*Indirect-Drive Ablator Shock Velocity at 50 Mbar:* The achievement of indirect-drive ignition of a NIF capsule requires capsule ablation pressures in the range of 1 to 100 Mbars. In FY02 SNL/LANL experiments on OMEGA extended the shock velocity data for Be + 0.9% Cu ablator samples to the 50-Mbar level[39] (Fig. 92.67). Shock velocities in the ablator were measured with Be + 0.9% Cu step samples. Al step witness plates were also used to confirm the shock pressure levels generated in the Be + 0.9% Cu ablator samples.

*Indirect-Drive Ablator X-Ray Burnthrough Measurements:* To achieve indirect-drive ignition of a NIF capsule, ablator burnthrough timing must be predicted to within a few percent. In FY02 SNL/LLNL experiments on OMEGA extended the x-ray burnthrough[39] data for polyimide and Be + 0.9% Cu ablators into the range of 190- to 200-eV hohlraum temperatures. As shown in Fig. 92.68, the experimental technique provides simultaneous measurements of ablator x-ray burnthough and x-ray re-emission (in the interior of the hohlraum). As shown in the figure, experimental arrangements involving multiple sample regions were also tested in the FY02 experiments.

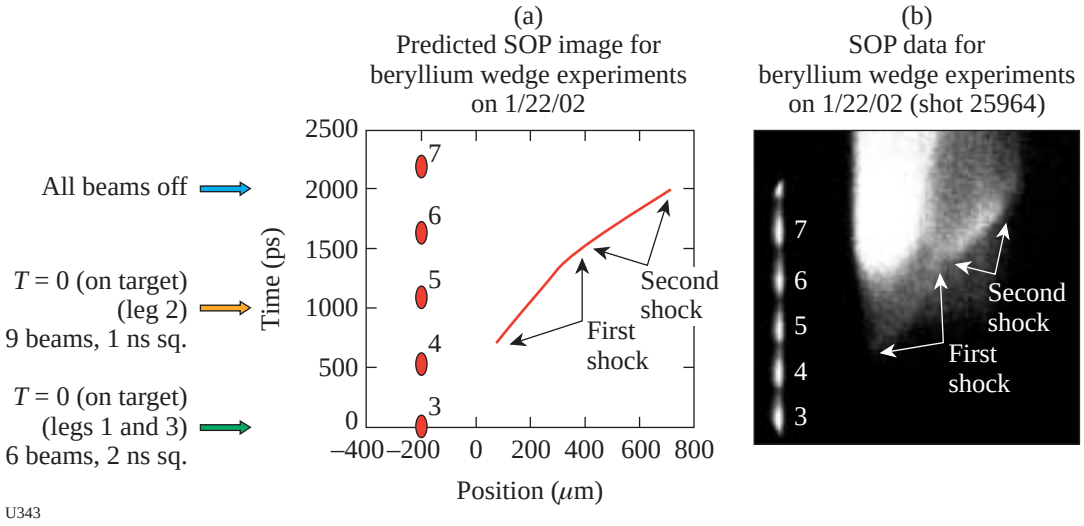


Figure 92.66
Predicted (a) and actual (b) shock coalesence as measured with SOP.

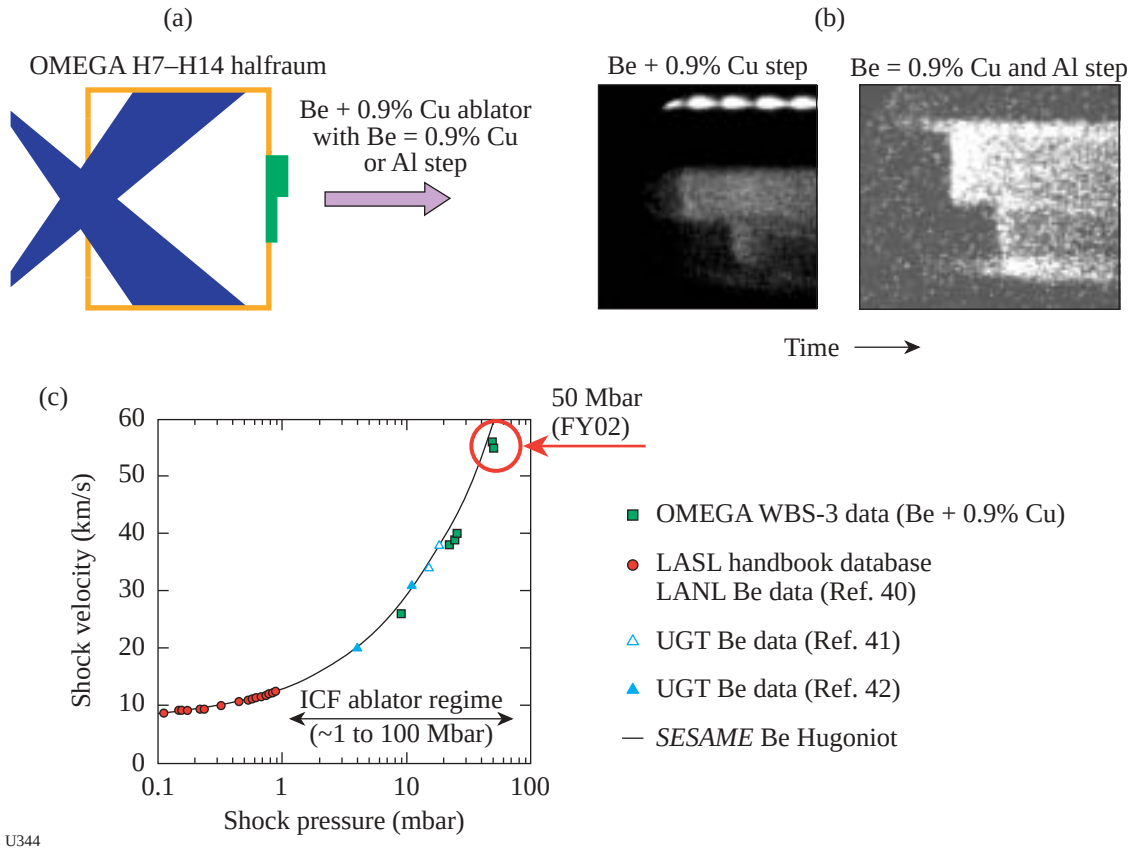


Figure 92.67
(a) Schematic illustrating the setup of a shock velocity measurement experiment. A step target is mounted on the back of a half-hohlraum that is irradiated by a subset of OMEGA beams. (b) Experimental data from two shock velocity measurement experiments. (c) Plot of shock velocity versus shock pressure from the OMEGA experiments compared to data from other sources in the ICF-ablator–relevant regime of interest.

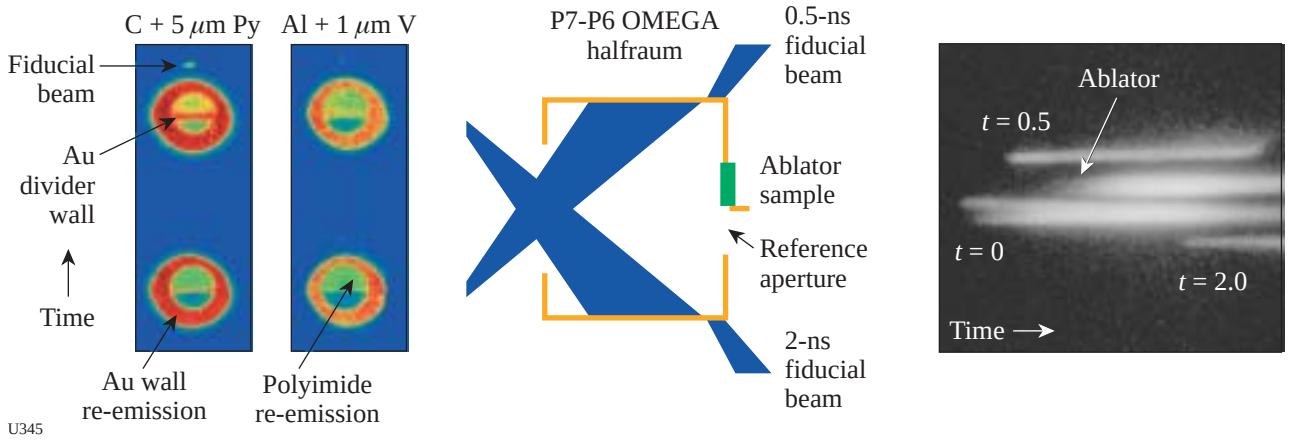


Figure 92.68
Schematic illustrating the ablator burnthrough measurement technique used on the SNL experiments on OMEGA.

*Time and Spatially Resolved Measurements of X-Ray Burnthrough and Re-emission in Au and Au:Dy:Nd Foils:* A mixture containing two or more high-*Z* elements can result in a material with a higher Rosseland mean opacity than either of the constituents. Computational simulations of the x-ray re-emission properties of such "cocktail" materials indicate that wall losses in a National Ignition Facility (NIF) ignition-scale hohlraum could be reduced by a significant amount (when compared to walls made of pure Au).[43] In a recent set of experiments on OMEGA a collaborative team including SNL, LLNL, and GA used x-ray framing and streak cameras to simultaneously measure the x-ray burnthrough and re-emission of pure Au and Au:Dy:Nd cocktail samples exposed to a hohlraum radiation temperature of ~160 eV. Although the burnthrough measurements indicate the cocktail has a higher Rosseland mean opacity than pure Au, the measured x-ray re-emission fluxes from the two materials were approximately equivalent.

**CEA**

CEA had four half-day dedicated shot opportunities on OMEGA during FY02. A total of 19 target shots were provided for experiments including tests of the LMJ three-ring symmetry and other aspects of indirect-drive targets. In addition, CEA participated in collaborative experiments on imaging the neutron core emission using the CEA-provided neutron-imaging system (NIS).[44]

REFERENCES


1. B. Yaakobi, F. J. Marshall, and D. K. Bradley, Appl. Opt. **37**, 8074 (1998).
2. S. W. Haan *et al.*, Phys. Plasmas **2**, 2480 (1995).
3. J. D. Lindl, R. L. McCrory, and E. M. Campbell, Phys. Today **45**, 32 (1992).
4. *Energy and Technology Review*, Lawrence Livermore National Laboratory, Livermore, CA, UCRL-52000-94-12, 1 (1994).
5. M. D. Rosen, Phys. Plasmas **3**, 1803 (1996).
6. M. Andre, M. Novaro, and D. Schirmann, Chocs **13**, 73 (1995); J. Maddox, Nature **372**, 127 (1994).
7. C. K. Li, D. G. Hicks, F. H. Séguin, J. A. Frenje, R. D. Petrasso, J. M. Soures, P. B. Radha, V. Yu. Glebov, C. Stoeckl, D. R. Harding, J. P. Knauer, R. L. Kremens, F. J. Marshall, D. D. Meyerhofer, S. Skupsky, S. Roberts, C. Sorce, T. C. Sangster, T. W. Phillips, M. D. Cable, and R. J. Leeper, Phys. Plasmas **7**, 2578 (2000).
8. F. H. Séguin, J. A. Frenje, C. K. Li, D. G. Hicks, S. Kurebayashi, J. R. Rygg, B.-E. Schwartz, R. D. Petrasso, S. Roberts, J. M. Soures, D. D. Meyerhofer, T. C. Sangster, C. Sorce, V. Yu. Glebov, C. Stoeckl, T. W. Phillips, R. J. Leeper, K. Fletcher, and S. Padalino, "Spectrometry of Charged Particles from Inertial-Confinement-Fusion Plasmas," to be published in the Review of Scientific Instruments.
9. F. H. Séguin, C. K. Li, D. G. Hicks, J. A. Frenje, K. M. Green, R. D. Petrasso, J. M. Soures, D. D. Meyerhofer, V. Yu. Glebov, C. Stoeckl, P. B. Radha, S. Roberts, C. Sorce, T. C. Sangster, M. D. Cable, S. Padalino, and K. Fletcher, Phys. Plasmas **9**, 2725 (2002).
10. F. H. Séguin, C. K. Li, J. A. Frenje, S. Kurebayashi, R. D. Petrasso, F. J. Marshall, D. D. Meyerhofer, J. M. Soures, T. C. Sangster, C. Stoeckl, J. A. Delettrez, P. B. Radha, V. A. Smalyuk, and S. Roberts, Phys. Plasmas **9**, 3558 (2002).
11. R. D. Petrasso, C. K. Li, M. D. Cable, S. M. Pollaine, S. W. Haan, T. P. Bernat, J. D. Kilkenny, S. Cremer, J. P. Knauer, C. P. Verdon, and R. L. Kremens, Phys. Rev. Lett. **77**, 2718 (1996).
12. D. D. Meyerhofer, J. A. Delettrez, R. Epstein, V. Yu. Glebov, V. N. Goncharov, R. L. Keck, R. L. McCrory, P. W. McKenty, F. J. Marshall, P. B. Radha, S. P. Regan, S. Roberts, W. Seka, S. Skupsky, V. A. Smalyuk, C. Sorce, C. Stoeckl, J. M. Soures, R. P. J. Town, B. Yaakobi, J. D. Zuegel, J. Frenje, C. K. Li, R. D. Petrasso, D. G. Hicks, F. H. Séguin, K. Fletcher, S. Padalino, M. R. Freeman, N. Izumi, R. Lerche, T. W. Phillips, and T. C. Sangster, Phys. Plasmas **8**, 2251 (2001).
13. D. D. Meyerhofer, J. A. Delettrez, R. Epstein, V. Yu. Glebov, V. N. Goncharov, R. L. Keck, R. L. McCrory, P. W. McKenty, F. J. Marshall, P. B. Radha, S. P. Regan, S. Roberts, W. Seka, S. Skupsky, V. A. Smalyuk, C. Sorce, C. Stoeckl, J. M. Soures, R. P. J. Town, B. Yaakobi, J. Frenje, C. K. Li, R. D. Petrasso, F. H. Séguin, K. Fletcher, S. Padalino, C. Freeman, N. Izumi, R. A. Lerche, T. W. Phillips, and T. C. Sangster, Plasma Phys. Control. Fusion **43**, A277 (2001).
14. P. B. Radha, J. Delettrez, R. Epstein, V. Yu. Glebov, R. Keck, R. L. McCrory, P. McKenty, D. D. Meyerhofer, F. Marshall, S. P. Regan, S. Roberts, T. C. Sangster, W. Seka, S. Skupsky, V. Smalyuk, C. Sorce, C. Stoeckl, J. Soures, R. P. J. Town, B. Yaakobi, J. Frenje, C. K. Li, R. Petrasso, F. Séguin, K. Fletcher, S. Padalino, C. Freeman, N. Izumi, R. Lerche, and T. W. Phillips, Phys. Plasmas **9**, 2208 (2002).
15. C. K. Li, F. H. Séguin, J. A. Frenje, S. Kurebayashi, R. D. Petrasso, D. D. Meyerhofer, J. M. Soures, J. A. Delettrez, V. Yu. Glebov, P. B. Radha, F. J. Marshall, S. P. Regan, S. Roberts, T. C. Sangster, and C. Stoeckl, Phys. Rev. Lett. **89**, 165002 (2002).
16. C. K. Li, F. H. Séguin, D. G. Hicks, J. A. Frenje, K. M. Green, S. Kurebayashi, R. D. Petrasso, D. D. Meyerhofer, J. M. Soures, V. Yu. Glebov, R. L. Keck, P. B. Radha, S. Roberts, W. Seka, S. Skupsky, C. Stoeckl, and T. C. Sangster, Phys. Plasmas **8**, 4902 (2001).
17. V. A. Smalyuk, V. N. Goncharov, J. A. Delettrez, F. J. Marshall, D. D. Meyerhofer, S. P. Regan, and B. Yaakobi, Phys. Rev. Lett. **87**, 155002 (2001).
18. T. R. Boehly, D. L. Brown, R. S. Craxton, R. L. Keck, J. P. Knauer, J. H. Kelly, T. J. Kessler, S. A. Kumpan, S. J. Loucks, S. A. Letzring, F. J. Marshall, R. L. McCrory, S. F. B. Morse, W. Seka, J. M. Soures, and C. P. Verdon, Opt. Commun. **133**, 495 (1997).

19. R. A. Lerche, D. W. Phillion, and G. L. Tietbohl, Rev. Sci. Instrum. **66**, 933 (1995).

20. R. D. Petrasso, C. K. Li, F. H. Séguin, J. A. Frenje, S. Kurebayashi, P. B. Radha, D. D. Meyerhofer, J. M. Soures, J. A. Delettrez, C. Stoeckl, S. Roberts, V. Yu. Glebov, W. Seka, C. Chiritescu, and T. C. Sangster, Bull. Am. Phys. Soc. **46**, 105 (2001).

21. C. K. Li and R. D. Petrasso, Phys. Rev. Lett. **70**, 3059 (1993).

22. From other $D^3He$ implosion experiments for which the signals are similar in amplitude to those of Fig. 92.38(b), the presence of the shock yield is clearly visible, so the absence of the shock yield in Fig. 92.38(b) is not due to lack of instrument sensitivity.

23. E. Goldman, Laboratory for Laser Energetics Report No. 16, University of Rochester (1973).

24. R. K. Fisher, R. B. Stephens, L. Disdier, J. L. Bourgade, A. Rouyer, P. A. Jaanimagi, T. C. Sangster, R. A. Lerche, and N. Izumi, Phys. Plasmas **9**, 2182 (2002).

25. M. Tabak *et al.*, Phys. Plasmas **1**, 1626 (1994).

26. P. A. Norreys *et al.*, Phys. Plasmas **7**, 3721 (2000).

27. C. A. Iglesias and F. J. Rogers, Astrophys. J. **464**, 943 (1996); F. J. Rogers, F. J. Swenson, and C. A. Iglesias, Astrophys. J. **456**, 902 (1996).

28. P. A. Keiter, R. P. Drake, T. S. Perry, H. F. Robey, B. A. Remington, C. A. Iglesias, R. J. Wallace, and J. Knauer, Phys. Rev. Lett. **89**, 165003 (2002).

29. R. P. Drake and P. A. Keiter, Phys. Plasmas **9**, 382 (2002).

30. R. P. Drake, H. F. Robey, O. A. Hurricane, H. Zhang, B. A. Remington, J. Knauer, J. Glimm, D. Arnett, J. O. Kane, K. S. Budil, and J. Grove, Astrophys. J. **564**, 896 (2002).

31. C. Calder *et al.*, Astrophys. J. Suppl. Ser. **143**, 201 (2002).

32. H. F. Robey *et al.*, "The Onset of Turbulence in High Reynolds Number, Accelerated Flows. Part II. Experiment," submitted to Physics of Fluids.

33. M. A. Meyers *et al.*, in *Shock Compression of Condensed Matter, AIP Conference Proceedings 620* (American Institute of Physics, New York, 2001), pp. 619–622; D. H. Kalantar *et al.*, in *Shock Compression of Condensed Matter, AIP Conference Proceedings 620* (American Institute of Physics, New York, 2001), pp. 615–618.

34. R. K. Kirkwood, J. D. Moody, A. B. Langdon, B. I. Cohen, E. A. Williams, M. R. Dorr, J. A. Hittinger, R. Berger, P. E. Young, L. J. Suter, L. Divol, S. H. Glenzer, O. L. Landen, and W. Seka, Phys. Rev. Lett. **89**, 215003 (2002).

35. S. H. Glenzer *et al.*, Bull. Am. Phys. Soc. **47**, 63 (2002); G. Gregori *et al., ibid.*

36. C. W. Barnes, S. H. Batha, A. M. Dunne, G. R. Magelssen, S. Rothman, R. D. Day, N. E. Elliott, D. A. Haynes, R. L. Holmes, J. M. Scott, D. L. Tubbs, D. L. Youngs, T. R. Boehly, and P. A. Jaanimagi, Phys. Plasmas **9**, 4431 (2002).

37. J. M. Foster *et al.*, Phys. Plasmas **9**, 2251 (2002).

38. J. A. Oertel *et al.*, Rev. Sci. Instrum. **70**, 803 (1999).

39. R. E. Olson *et al.*, Bull. Am. Phys. Soc. **47**, 329 (2002).

40. S. P. Marsh, ed. *LASL Shock Hugoniot Data*, Los Alamos Series on Dynamic Material Properties (University of California Press, Berkeley, CA, 1980).

41. C. E. Ragan III, Phys. Rev. A **25**, 3360 (1982).

42. W. J. Nellis *et al.*, J. Appl. Phys. **82**, 2225 (1997).

43. L. Suter *et al.*, Phys. Plasmas **7**, 2092 (2000).

44. L. Disdier *et al.*, Nucl. Instrum. Methods Phys. Res. A **489**, 496 (2002).

# Publications and Conference Presentations

## Publications


T. R. Boehly, T. J. B. Collins, O. Gotchev, T. J. Kessler, J. P. Knauer, T. C. Sangster, and D. D. Meyerhofer, "Observations of Modulated Shock Waves in Solid Targets Driven by Spatially Modulated Laser Beams," J. Appl. Phys. **92**, 1212 (2002).

H. Brunnader, W. T. Shmayda, D. R. Harding, L. D. Lund, and R. Janezic, "Advanced Tritium Recovery System," Fusion Sci. Technol. **41**, 840 (2002)

Y. Cao, H. Li, J. A. Szpunar, and W. T. Shmayda, "Effects of Textures on Hydrogen Diffusion in Nickel," in *Textures of Materials*, Materials Science Forum, Vols. 408–412, edited by D. N. Lee (Trans Tech Publications, Aedermannsdorf, Switzerland, 2002), Part 2, pp. 1139–1144.

I. V. Igumenshchev, "On Angular Momentum Transport in Convection-Dominated Accretion Flows," Astrophys. J. **577**, L31 (2002).

S. D. Jacobs and L. L. Gregg, "Making Waves with the Optics Suitcase," Opt. Photonics News **13**, 12 (2002).

T. Z. Kosc, K. L. Marshall, S. D. Jacobs, J. C. Lambropoulos, and S. M. Faris, "Electric-Field-Induced Motion of Polymer Cholesteric Liquid-Crystal Flakes in a Moderately Conductive Fluid," Appl. Opt. **41**, 5362 (2002).

M. V. Kozlov and C. J. McKinstrie, "Sound Waves in Two-Ion Plasmas," Phys. Plasmas **9**, 3783 (2002).

P. Kús, A. Plecenik, L. Satrapinsky, Y. Xu, and R. Sobolewski, "Superconducting Properties of $MgB_2$ Thin Films Prepared on Flexible Substrates," Appl. Phys. Lett. **81**, 2199 (2002).

S. Papernov and A. W. Schmid, "Establishing Links Between Single Gold Nanoparticles Buried Inside $SiO_2$ Thin Film and 351-nm Pulsed Laser Damage Morphology," in *Laser-Induced Damage in Optical Materials: 2001*, edited by G. J. Exarhos, A. H. Guenther, K. L. Lewis, M. J. Soileau, and C. J. Stolz (SPIE, Bellingham, WA, 2002), Vol. 4679, pp. 282–292.

S. P. Regan, J. A. Delettrez, F. J. Marshall, J. M. Soures, V. A. Smalyuk, B. Yaakobi, R. Epstein, V. Yu. Glebov, P. A. Jaanimagi, D. D. Meyerhofer, P. B. Radha, T. C. Sangster, W. Seka, S. Skupsky, C. Stoeckl, R. P. J. Town, D. A. Haynes, Jr., I. E. Golovkin, C. F. Hooper, Jr., J. A. Frenje, C. K. Li, R. D. Petrasso, and F. H. Séguin, "Shell Mix in Compressed Core of Spherical Implosions," Phys. Rev. Lett. **89**, 085003 (2002).

S. P. Regan, J. A. Delettrez, B. Yaakobi, V. A. Smalyuk, F. J. Marshall, R. Epstein, V. Yu. Glebov, P. A. Jaanimagi, D. D. Meyerhofer, P. B. Radha, W. Seka, S. Skupsky, J. M. Soures, C. Stoeckl, R. P. J. Town, D. A. Haynes, Jr., I. Golovkin, C. F. Hooper, Jr., J. A. Frenje, C. K. Li, R. D. Petrasso, and F. H. Séguin, "High-Density, Direct-Drive Implosions on OMEGA," in *Inertial Fusion Sciences and Applications 2001*, edited by K. A. Tanaka, D. D. Meyerhofer, and J. Meyer-ter-Vehn (Elsevier, Paris, 2002), pp. 89–95.

F. H. Séguin, C. K. Li, J. A. Frenje, S. Kurebayashi, R. D. Petrasso, F. J. Marshall, D. D. Meyerhofer, J. M. Soures, T. C. Sangster, C. Stoeckl, J. A. Delettrez, P. B. Radha, V. A. Smalyuk, and S. Roberts, "Measurements of $\rho R$ Asymmetries at Burn Time in Inertial-Confinement-Fusion Capsules," Phys. Plasmas **9**, 3558 (2002).

C. R. Shmayda, W. T. Shmayda, and N. P. Kherani, "Monitoring Tritium Activity on Surfaces: Recent Developments," Fusion Sci. Technol. **41**, 500 (2002).

W. T. Shmayda, A. Bruggeman, J. Braet, and S. Vanderbiesen, "Treatment of Tritiated Solvents," Fusion Sci. Technol. **41**, 721 (2002).

W. T. Shmayda and R. D. Gallagher, "Recovery of Tritium from Pharmaceutical Mixed Waste Liquids," Fusion Sci. Technol. **41**, 726 (2002).

R. W. Short and A. Simon, "Damping of Perturbations in Weakly Collisional Plasmas," Phys. Plasmas **9**, 3245 (2002).

S. Skupsky, R. Betti, T. J. B. Collins, V. N. Goncharov, D. R. Harding, R. L. McCrory, P. W. McKenty, D. D. Meyerhofer, and R. P. J. Town, "High-Gain Direct-Drive Target Designs for the National Ignition Facility," in *Inertial Fusion Sciences and Applications 2001*, edited by K. A. Tanaka, D. D. Meyerhofer, and J. Meyer-ter-Vehn (Elsevier, Paris, 2002), pp. 243–245.

R. P. J. Town, J. A. Delettrez, R. Epstein, V. N. Goncharov, C. K. Li, R. L. McCrory, P. W. McKenty, P. B. Radha, S. Skupsky, V. Yu. Glebov, D. R. Harding, D. D. Meyerhofer, F. J. Marshall, R. D. Petrasso, S. P. Regan, F. H. Séguin, W. Seka, V. A. Smalyuk, C. Stoeckl, J. M. Soures, and J. D. Zuegel, "OMEGA Direct-Drive Cryogenic Target Physics," in *Inertial Fusion Sciences and Applications 2001*, edited by K. A. Tanaka, D. D. Meyerhofer and J. Meyer-ter-Vehn (Elsevier, Paris, 2002), pp. 126–131.

L. J. Waxer, J. H. Kelly, J. Rothenberg, A. Babushkin, C. Bibeau, A. Bayramian, and S. Payne, "Precision Spectral Sculpting for Narrow-Band Amplification of Broadband Frequency-Modulated Pulses," Opt. Lett. **27**, 1427 (2002).

## Forthcoming Publications

A. Babushkin, M. J. Harvey, and M. D. Skeldon, "The Output Signal-to-Noise Ratio of a Nd:YLF Regenerative Amplifier," to be published in Applied Optics.

Y. Geng, S. W. Culligan, A. Trajkovska, J. U. Wallace, and S. H. Chen, "Monodisperse Oligofluorenes Forming Glassy Nematic Films for Polarized Blue Emission," to be published in Chemistry of Materials.

R. K. Kirkwood, J. D. Moody, A. B. Langdon, B. I. Cohen, E. A. Williams, M. R. Dorr, J. A. Hittinger, R. Berger, P. E. Young, L. J. Suter, L. Divol, S. H. Glenzer, O. L. Landen, and W. Seka, "Observation of Saturation of Energy Transfer Between Copropagating Beams in a Flowing Plasma," to be published in Physical Review Letters.

J. A. Marozas and J. D. Zuegel, "The Smoothing Performance of Ultrafast Pickets on the NIF," to be published in the Journal of the Optical Society of America B.

R. L. McCrory, D. D. Meyerhofer, R. Betti, T. R. Boehly, R. S. Craxton, T. J. B. Collins, J. A. Delettrez, R. Epstein, V. Yu. Glebov, V. N. Goncharov, D. R. Harding, R. L. Keck, J. H. Kelly, J. P. Knauer, S. J. Loucks, L. Lund, J. A. Marozas, P. W. McKenty, F. J. Marshall, S. F. B. Morse, P. B. Radha, S. P. Regan, S. Roberts, W. Seka, S. Skupsky, V. A. Smalyuk, C. Sorce, C. Stoeckl, C Soures, R. P. J. Town, B. Yaakobi, J. A. Frenje, C. K. Li, R. D. Petrasso, F. H. Séguin, K. Fletcher, S. Padalino, C. Freeman, and C. Sangster, "Direct-Drive Inertial Confinement Fusion Research at the Laboratory for Laser Energetics," to be published in the proceedings of *Current Trends in International Fusion Research: A Review*.

S. Papernov and A. W. Schmid, "Correlations Between Embedded Single Gold Nanoparticles in $SiO_2$ Thin Film and Nanoscale Crater Formation Induced by Pulsed-Laser Radiation," to be published in the Journal of Applied Physics.

G. Sabouret, C. Williams, and R. Sobolewski, "Resistive Switching Dynamics in Current-Biased $YBa_2Cu_3O_{7-x}$ Microbridges Excited by Nanosecond Electrical Pulses," to be published in Physical Review B.

W. Seka, H. A. Baldis, J. Fuchs, S. P. Regan, D. D. Meyerhofer, C. Stoeckl, B. Yaakobi, R. S. Craxton, and R. W. Short, "Multibeam Stimulated Brillouin Scattering from Hot Solid-Target Plasmas," to be published in Physical Review Letters.

W. T. Shmayda, S. Zukotynski, D. Yeghikyan, and F. Gaspari, "Properties of Amorphous Carbon Films," to be published in Fusion Science and Technology.

M. D. Skeldon, "An Optical-Pulse-Shaping System Based on an Electro-Optic Modulator Driven by an Aperture-Coupled-Stripline Electrical-Waveform Generator," to be published in the Journal of the Optical Society of America B.

V. A. Smalyuk, S. B. Dumanis, F. J. Marshall, J. A. Delettrez, D. D. Meyerhofer, T. C. Sangster, and B. Yaakobi, "Radial Structure of Shell Modulations Near Peak Compression of Spherical Implosions," to be published in Physics of Plasmas.

V. A. Smalyuk, P. B. Radha, J. A. Delettrez, V. Yu. Glebov, V. N. Goncharov, D. D. Meyerhofer, S. P. Regan, S. Roberts, T. C. Sangster, J. M. Soures, C. Stoeckl, J. A. Frenje, C. K. Li, R. D. Petrasso, and F. H. Séguin, "Time-Resolved Areal-Density Measurements with Proton Spectroscopy in Spherical Implosions," to be published in Physical Review Letters.

C. Stoeckl, V. Yu. Glebov, J. D. Zuegel, and D. D. Meyerhofer, "Wide-Dynamic-Range 'Neutron Bang Time' Detector on OMEGA," to be published in Review of Scientific Instruments.

A. Sunahara, J. A. Delettrez, C. Stoeckl, R. W. Short, and S. Skupsky, "Time-Dependent Electron-Thermal-Flux Inhibition in Direct-Drive Laser Implosion," to be published in Physical Review Letters.

B. Yaakobi, F. J. Marshall, T. R. Boehly, R. P. J. Town, and D. D. Meyerhofer, "Extended X-Ray Absorption Fine Structure Experiments Using a Laser-Imploded Target as a Radiation Source," to be published in the Journal of the Optical Society of America B.

J. D. Zuegel and S. A. Letzring, "Bulk Microwave Phase Modulators for Smoothing by Spectral Dispersion," to be published in Applied Optics.

## Conference Presentations

T. Z. Kosc, K. L. Marshall, S. D. Jacobs, and J. C. Lambropoulos, "Electric Field–Induced Rotation of Polymer Cholesteric Liquid Crystal Flakes: Mechanisms and Applications," International Symposium on Optical Science and Technology, Seattle, WA, 7–11 July 2002.

---

The following presentations were made at the 14th Topical Conference on High-Temperature Plasma Diagnostics, Madison, WI, 8–11 July 2002:

V. Yu. Glebov, C. Stoeckl, T. C. Sangster, D. D. Meyerhofer, P. B. Radha, S. Padalino, L. Baumgart, R. Coburn, and J. Fuschino, "Carbon Activation Diagnostic for Tertiary Neutron Measurements."

O. V. Gotchev, P. A. Jaanimagi, J. P. Knauer, F. J. Marshall, D. D. Meyerhofer, N. Bassett, and J. B. Oliver, "High-Throughput, High-Resolution, Kirkpatrick–Baez Microscope for Advanced Streaked Imaging of ICF Experiments on OMEGA."

D. L. McCrorey, R. C. Mancini, V. A. Smalyuk, S. P. Regan, and B. Yaakobi, "Spectroscopic Determination of Compressed-Shell Conditions in OMEGA Implosions Based on Ti *K*-Shell Line Absorption Analysis."

C. Stoeckl, V. Yu. Glebov, S. Roberts, T. C. Sangster, R. A. Lerche, and C. Sorce, "A TIM-Based Neutron Diagnostic for Cryogenic Experiments on OMEGA."

---

The following presentations were made at the 32nd Anomalous Absorption Conference, Oahu, HI, 21–26 July 2002:

J. A. Delettrez, J. P. Knauer, P. A. Jaanimagi, W. Seka, and C. Stoeckl, "Numerical Investigation of Recent Laser Absorption and Drive Experiments of CH Spherical Shells on the OMEGA Laser."

V. N. Goncharov, J. P. Knauer, P. W. McKenty, S. Skupsky, T. C. Sangster, R. Betti, and D. D. Meyerhofer, "Adiabat Shaping of Direct-Drive Inertial Confinement Fusion (ICF) Implosions Using a High-Intensity Picket."

C. K. Li, F. H. Séguin, J. A. Frenje, S. Kurebayashi, R. D. Petrasso, D. D. Meyerhofer, J. M. Soures, J. A. Delettrez, V. Yu Glebov, F. J. Marshall, P. B. Radha, S. P. Regan, S. Roberts, T. C. Sangster, and C. Stoeckl, "Effects of Fuel–Shell Mix on Direct-Drive, Spherical Implosions on OMEGA."

A. Maximov, J. Myatt, and R. W. Short, "Nonlinear Propagation of Laser Beams in Plasmas Near a Critical-Density Surface."

J. Myatt, A. Maximov, and R. W. Short, "Modeling Laser–Plasma Interaction Physics Under Direct-Drive Inertial Confinement Fusion Conditions."

R. D. Petrasso, R. Rygg, J. A. Frenje, C. K. Li, F. H. Séguin, S. Kurebayashi, B. Schwartz, P. B. Radha, J. M. Soures, J. A. Delettrez, V. Yu. Glebov, D. D. Meyerhofer, S. Roberts, T. C. Sangster, C. Stoeckl, and S. Hatchett, "Capsule Areal-Density Nonuniformities and Evolution Inferred from 14.7-MeV Proton Line Structure in OMEGA $D^3He$ Implosions."

S. P. Regan, R. S. Craxton, J. A. Delettrez, D. D. Meyerhofer, T. C. Sangster, W. Seka, and B. Yaakobi, "Experimental Investigation of Expansion Velocity and Gradients in Long-Scale-Length Plasmas on OMEGA."

W. Seka, C. Stoeckl, B. Yaakobi, R. S. Craxton, R. W. Short, and H. Baldis, "Fast-Electron Preheat of Direct-Drive Targets Due to the Two-Plasmon-Decay Instability."

R. W. Short, "A Linear Model of Anomalous Stimulated Raman Scattering and Electron-Acoustic Waves in Laser-Produced Plasmas."

V. A. Smalyuk, J. A. Delettrez, R. Epstein, V. N. Goncharov, F. J. Marshall, D. D. Meyerhofer, S. P. Regan, T. C. Sangster, B. Yaakobi, D. L. McCrorey, and R. C. Mancini, "Measurements of Heat Propagation in Compressed Shells in Direct-Drive Spherical Implosions on OMEGA."

V. A. Smalyuk, P. B. Radha, J. A. Delettrez, V. Yu. Glebov, V. N. Goncharov, J. P. Knauer, D. D. Meyerhofer, S. P. Regan, S. Roberts, T. C. Sangster, S. Skupsky, J. M. Soures, C. Stoeckl, R. P. J. Town, J. A. Frenje, C. K. Li, R. D. Petrasso, and F. H. Séguin, "Areal-Density-Growth Measurements with Proton Spectroscopy in Spherical Implosions on OMEGA."

---

S. G. Lukishova, A. W. Schmid, and R. W. Boyd, "Near-Field Optical Microscopy of Cholesteric Oligomer Liquid Crystal Layers," 7th International Conference on Near-Field Optics and Related Techniques, Rochester, NY, 11–15 August 2002.

---

D. W. Griffin and K. L. Marshall, "Phase-Shifting Liquid Crystal Interferometers for Microgravity Fluid Physics," 6th Microgravity Fluid Physics and Transport Phenomena Conference, Cleveland OH, 14–16 August 2002.

---

S. Papernov and A. W. Schmid, "Damage Behavior of $SiO_2$ Thin Films Containing Gold Nanoparticles Lodged on a Predetermined Distance from the Film Surface," XXXIV Annual Symposium on Optical Materials for High-Power Lasers, Boulder, CO, 16–19 September 2002.

---

S. P. Regan, J. A. Delettrez, F. J. Marshall, J. M. Soures, V. A. Smalyuk, B. Yaakobi, R. Epstein, V. Yu. Glebov, P. A. Jaanimagi, D. D. Meyerhofer, P. B. Radha, T. C. Sangster, W. Seka, S. Skupsky, C. Stoeckl, D. A. Haynes, Jr., I. E. Golovkin, J. A. Frenje, C. K. Li, R. D. Petrasso, and F. H. Séguin, "Experimental Investigation of Shell Mix in the Compressed Core of Spherical Implosions Involving Hot, Dense Spectroscopy," 10th International Workshop on Radiative Properties of Hot Dense Matter, Saint-Malo, Brittany, France, 16–20 September 2002.

---

S. D. Jacobs, H. M. Pollicove, E. M. Fees, and J. Schoen, "Aspheric Optics Manufacturing for Commercial and Military Systems," First Symposium for Explosive Materials, Weapons, and Military Technology, Ohrid, Republic of Macedonia, 25–28 September 2002.

---

The following presentations were made at the 2002 OSA Annual Meeting, Orlando, FL, 29 September–3 October 2002:

M. J. Guardalben, J. Keegan, L. J. Waxer, and J. D. Zuegel, "Stability of Optical Parametric Amplification: Spatiotemporal Considerations in the Design of an OPCPA System."

S. G. Lukishova, R. W. Boyd, N. Lepeshkin, A. W. Schmid, and K. L. Marshall, "Feedback-Free Pattern Formation in Dye-Doped Liquid Crystals and Isotropic Liquids."

L. J. Waxer, V. Bagnoud, I. A. Begishev, M. J. Guardalben, J. Puth, and J. D. Zuegel, "Development of a High-Conversion-Efficiency OPCPA System for the OMEGA EP Laser System."

UNIVERSITY OF
ROCHESTER